

BOSTON UNIVERSITY
COLLEGE OF ENGINEERING

Dissertation

**ENGINEERING WITH ATOMICALLY THIN MATERIALS:
MAKING CRYSTAL GRAINS, STRAINS, AND
NANOPOROUS MEMBRANES**

by

DAVID LLOYD

MPhys., University of Oxford, 2013

Submitted in partial fulfillment of the
requirements for the degree of
Doctor of Philosophy

2020

© 2020 by
DAVID LLOYD
All rights reserved

Approved by

First Reader

Joseph Scott Bunch, Ph.D.
Associate Professor of Mechanical Engineering
Associate Professor of Materials Science and Engineering
Associate Professor of Physics

Second Reader

Anna K. Swan, Ph.D.
Associate Professor of Electrical and Computer Engineering
Associate Professor of Materials Science and Engineering
Associate Professor of Physics

Third Reader

Douglas P. Holmes, Ph.D.
Associate Professor of Mechanical Engineering
Associate Professor of Materials Science and Engineering

Fourth Reader

Chuanhua Duan, Ph.D.
Assistant Professor of Mechanical Engineering
Assistant Professor of Materials Science and Engineering

We're here to get each other through this thing, whatever it is...

Mark Vonnegut

DEDICATION

*My Mum would have loved to see this.
This work is for her.*

ACKNOWLEDGMENTS

During my PhD career I have been extremely fortunate in the colleagues, friends, and loved ones who have supported me throughout this adventure. As I type up the final sentences of this dissertation, there is a clarity gained in viewing the work as a whole. I can see now more than ever how utterly reliant I have been on the guidance, intelligence, and kindness of countless people who have worked alongside me to bring success to these projects. I am truly grateful to you all.

The most important person to acknowledge is my advisor, Scott Bunch. I emailed Scott in 2013 after I kept noticing his name on cool nanotechnology papers. He quickly replied with the same support and encouragement that has gone on to characterize his mentorship of me for the past six years. Scott is a brilliant scientist, and I have learnt much from his curiosity, inventiveness, and wise skepticism as he's guided me through my PhD. Importantly, he has always given me the space to try my own ideas and make my own mistakes. He never gave me a hard time for my failures, instead providing gentle nudges and suggestions which usually led to successes down the road. One characteristic I think really distinguishes Scott is his fearlessness as a researcher – his record of publications shows that he is not afraid to try experiments that might seem crazy or impossible to begin with, but which end up producing work that really pushes research forward into exciting new terrain. I hope I will take some of these qualities with me as I move on to new things.

I would also like to thank my committee – Anna Swan, Doug Holmes, and Chuanhua Duan – for their advice and thought provoking discussions over the years. Thanks too to the other BU faculty – Harold Park, Xi Ling, Aaron Schmidt, and others – for much help and fruitful collaboration.

I have learnt a huge amount from my fellow graduate students, and have been consistently impressed by their level of dedication, expertise, and intelligence. I particularly want to thank my fellow members of the Bunch lab, especially Lauren Cantley who trained me from the ground up on imaging, lab and cleanroom techniques, a time consuming feat for which I am extremely grateful. Without her skill and patience I simply wouldn't have been able to get started with research at all. My work with graphene nanopores in chapter 7 was a continuation of Lauren's project, and so owes much to methods and protocols originally developed by her. Meteh Calis and Feri Yousefi joined the lab after me, and it wasn't long after training them in the basics that they were coming back to teach me new tricks of their own. They have both been a joy to work with. Meteh is a diligent and committed researcher who has a wonderful appetite for learning, always asking great questions to get to the deepest understanding of new concepts. I wish him the very best for his new challenge – raising his son Egemen, born a few months ago. Feri is always quick on the uptake and is never satisfied with having a partial understanding of the theory behind his experiments, and it's been great to see him gradually gain mastery over the resonator set-up. They've both been great fun to work with and I wish them both the very best with their future research. Thanks too to the

countless other visiting PhD, masters and undergraduate students who have passed through the lab: Andrew Theori, Nikunj Khetan, Gaby Abad, Anubhav Wadehra, Brian Kim, Robert Fraser, Runze Chi, Guang Yang, Santiago Cartamil, to name but a few. A huge thanks especially to Anubhav, Brian, Runze, Guang, and Nikunj for helping me build and optimize the CVD growth furnace –your perseverance with this often tedious process sped up the progress of the project immensely.

I was lucky to have many friends dotted around the photonics and physics buildings who were sources of priceless troubleshooting tips and fun discussions. A special mention goes to Jason Christopher, with whom I shared many happy (and frequently comical) collaborations. Jason is extremely talented, one of those guys who excels at whatever he turns his hand to, and whose understanding of the field was so wide and deep that I was always finding excuses to bump into him and ask him questions. He was also a great friend, and we shared many a laugh over our common frustrations and delighted in each other's occasional successes. He also taught me my favorite phrase of my PhD - *skinning the yak* (to encounter layer upon layer of successively more circuitous intermediate problems until before long you find you are...). Over the years we accumulated many heaps of butchered ox carcass together on various projects, and I am thankful for his many contributions to the work presented below.

I would like to also thank Ang Liu, Xiaowei Wang, Leonard 'Rasta' Kergos, Jackson Chang, Vural Kara, Fish Wang, to name just a few staples of the cleanroom

scene gave me many useful tips and tricks, and who brought warmth and humour to this sterile environment. Paul Mak has managed the cleanroom with aplomb, fixing countless machines and facilitating my progress immensely. Jacob Swett provided innumerable insights and bright ideas for the nanopore project – he’s a very smart and creative researcher and one to watch for sure. In the past year I have had the pleasure of working closely with some members of the Duan lab, particularly Sean Xiao, Rami Yazbeck and Vera Xu, due to their expertise with nanopore experiments. They are a great team, full of smart ideas and perseverance, and I’m confident you will all go on to do great things. I’m also grateful for the general warm and helpful presence of a load more PhD students, such as Mounika Vutukuru, Marco Chen, Miguel Goni Rodrigo, Rachel Jayne, Elbara Ziade, Cory Pollock, Alex Stange, Wes Britton, Sedat Dogru, Cagatay Karakan, and others whom I have surely forgotten to add here.

The friendships I’ve made outside the lab have given me invaluable support through the inevitable challenges of a PhD. I have been very lucky with the roommates I’ve had over the years: Rohan, Jamie, Meredith, Euro, Oscar, Minagi, and Michael. Thanks too to Alek Zosuls, my landlord for several years who allowed me to hook up his outboard motor to my inflatable dinghy. Taking out landlubbers to cruise the Charles at speed and make landings on the Harbor Islands was the closest I’ll likely get to piracy, and was a hell of a lot of fun. Here’s just a handful of friendships and memories I will treasure: hiking the Whites with Ali and Sia, seeing the total eclipse of 2017 with Nithin and friends in Idaho, eating our way through Osaka with Jon, paddling through some true

wilderness in Quebec with Melina followed by Christmases in Montreal with her family, celebrating thanksgiving with Tomoki, Olivia, Ali, Susan and Reza in San Francisco, and after work drinks with Becks, Alex S and Mounika,... The people I've met in the last few years span the full gamut of personalities and backgrounds, and has been a thoroughly enriching experience to know you all. The timing of my graduation is a tad unfortunate – I am writing these words in the midst of the COVID-19 lockdown – meaning we haven't had the opportunity to celebrate in person. Rest assured, some day soon we will be safe to lay down our PPE and emerge from the fusty chrysalises of our apartments, and we will celebrate then.

My parents have supported me in so many ways it will be impossible to do justice to them here. Dad surrounded me and my brother with science from a young age, guiding us with the manufacture of model boats, power generators and gun powder. Along the way he taught us to think carefully and skeptically, to be wary of easy explanations which elide the true complexity of the world. It is surely not a coincidence that both his sons are now researchers full time. Mum would have been so proud to see this achievement. Whenever I would have doubts about my abilities she would always remind me to just do the best I can, simple advice which I keep coming back too. I really couldn't have asked for more loving and supportive parents, and could not have earned this degree without the love and encouragement they spent a good deal of their lives dedicating their children. I'm grateful too to my brother Ben for some wonderful adventures and discussions over

the course of my PhD, and some of his suggestions and ideas turned out to be very useful in the work presented below.

Lastly I want to thank my girlfriend Alex, the greatest source of joy in my life. I learn every day from her kindness, playfulness, and her inspiring dedication to helping others. She defended her PhD one week after me, and watching her razor sharp mind in action was one of the most exciting and joyous things I have ever seen. We have both overcome many challenges in the past year, but the love and care we show each other every day makes life better than I thought possible. I can't wait to continue our adventure together.

This thesis marks the end of a degree, the accumulation of what I have learnt. But what is presented here is of course only partial. In the past six years I learnt not just how to do science, but about friendship, kindness and love too. These are my most valuable findings, ones that will nourish me as I move on to whatever lies ahead. To my many teachers – all those mentioned above, and the many I have missed – thank you.

**ENGINEERING WITH ATOMICALLY THIN MATERIALS:
MAKING CRYSTAL GRAINS, STRAINS, AND NANOPOROUS MEMBRANES**

DAVID LLOYD

Boston University College of Engineering, 2020

Major Professor: J. Scott Bunch, Associate Professor of Mechanical Engineering,
Associate Professor of Materials Science and Engineering, Associate
Professor of Physics

ABSTRACT

Monolayer molybdenum disulfide (MoS_2) is a three-atom-thick direct band gap semiconductor, which has received considerable attention for use as a channel material in atomically thin transistors, photodetectors, excitonic LED's, and many other potential applications. It is also a mechanically exceptional material with a large stiffness and flexibility, and can withstand very large strains (11%) before rupture. In this dissertation we investigated the mechanics of the stiffness and adhesion forces in atomically thin MoS_2 membranes, and how biaxial strains can be used to induce large modulations in the band structure of the material.

First, we used chemical vapor deposition (CVD) to grow MoS_2 crystals that are highly impermeable to gas, and used a pressure difference across suspended membranes to induce large biaxial strains. We demonstrated the continuous and reversible tuning of the optical band gap of suspended monolayer membranes by as much as 500 meV, and induced strains of as much as 5.6% before rupture. We observed the effect of strain on the energy and intensity of the peaks in the photoluminescence (PL) and Raman spectra

and found their linear strain tuning rates, then report evidence for the strain tuning of higher level optical transitions.

Second, we determined the Young's modulus and works of separation and adhesion of MoS₂ membranes, and found that adhesion hysteresis is an important effect in determining the behavior of our systems.

Finally, we investigated the use of atomically thin materials as nanofiltration membranes, by perforating the material with nanopores which selectively permit the transport of smaller molecules while rejecting larger ones. We studied ion transport through nanopores in graphene membranes and demonstrate that in-situ atomic force microscope measurements in liquid are a powerful way to reveal occlusions and contaminants around the pores - work which will aid future researchers in further unveiling the properties of these fascinating systems.

TABLE OF CONTENTS

DEDICATION	v
ACKNOWLEDGMENTS	vi
ABSTRACT.....	xii
TABLE OF CONTENTS.....	xiv
LIST OF TABLES	xvii
LIST OF FIGURES	xviii
CHAPTER ONE: INTRODUCTION.....	1
1.1 Next generation nanoscale materials	1
1.2 MoS ₂ – a two dimensional semiconductor	3
1.3 Mechanics and strain tuning of MoS ₂	5
1.4 Using atomically thin materials as separation membranes	6
1.5 Outline	8
CHAPTER TWO: BASICS OF SEMICONDUCTOR PHYSICS	10
2.1 The band gap and the Fermi energy.....	10
2.2 Electronic properties of materials	12
2.3 Photoluminescence, excitons, and the optical properties of MoS ₂	16
2.4 Raman scattering and spectroscopy	21
2.5 Spectroscopy experimental setup.....	23
CHAPTER THREE: NANOMECHANICS	25
3.1 Bulge testing	25
3.2 Measuring the adhesion energy	29

3.3 Membrane re-lamination and adhesion hysteresis	34
CHAPTER FOUR: CVD GROWTH AND CHARACTERIZATION	37
4.1 Growing and transferring atomically thin semiconductors.....	37
4.2 Characterizing membrane strength and quality	42
4.3 Optimized growth parameters and troubleshooting.....	47
CHAPTER FIVE: BAND GAP ENGINEERING WITH ULTRA-LARGE BIAxIAL STRAINS IN SUSPENDED MONOLAYER MOS ₂	51
5.1 Introduction.....	51
5.2 Device geometry	54
5.3 Strain tuning the band gap and Raman modes.....	56
5.4 Applying Ultra-large Strains.....	62
5.5 Conclusions.....	66
CHAPTER SIX: ADHESION, STIFFNESS, AND INSTABILITY IN ATOMICALLY THIN MOS ₂ BUBBLES.....	68
6.1 Introduction.....	68
6.2 Device geometry	70
6.3 Finding the Young's modulus and the work of separation.....	72
6.4 Adhesion hysteresis and finding the work of adhesion	78
6.5 Conclusions.....	84
CHAPTER SEVEN: IN-SITU AFM IMAGING OF GRAPHENE NANOPORES	86
7.1 Introduction to nanopores	86
7.2 Conductance measurements of graphene nanopores	89

7.3 In-situ AFM imaging	93
7.4 Nanobubbles in nanopores.....	96
7.5 Discussion.....	99
7.6 Conclusions.....	101
CHAPTER EIGHT: FUTURE WORK AND CONCLUSIONS	102
8.1 Nanofluidic switches using graphene electrowetting	102
8.2 Conclusions.....	105
APPENDIX A: ADDITIONAL DATA FOR CHAPTER 5.....	108
APPENDIX B: ADDITIONAL DATA FOR CHAPTER 6.....	114
APPENDIX C: ADDITIONAL DATA FOR CHAPTER 7	126
BIBLIOGRAPHY.....	128
CURRICULUM VITAE.....	141

LIST OF TABLES

Table 3.1 Values for constants $C(v)$ and $K(v)$ for several 2D crystals, calculated using Hencky's solution.	28
Table 3.1	49
Table 3.2	50
Table 5.1 Raman mode shift rates for each membrane thickness. A comparison of the strain dependencies of the Raman modes that we observed in Fig. 5.2c. These results show that both modes are less strain sensitive with increasing membrane thickness, an effect which was also observed in Rice et al., 2013.....	60

LIST OF FIGURES

Figure 1.1 a) A cross section of the 7nm-process FinFETs in the Apple A12 Bionic processor. Each transistor has a silicon ‘fin’ channel which runs into the page. (adapted from wikichip.org) b) A sub-10nm channel width transistor made from stacked 2D materials (Nourbakhsh et al., 2016).	2
Figure 1.2 a) The layered structure of MoS ₂ . b) An mechanically exfoliated MoS ₂ monolayer on SiO _x , viewed from a microscope (adapted from Wang, et al. 2012) c) The elements highlighted in the periodic table can be combined to make many different TMD’s (adapted from Chhowalla, et al., 2013).	4
Figure 2.1 The electronic band structure of monolayer MoS ₂ (Ellis, Lucero, & Scuseria, 2011), and a zoomed in cartoon of the band gap. The blue circles represent states occupied by electrons.....	11
Figure 2.2 Depending on the Fermi energy, a material can have a high conductance (a & c) or a low conductance (b).....	13
Figure 2.3 Changing the band structure of a crystal in turn affects its conductivity (Manzeli et al. 2015). Strain is applied to suspended MoS ₂ which reduces its band gap energy, which increases its conductivity according to Eq. 2.2.	15
Figure 2.4 a) An electron in the valence band absorbs a phonon (i), is excited into the conduction band (ii), scatters back down to the bottom of the conduction band (iii) and decays back down to the valence band by emitting a photon of lower energy than it absorbed (iv). b) Electrons bind to holes to form stable quasi-particles called <i>excitons</i> . An electron can bind to an exciton to form a <i>trion</i> . The binding energy of these particles mean they have an energy slightly lower than the conduction band. 16	16
Figure 2.5 a) Absorption spectrum of monolayer MoS ₂ , taken at 10K with a -100V gate voltage (Mak et al. 2013). b) Photoluminescence spectrum of monolayer and bilayer MoS ₂ (taken at room temperature). Both curves have peaks corresponding to the <i>A</i> and <i>B</i> excitons, and the bilayer has the additional <i>I</i> peak caused by emission across the indirect band gap. The bilayer curve has been scaled by a factor of x1000 for comparison.	20

Figure 2.6 a) The phonon band structure (J. W. Jiang, 2014). The labels represent types of mode, e.g. LA = longitudinal acoustic. b) Schematic of the main vibrational modes, and c) Raman peaks of MoS ₂	22
Figure 2.7 a) The separation between the two Raman modes increases with MoS ₂ layer thickness (H. Li et al., 2012). b) The Raman peaks are also effected by mechanical strain (Conley et al., 2013a).	23
Figure 2.8 a) Raman microscope schematic. b) Pressure chamber which allows Raman and PL measurements to be taken on pressurized samples.	24
Figure 3.1 a) A membrane subjected to a pressure difference across a sealed aperture. b) The radial and tangential strains in the membrane as a function of radius r . At $r = 0$ the membrane experiences biaxial strain.	26
Figure 3.2 A sealed cavity is filled with pressurized gas after being left to equilibrate in a pressure chamber at p_0 as the gas leaks slowly through the substrate. When it is removed the bulge expands and the internal pressure reduces. The membrane can also delaminate ($a > a_0$).	30
Figure 3.3 a) The free energy $F(a)$ as a function of radius a for different charging pressures p_0 . The grey circles represent the minimum of each curve corresponding to a given pressure p_0 . b) The expected trajectory of the device if the pressure reduces after delamination.	33
Figure 3.4 a) Contact angle hysteresis in sessile liquid drop experiment (Nowak, Combes, Stitt, & Patek, 2013). b) Analogous behavior in delaminated pressurized membranes as the pressure is reduced. The radius of the device gradually increased as the device was inflated, but remained mostly pinned at a constant radius whilst it deflated.	34
Figure 3.5. The modified free energy landscape if $\Gamma_{adh} < \Gamma_{sep}$. As the device reduces its radius its free energy is determined by the dashed lines. The device is now trapped in a free energy minima and snap-in only occurs when the gradient of the dashed line is greater than zero.	36
Figure 4.1 Vacuum furnace set up. Results are improved by adding O ₂ and H ₂	39

Figure 4.2 a) A typical growth of large monolayer MoS₂ domains on a SiO_x substrate. Additional layers tend to grow outwards from the initial crystal seed in the center of each grain. b) A transfer to an array of microcavities. The yield can immediately be determined using an optical microscope. The colored rings in i) show that these monolayer membranes are bulging down and are therefore impermeable. ii) shows the same for a bilayer. iii) shows a broken device and iv) shows a suspended device with no Newton rings – this device is therefore permeable and is likely torn. Scale bar is 20 μm. 41

Figure 4.3 a) Most devices measured had extremely low gas permeabilities, so that devices left out in ambient conditions remained inflated for several months. Different colors represent different devices. b) Gas permeability plotted against gas molecular size. We compare the CVD grown MoS₂ membranes to the pristine and nanoporated graphene samples presented in Koenig et al., 2012. The data suggests CVD grown MoS₂ has a permeability roughly comparable to pristine graphene..... 44

Figure 4.4 The PL enhancement of membranes that were exposed to additional O₂ and N₂ gas during growth. The PL intensity of the black curve saturated the detector – the dashed line is an estimate of the true maximum intensity. 45

Figure 4.5 a) TEM image of CVD grown monolayer MoS₂. There are some single atom vacancies (b) and in some samples are larger nm scale defects (c). The white dots are Mo or S atoms in a hexagonal lattice, with the white haze caused by hydrocarbon contamination stuck to the surface of the membrane..... 46

Figure 5.1 a) Device schematic. b) A typical sample of CVD grown MoS₂ membranes suspended over cylindrical cavities after transfer (scale bar is 20 μm). c) An AFM cross section of a device at various p_{int} , resulting in different biaxial strains at the center of the device. Devices can be bulged up or down depending on whether Δp is positive or negative. 55

Figure 5.2 a) The PL spectra for monolayer MoS₂ at different biaxial strains corresponding to different p_{int} , and the relationship between strain and A peak intensity (inset). Intensities are normalized to the A_{1g} Raman peak. b) The peak positions of the A (red), A⁻ (blue) and B (green) excitons as a function of biaxial strain for CVD (crosses) and exfoliated (triangles) monolayer devices. The peaks were fitted using three Voigt functions. c) The E¹_{2g} and A_{1g} Raman modes for unstrained MoS₂ (inset) and peak positions as a function of biaxial strain. Colors represent different devices. d) A bilayer PL spectrum, and the peak positions of the

A, B and indirect I peak as a function of biaxial strain for exfoliated bilayer and trilayer devices.....	58
Table 5.1 Raman mode shift rates for each membrane thickness. A comparison of the strain dependencies of the Raman modes that we observed in Fig. 5.2c. These results show that both modes are less strain sensitive with increasing membrane thickness, an effect which was also observed in Rice et al., 2013.....	60
Figure 5.3 a) A PL map of a device with $p_{int} \sim 0.75$ MPa and $p_{ext} = 1$ atm, with colours representing the A peak position. b) Line cuts through the center of the device along the x, y, (1,1) and (1,-1) directions.	61
Figure 5.4 <i>In-situ</i> measurements of a) PL spectra for a monolayer device (scaled for comparison with ticks marking A peak position), with the largest pressure difference representing ~ 5 % strain. b) Raman spectra at increasing chamber pressures. Labels refer to the negative pressure difference $-\Delta p$ across the membrane, and Raman peaks are normalized to the silicon peak intensity.....	62
Figure 5.5 a) The Raman intensity ratio E_{2g}^1 / A_{1g} for bulged up (black triangles) and bulged down (colored crosses) devices. b) A zoomed in version of Fig. 5.4b to highlight the 2LA(M) mode.....	64
Figure 5.6 a) The A peak position of the PL spectrum plotted against the strain as determined from the E_{2g}^1 peak shift. In this case we fitted a single curve to the A peak feature, as the large decrease in PL intensity meant that the individual A and A ⁻ peak contribution could not be resolved. Different colors represent different devices. b) The ratio of the integrated intensities of the E_{2g}^1 and A_{1g} modes normalized to the silicon peak and plotted against strain. The expected intensity modulation due to interference is also plotted for comparison.	65
Figure 6.1 a) Microscope image of a delaminated device (scale bar is 5 μ m). b) Device schematic. c) AFM image and d) AFM cross sections. e) Deflection δ and f) radius a plotted against input pressure p_0 . Inset microscope images show a device before and after snap-out (scale bar is 5 μ m).....	71
Figure 6.2 a) Plots for CVD monolayer and bilayer devices (different symbols/colors represent each device), with linear fits (dashed lines) used to find E_{2D} . b) E_{2D} for each device in our exfoliated samples, and three of our CVD samples (N1-3) c) E_{2D} divided by number of layers n for each sample. Data points and error bars represent	

the mean and standard deviation respectively for each sample. Results from nanoindentation measurements in references 16, 28 and 29 are plotted for comparison.....	73
Figure 6.3 Work of separation of membranes of 1 to 3 layer thickness. The data includes measurements of CVD monolayer devices from three separate growths and transfers (N2-4). Several devices are measured per sample, with data points and error bars representing the means and standard deviations respectively. For samples with fewer than 3 measurements the data points represent each device measured. The dashed line marks the mean of the 6 samples.	76
Figure 6.4 Stable delamination with increasing pressure.	77
Figure 6.5 a) AFM cross sections of a device during inflation (increasing N) and deflation (decreasing N). Arrows mark the snap transitions. b) δ and a of devices during inflation and deflation. Different colors represent different devices on sample N2. More data can be found in the supplementary information which is not shown here for reasons of clarity. Red and blue arrows mark snap-out and snap-ins respectively. The upper and lower dashed lines correspond to solutions to Eq. 6.4 and Eq. 6.7 respectively. c) A comparison between the works of separation and adhesion for samples N2-4. Data points and error bars represent the means and standard deviations respectively of all the devices measured on each sample.....	79
Figure 6.6 a) The free energy landscape for a device with no adhesion hysteresis. The device radius adjusts to minimize the free energy, and the energy minima are marked with grey circles. b) The energy landscape if the criteria in Eq. 6.5 are followed. The dashed and solid lines are generated using Eq. 6.2 with $\Gamma = \Gamma_{adh}$ and $\Gamma = \Gamma_{sep}$ respectively.	80
Figure 6.7 a) We checked the repeatability of our measurements of Γ_{adh} by repeating the experiment 6 times on a single device at a number of different charging pressures, which resulted in a mean and standard deviation of 13 mJ/m ² and 5 mJ/m ² respectively. b) Mean and standard deviations of the work of adhesion in each sample. The dashed line represents the mean of the 5 samples.	82
Figure 7.1 a) The membrane lipoprotein used by Oxford nanopore to sequence DNA. b) The steric exclusion of ion hydration radii means that large ion selectivity can be achieved in sub-nanometer graphene nanopores. In this case, K ⁺ cations have a flux	

across the pore that is several orders of magnitude higher the similarly sized Cl^- anions. Both images from (Sahu & Zwolak, 2019).	87
Figure 7.2 a) Cartoon schematic of the device geometry. The real suspended graphene region is 1 to 5 μm in diameter. b) Helium ion microscope (HIM) image of a nanopore. The region of white contrast is caused by hydrocarbon contamination deposited around the pore mouth during the HIM milling process. c) The PDMS flow cell and mounted Si/ SiN_x chip.....	90
Figure 7.3 a) The IV characteristics for pores in three different states. Large linear conductance (i), low non-linear conductance (ii), and non-conductive (iii). b) The cation selectivity of a 50 nm pore device in <i>state ii</i> . The dashed line represents the predicted conductance curve for a pore of this diameter.	92
Figure 7.4 a) A device with a 50 nm pore, imaged with AFM first in air then in H_2O . The pore region is occluded when in liquid. The square region around the device is caused by hydrocarbons introduced during HIM imaging. b) A zoom-in and cross section of the bubble-like object occluding the pore. c) AFM images of the bubble in water and ethanol. The bubble disappears when water is replaced with EtOH, and reappears when water is re-introduced. The images are imperfectly aligned due to sample drift.	94
Figure 7.5 AFM images of the pore taken in water with different set point ratios of (a) 36%, (b) 30%, and back to 36% again (c). The lower set point ratio increases tip-sample forces which deform the bubble.	95
Figure 7.6 a) AFM phase channel image of a 75 nm diameter pore with no pore occlusion. The phase channel was used to get the best contrast for the pore edges. Scale bar is 200 nm. b) Conductance curves for the device shown in (a). Based on the conductance curves and Eq. 7.1 the predicted pore radius is 74 nm, in good agreement with the AFM images. c) AFM of a device in air and d) imaged in water. The device appears much cleaner using the new mounting procedure. e) Adding liquid that has passed through a PDMS flow cell makes the device significantly more dirty. f) Another device with a 150 nm pore is imaged in air then g) in water. The pore is free of bubbles, but immediately became covered in what appears to be some other kind of contaminant.....	99
Figure 8.1 a) The application of V_{sd} in the geometry described in chapter 7 occasionally precipitated the delamination of the graphene membrane from the SiN_x substrate. b)	

The geometry used in this chapter involves applying a gate voltage to the graphene, and wetting only the back side of the membrane.....	103
Figure 8.2 a) A gate voltage of 5V causes delamination of the graphene membrane, which can be seen in both the height and phase channels. b) The delaminated region is raised by approximately 5 nm. c) The graphene membrane and electric double layer have a capacitance that energetically drives the delamination process. d) Electrowetting can occur at small voltage magnitudes – in this case -0.3V. e) The delaminated region is raised by ~15 nm.	104
Figure A1 a) An example of the peak shift in two monolayer devices in which p_{int} was increased then decreased, with AFM images of both devices after pressure cycling (scale bars are 2 μm). Device 2 shows evidence of slipping. b) The repeatability of subjecting a device to high strain. Measurements were taken in the sequence indicated.....	108
Figure A2 Comparison of the change in A peak exciton intensity with strain to a theoretical prediction. The intensity of our data has been scaled for comparison with the theory.	109
Figure A3 a) A ray diagram of incident and scattered light. The effective power of the excitation laser (black) is the sum of the incident beam with its reflected beams. The intensities of Raman scattered light (red) also depend on the sum of reflected rays, and rays scattered at different phases within the MoS ₂ or Si. The effect of this interference for each frequency of light depends on the distance between membrane and substrate, d_2 , which changes as the devices are strained. b) & c) The intensities of the E ¹ _{2g} and A _{1g} peaks relative to the Si peak. We compare our data (crosses) to the interference model (blue line).	111
Figure A4 The ratio of integrated intensities of the E ¹ _{2g} to A _{1g} Raman modes for different membrane thicknesses.	112
Figure A5 a) Line scan of Raman modes across a device. b) Peak positions and c) peak intensities of the Raman modes (normalized to the Si peak) across the device. d) The ratio E ¹ _{2g} / A _{1g} of the two Raman mode intensities across the device.	113
Figure B1 All I_{sep} data used to calculate means and standard deviations of each sample in Fig. 6.3.	115

Figure B2 Data for devices measured on sample *N2*, showing the values of δ_c and a_p just before snap-in used to calculate Γ_{adh} . Each color/symbol represents a different device. 116

Figure B3 a) Work of adhesion for every device measured in each sample. b) A device which delaminates stably with increasing pressure, but shows adhesion hysteresis upon deflation. This device snapped in to an intermediate step before fully re-laminating to the substrate. 117

Figure B4 a) AFM image (amplitude channel) of a delaminated device before the snap-in transition. The position of the microcavity is marked by a dashed circle. Below is a cross section of the device. b) Strain map of the same device after the snap-in transition when the device has fully deflated. Strain is calculated using the peak shift in the E_{2g}^1 Raman mode at each point. Each pixel is $1 \times 1 \mu\text{m}$ and corresponds to a single Raman scan..... 118

Figure B5 a) Raman line scans over a device over time as it deflates. Dashed vertical lines mark the edge of the delaminated bubble. b) A zoomed in version of a) focusing on the edge region of the device. c) AFM cross sections of the device at each time, using the same color scheme as in a). d) Radial (ϵ_r) and tangential (ϵ_θ) components of the strain as a function of radius for this device’s initial geometry before deflating, calculated using Hencky’s model with values for δ and a taken from the red curve in c)..... 120

Figure B6 The contact angle of a device during inflation (black) and deflation (red). .. 121

Figure B7 a) Complete data containing all data points of results presented in Fig. 6.5b in the main text. Each color represents a different device. b) Comparison of snap-in transitions measured optically or by AFM. For optical measurements a is determined using an optical microscope with a 100x objective, and δ is determined from the PL peak position and Eq. B4. 124

Figure B8 a) CVD monolayer devices from sample *N1* and *N2*. b) Exfoliated monolayer and trilayers devices. Dashed lines are plotted for each of the sample means reported in Fig. 6.2c of the main text. Different color/symbols represent different devices. 125

Figure C1 Examples of other devices we imaged which are covered in nanobubbles. The devices were measured with AFM in water. Scale bars are $1\mu\text{m}$ 127

Figure C2 Evidence of hydrocarbon contamination around the nanopore mouth after HIM milling. The white region indicates charging is occurring on the electrically insulating hydrocarbon layer..... 127

CHAPTER ONE: INTRODUCTION

1.1 Next generation nanoscale materials

Innovations in our ability to engineer matter at the nanometer length scale have had, and will continue to have, a profound effect on human history. The most dramatic of nanotechnology's successes has been the miniaturization of silicon based electronic components. Between 1970 and 2020, the number of transistors that can be packed on a microchip has increased by a factor of over one million, with the latest Apple A12X Bionic processor containing a total of roughly one billion (Roser, 2020). These astonishing figures derive from half a century of steady cumulative improvements in CMOS fabrication methods aimed at reducing transistor sizes, and has delivered us the age of smartphones, AlphaGo, and self-driving cars*.

The latest generation of FinFET transistors have channel widths less than 10 nm wide (Fig.1.1a). This fact presents us with a remarkable achievement of engineering, but also a challenge. Transistor dimensions are approaching their fundamental limit – the length scale of single atoms. In order to proceed along the path of miniaturization, scientists and engineers must turn their ingenuity to the challenge of building electrical components with dimensions containing just a handful of atoms.

* Great technological innovations rarely arrive without their troubling side effects. Just as the miracle of nuclear power followed the horrors of Hiroshima, so too the computer age has given us both Wikipedia and the YouTube Influencer.

The work in this thesis will be about a class of materials which may help us rise to this challenge. Graphene, discovered in 2004, is a honeycomb lattice of carbon atoms that is only a single atom thick, and is therefore a truly two-dimensional material. It is also the world's strongest material, extremely electrically and thermally conductive, totally impermeable to all molecules, and highly elastic, to name just a few of its superlative properties. After graphene an enormous cohort of other 2D crystals were isolated, including many semiconductors (MoS_2 , WSe_2 , black phosphorus etc.), the electrically insulating hexagonal boron nitride (hBN), Xenos such as Silicene and Germanene, with more added to the list each passing year. Nanotechnologists thus have in their hands a rich panoply of materials to connect and combine to engineer the next generation of atomically thin devices (Fig.1.1b).

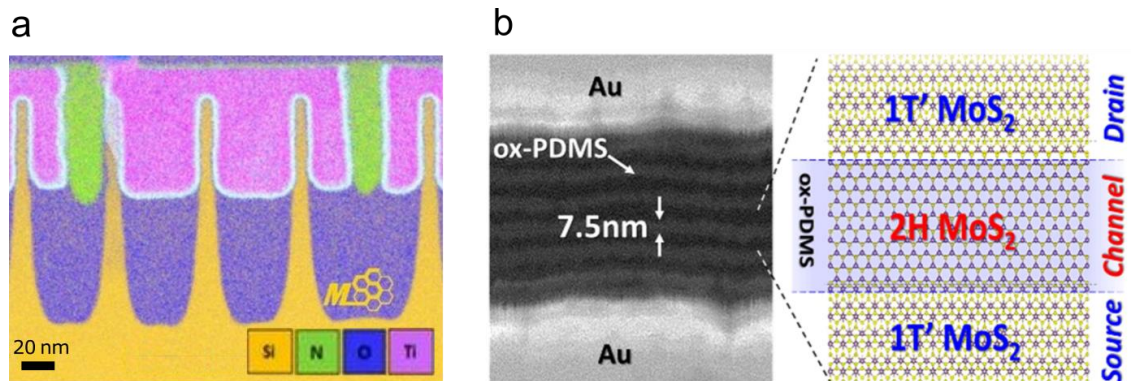


Figure 1.1 a) A cross section of the 7nm-process FinFETs in the Apple A12 Bionic processor. Each transistor has a silicon ‘fin’ channel which runs into the page. (adapted from wikichip.org) b) A sub-10nm channel width transistor made from stacked 2D materials (Nourbakhsh et al., 2016).

1.2 MoS₂ – a two-dimensional semiconductor

The bulk of this thesis will be concerned with the archetypal 2D semiconductor – MoS₂. This was the first semiconducting 2D material to be isolated and is therefore the most widely studied. The discovery generated considerable excitement because the three-atom-thick crystal has a large direct band-gap (Mak, Lee, Hone, Shan, & Heinz, 2010), meaning it is intrinsically much better suited for making transistors than graphene. It is also a strong absorber and emitter of light, making it well suited for applications such as the photodetector that depend on the interaction of electricity and light.

Bulk MoS₂ is composed of many stacked layers of 2D honeycomb lattices (Fig. 1.2a), with each layer bound to its neighbor by van der Waals forces. This bulk form has long been used as a dry lubricant in engines and brakes, due to the ease with which layers can slide past each other. This relatively weak binding between layers is what allowed the first monolayer form to be isolated by peeling off a single layer of bulk crystal by *mechanical exfoliation* (Fig. 1.1b), though now the monolayer crystals are more often grown from scratch with methods like *chemical vapor deposition* (CVD). MoS₂ belongs to the class of materials called the *transition metal dichalcogenides* (or TMD's), which are crystals formed by bonding a transition metal (any element in groups 3-11 of the periodic table) with a pair of chalcogenides (the elements of group 16). A huge number of permutations can therefore be formed, but the most frequently studied are MoS₂, MoSe₂, WS₂, and WSe₂, which are all large band gap semiconductors with slightly different

properties (Chhowalla et al., 2013). Despite this thesis' focus on MoS₂, the similarities between the materials of this class mean that many of the methods used here can be transferred directly for the study of the other TMD's too.

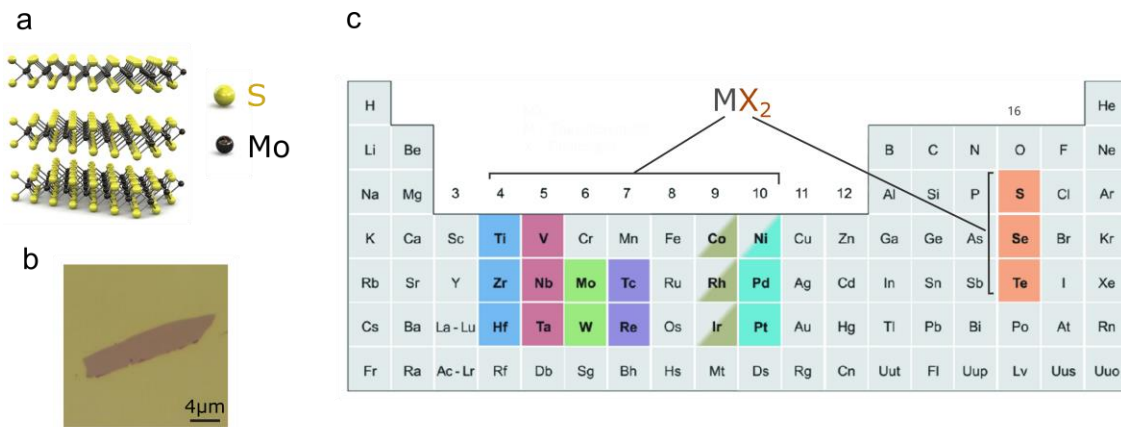


Figure 1.2 a) The layered structure of MoS₂. b) An mechanically exfoliated MoS₂ monolayer on SiO_x, viewed from a microscope (adapted from Wang, et al. 2012) c) The elements highlighted in the periodic table can be combined to make many different TMD's (adapted from Chhowalla, et al., 2013).

Research interest in MoS₂ is driven by the performance of the devices which can be made from it. The excitement began with the demonstration of the first monolayer MoS₂ transistor (Radisavljevic, Radenovic, Brivio, Giacometti, & Kis, 2011b), which had large on-off ratio's and a carrier mobility of $\sim 200 \text{ cm}^2\text{V}^{-1}\text{s}^{-1}$. While this mobility was comparable to state of the art graphene transistors of the time, it is still much less than its theoretically predicted maximum value due to the presence of scattering sites at defects in the crystal or at its interfaces. Much more work will be needed to improve carrier mobilities, growth quality, and reduce the contact Schottky barriers if MoS₂ transistors

are to develop into a mainstream technology (Verreck, Arutchelvan, Heyns, & Radu, 2019).

MoS₂ has a number of interesting material properties which make other possible device applications possible too, and the literature now contains hundreds of such examples. It is mechanically flexible making it ideal for use in flexible electronics (Akinwande, Petrone, & Hone, 2014). It is optically active and has been used to make excitonic LEDs, photodetectors and optically gated memories (Mak & Shan, 2016; Roy et al., 2013). It also allows the conduction of electrons while maintaining their spin degree of freedom, a property that could be used to make so-called *spintronic* devices (Manzeli, Ovchinnikov, Pasquier, Yazyev, & Kis, 2017). Many other TMD's are being vigorously investigated for these applications and more.

1.3 Mechanics and strain tuning of MoS₂

It is the semiconducting nature of TMD's – the presence of a band gap – that make feasible so many of the devices described above. The central importance of the band gap leads us on to another intriguing property of MoS₂ – it has a band gap that changes magnitude depending on the mechanical strain within the material. While this property is not unique to MoS₂, the strain sensitivity of the band gap combined with the crystal's enormous breaking strain (~11%) make the material extraordinarily well suited to using strain to modulate the size of the band gap, also known as *strain engineering* (Manzeli, Allain, Ghadimi, & Kis, 2015a).

Strain engineering is a powerful tool that opens up two new routes. Firstly, we can use strain to optimize and enhance the performance of the material in already extant devices. This kind of optimization is common in semiconductor manufacturing where, for instance, the semiconductor in a quantum well laser is strained to improve device performance (Adams, 2011). Secondly, we can use the strain sensitivity of the band gap to make novel strain or force sensing devices. In chapter 5, we will measure the effects of biaxial strain on the band gap of single and few layer MoS₂, work which I hope will contribute to making progress along both these routes.

The mechanics of atomically thin materials is a fascinating topic in its own right, and an understanding of how the dominant forces of adhesion and elasticity interact will be important for many of the applications so far mentioned. In chapter 6 we will investigate these forces, and discover that adhesion hysteresis plays an important role in understanding how atomically thin membranes peel off and on to their substrates.

1.4 Using atomically thin materials as separation membranes

Semiconductor electronics was the first nanotechnology become a large-scale technology, but will certainly not be the last. Diverse industries such as medicine, filtration, carbon capture and tribology are all hoped to be disrupted and improved by technologies than exploit the advantages to be gained by engineering materials at the

nanometer scale. In the final part of this thesis (chapter 7), we will investigate the use of atomically thin materials in one of these burgeoning technologies — the use of nanoporous materials for separating molecules by size with a sub-nanometer resolution.

Pristine graphene is impermeable to all atoms and molecules, and can act as a perfect barrier separating two reservoirs of gas or liquid (Bunch et al., 2008; P. Z. Sun et al., 2020). Holes can readily be introduced into the graphene by electron or ion irradiation, some with nanometer or even sub-nanometer diameters (Sahu & Zwolak, 2019). Such holes are referred to as *nanopores*, and are special because their diameters are small enough to be able to block larger molecules based on their size. Smaller molecules can pass through the pores relatively unimpeded, and thus a nanoporous membrane can function like a sieve, separating large molecules from small.

From a purely scientific perspective these nanopores are fascinating systems to study. They represent examples of flow and transport across the smallest possible apertures in nature, and are still far from fully understood. But there are big technological opportunities here too. Conventional membrane technologies such as reverse osmosis generally separates molecules based on a diffusive process where large molecules are removed from small ones based on their diffusion rate. In nanoporous membranes the larger molecules are not just slowed down by the membrane, they are strictly forbidden from passing it at all due to steric exclusion. Such membranes have the potential to be far more efficient than their conventional competitors. Such a breakthrough could have

important implications - an enhanced technology for filtering salt from water, or CO₂ molecules from industrial pollution, could play a role in tackling the severe humanitarian challenges of water scarcity and global warming (Cohen-Tanugi & Grossman, 2012).

My work in chapter 7 will involve measurements of the transport of ions across graphene nanopores in water, and in particular will describe some of the experimental artifacts that can lead to erroneous interpretation of these measurements. It is hoped this work will contribute a useful measurement technique to the field, which will help others make progress towards understanding these intriguing systems.

1.5 Outline

The majority of this thesis will be about investigating the mechanical properties of MoS₂ and the effect of strain on its band gap. As a result, a functional theoretical understanding of both mechanics and semiconductor physics is required to understand some of the experiments and results. My hope is that this thesis can still be read by budding mechanical engineers who want to learn about 2D semiconductors but have not yet encountered much (or have only a hazy memory of) solid state physics. I therefore dedicate chapter 2 to developing the key ideas needed to understand the basic electrical and optical properties of 2D semiconductors. This very brief introduction should provide a functional working model of the theory to the uninitiated. Chapter 3 covers the background mechanics of bulge testing, with chapter 4 covering the procedures for the

growth and transfer of 2D materials. Chapter 5 closely follows a paper published in *Nano Letters* **16**, 9 (2016), about strain engineering in atomically thin MoS₂. Chapter 6 is based on work also published in *Nano Letters* **17**, 9 (2017) about the mechanical stiffness and adhesion energy of MoS₂ on SiO_x substrates. Chapter 7 is based on work that contributed to the paper published in *Nanoscale* **11**, 9856 (2019), and involves probing the ion conductance of graphene nanopores using electrical and atomic force microscope (AFM) measurements. Chapter 8 contains unpublished work that may make up future directions of research, and my concluding remarks.

CHAPTER TWO: BASICS OF SEMICONDUCTOR PHYSICS

In this chapter I will introduce the basic elements of solid state physics, in the context of understanding the properties of the atomically thin semiconductors. The theoretical models in this chapter are described in more detail in several textbooks (Ashcroft & Mermin, 2003; Kittel, 2004; Simon, 2016).

2.1 The band gap and the Fermi energy

In developing an understanding of the atom, physicists had to uncover the structure of possible energy levels an electron may occupy. Similarly, in order to understand crystals, which are periodic arrays of atoms, we will need to have a model which describes the possible energy states an electron may have in the crystal. We will then be able to understand how electrons will behave at a microscopic level when we try and give them more energy through photons or electric fields, which will ultimately allow us to explain macroscopic phenomena such as the materials absorptivity and electrical conductance.

Free electrons can have a continuum of energies, with the kinetic energy E proportional to the square of the momentum \mathbf{k} , or $E \sim |\mathbf{k}|^2$. In atoms, electrons are confined in orbits around a nucleus and have quantized energy levels E_n but can carry no linear momentum. In a periodic crystal, electrons experience a little of both of these extremes: they are still attracted to nuclei, but are also allowed to move between atoms

and carry a momentum \mathbf{k} . The energy landscape of an electron in a crystal therefore preserves elements of both the limiting cases — the electrons have a discrete set of energy levels that they can occupy, called energy *bands*, and within each band the electron can take a quasi-continuous range of energy values.

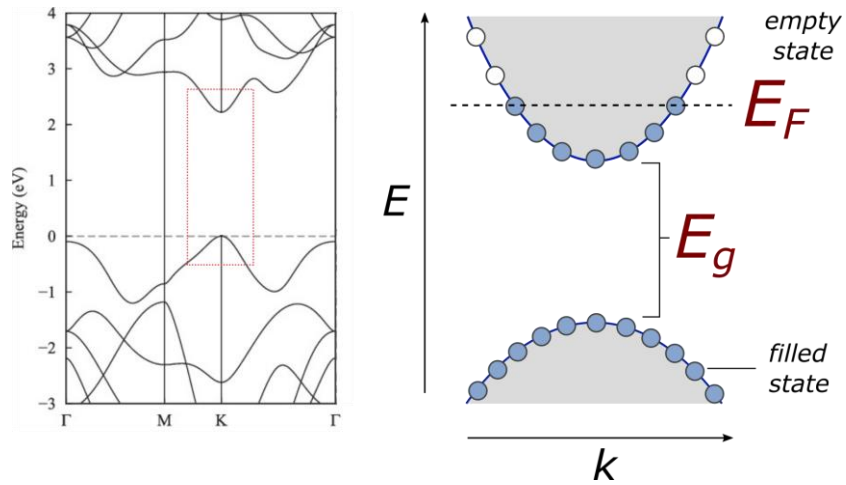


Figure 2.1 The electronic band structure of monolayer MoS₂ (Ellis, Lucero, & Scuseria, 2011), and a zoomed in cartoon of the band gap. The blue circles represent states occupied by electrons.

The band diagram of monolayer MoS₂ in Fig. 2.1 shows two bands which take a rather complicated shape as the momentum is varied in the x axis. The upper band in the figure is called the *conduction band*, and the lower one is the *valence band* (the other bands above and below them aren't very important). The bands are separated by a discrete gap between them. The most important region in the diagram is the point at which the valence band is highest and the conduction band is lowest, and the energy gap between the bands at this momentum (which is the so-called *K point* for 2D materials) is called the *band gap* E_g . In monolayer MoS₂, $E_g = 2.47$ eV (Hill et al., 2015). We can also note that, because in quantum physics momentum must be quantized, there are in fact

millions of momentum states that lie along each band, shown by evenly spaced circles in Fig 2.1 which represent states that an electron can fill. The separation between these states is extremely small, which is why \mathbf{k} is a quasi-continuous variable.

The electrons in the crystal fill up the lowest available energies first (like in an atom), and the highest energy electron in the pile is referred to as the Fermi energy E_F . The Fermi energy is not fixed, and can be increased or decreased by adding or removing electrons from the material, which is called *doping*. In un-doped MoS_2 the Fermi energy lies within the band gap. The value of E_F is significant because its position relative to the band gap in the band diagram plays a major role in determining the electrical and optical properties of the material. For this reason, E_F and E_g are the two most important numbers in this chapter.

2.2 Electronic properties of materials

Changing the value of E_F through doping causes the conductivity of the material to change too. If we add enough electrons to the MoS_2 for the Fermi energy to lie in the conduction band, the material will be (as the band name suggests) electrically conductive. The reason is that when an electric field is applied, the electrons near the Fermi energy change their momentum and energy to reflect their acceleration by the electric field. The new configuration, after a shuffling around of the available \mathbf{k} states, contains more electrons going right than left (Fig. 2.2a) and therefore a net current flows.

We can now try removing electrons from the system until the conduction band is empty and the valence band is full (Fig. 2.2b). When we apply an electric field now *it has no effect at all* on the electrons. This is because the electrons, being fermions, cannot occupy the same \mathbf{k} states, so when all the \mathbf{k} states in a band are filled the electrons can't shuffle around and change momentum. In this state the material has a very low conductance because the electrons cannot accelerate and carry a current.

If we remove even more electrons from the material, we find (a bit counterintuitively) that the conductance *increases* as the valence band is emptied (Fig. 2.2c). The empty \mathbf{k} states allow electrons to be accelerated by the E field and carry current. By convention, empty electron states in the valence bands are thought of as *holes*, basically particles in their own right which behave like a positively charged electron in a completely full (and therefore electronically inert) band of electrons.

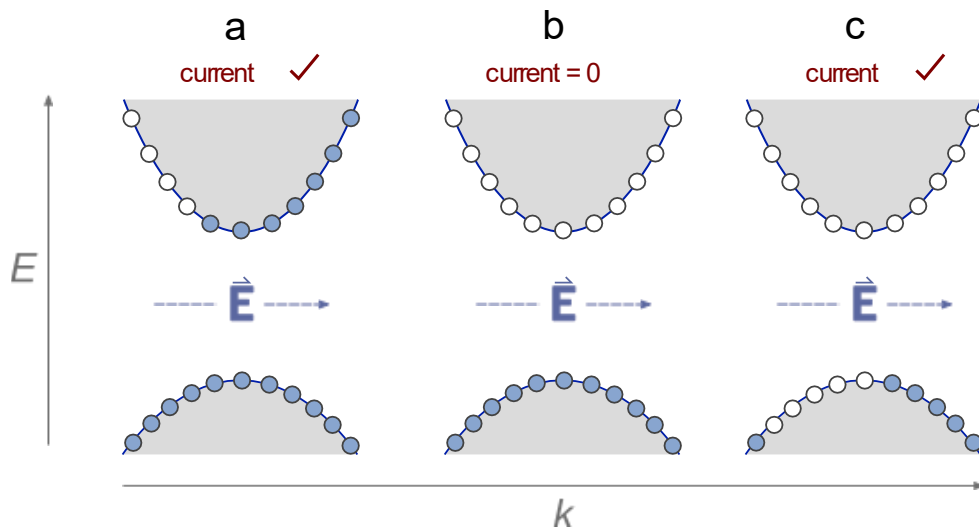


Figure 2.2 Depending on the Fermi energy, a material can have a high conductance (a & c) or a low conductance (b).

Materials can therefore carry positive or negative charge carriers (holes or electrons). The conductivity σ of the material depends on the total number of these charge carriers, given by

$$\sigma = ne\mu \quad \text{Eq. 2.1}$$

where n is the number of charge carriers, e is the charge of an electron, and μ is the electrical mobility of the charge carrier. For MoS₂ this number is $\sim 200 \text{ cm}^2\text{V}^{-1}\text{s}^{-1}$, and is reduced by defects in the crystal environment.

Finally, we can refine our understanding slightly by accounting for the temperature of the electrons, which spreads them out into a distribution of energies. It can be shown (Simon, 2016) that for a material with a mostly full valence band at temperature T , the number of electrons in the conduction band follows

$$n \propto T^{3/2} e^{-\frac{E_g}{2kT}} \quad \text{Eq. 2.2}$$

This equation shows that temperature allows some thermalisation of electrons from valence to conduction bands, but that the probability of an electron making this jump tails off exponentially with increasing E_g . For materials with empty conduction bands and a very large E_g , $n \rightarrow 0$, which (by considering Eq. 2.1) causes $\sigma \rightarrow 0$ too.

The importance of Eq. 2.2 for this thesis is that it tells us modulations to E_g will have a strong effect on the conductance (and other properties) of the semiconductor. This allows us to understand the results of Manzeli et al., 2015 who used mechanical strain to vary the strain sensitive band gap of MoS₂. Higher applied strains resulted in lower band gap energies, which in turn increased the conductivity (or lowered the resistivity) of the crystal (Fig. 2.3). This relationship between mechanical strain and conductivity could be used to dynamically measure strain in the material (a kind of piezoresistive strain gauge), or to simply modify the baseline properties of the material with statically induced strains. The idea of modifying E_g is in fact a widely used technique, and is in general referred to as *band gap engineering* which will be the subject of chapter 5.

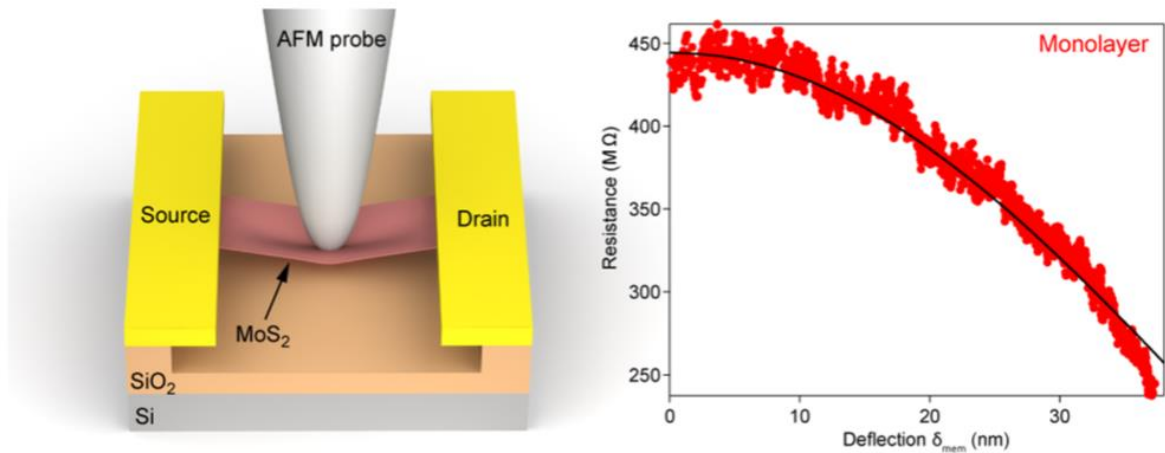


Figure 2.3 Changing the band structure of a crystal in turn affects its conductivity (Manzeli et al. 2015). Strain is applied to suspended MoS₂ which reduces its band gap energy, which increases its conductivity according to Eq. 2.2.

2.3 Photoluminescence, excitons, and the optical properties of MoS₂

Photoluminescence

The model outlined so far also helps us explain some optical phenomena that will be important later. When light is incident on a material, photons interact with its electrons. We will be concerned with the case of an electron in the valence band absorbing the energy of a photon and thereby gaining enough energy to jump into the conduction band (Fig. 2.4a). After absorption, the electron then scatters to reach the conduction band minimum before falling back down into the valence band by emitting a photon. This process is called *photoluminescence*.

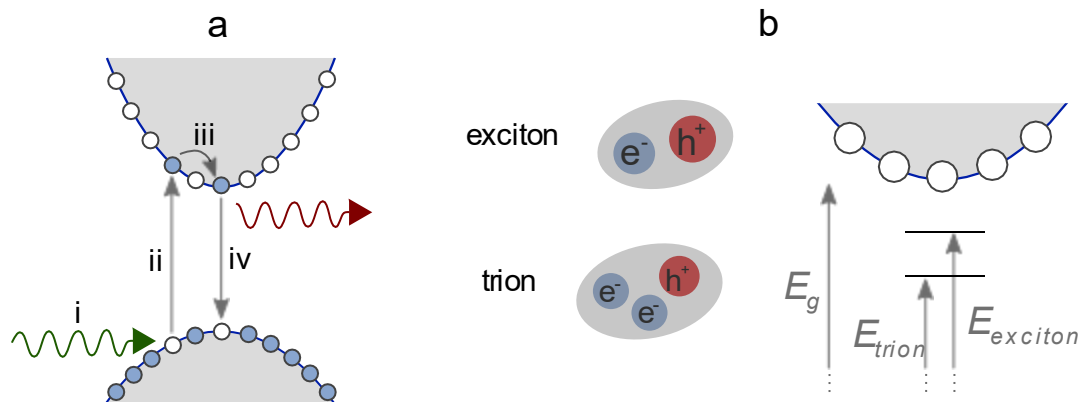


Figure 2.4 a) An electron in the valence band absorbs a photon (i), is excited into the conduction band (ii), scatters back down to the bottom of the conduction band (iii) and decays back down to the valence band by emitting a photon of lower energy than it absorbed (iv). b) Electrons bind to holes to form stable quasi-particles called *excitons*. An electron can bind to an exciton to form a *trion*. The binding energy of these particles mean they have an energy slightly lower than the conduction band.

In order for photoluminescence to occur, both momentum and energy must be conserved. To do this the electron's momentum must shift along the momentum axis by an amount equal to the momentum of the emitted photon. Photons carry very little momentum relative to electrons in crystals[†], so transitions must be basically vertical in the band diagram. This means that for strong photoluminescence to occur, the conduction band and valence band extrema must occur at the same location in \mathbf{k} space. Materials for which this is the case are called *direct gap semiconductors*, which include GaAs and monolayer MoS₂, and are excellent emitters of light for that reason. Indirect gap semiconductors (e.g. crystalline silicon and multilayer MoS₂) are those for which the band extrema have different \mathbf{k} 's, so are very poor emitters of light and cannot be used for applications such as LED's. The difference in single layer and multilayer MoS₂ photoluminescence will turn out to be useful in chapter 4, where it will allow us to quickly distinguish monolayer from multilayer samples.

Excitons

When an electron has been excited into the conduction band, a vacancy or positively charged *hole* remains in the valence band. Remarkably, the electron and the newly formed hole can form bound states called *excitons*, where the mutual electrostatic attraction keeps the pair in an orbit somewhat analogous to a hydrogen atom. In fact, the

[†] The electron momentum has a value of the order $k_e = 2\pi/a$, where a is the lattice constant that is typically several Angstroms. For semiconductors with $E_g \sim 1\text{eV}$ the photon energy to excite electrons across the gap must be approximately $k_{ph} = 1 \text{ eV}/\hbar c$. Such a photon therefore has a momentum $\sim 10^4$ times smaller than that of a typical electron momentum.

physics of excitons is so similar to hydrogen that we can use the same description developed by Rydberg to account for its binding energy. Thus, for a stationary exciton, its energy can be written,

$$E_{exciton} = E_g - \frac{Ry^*}{n_B^2} \quad \text{Eq. 2.3}$$

where n_B is bound state energy quantum number and Ry^* is the Rydberg energy of the exciton (Rigosi, 2016). In MoS_2 $Ry^* = 440$ meV (Hill et al., 2015), which is enormous compared to most semiconductors (typically, $Ry^* < 200$ meV). This is because the 2D nature of the material means the electrostatic field lines binding the electron and hole can mostly travel through the free space on either side of the crystal, so the excitons therefore experience a much weaker electrostatic screening compared to those in 3D crystals.

With this understanding of excitons we can slightly improve upon our model of optical transitions. When an electron is excited across the band gap, it can form an exciton state with an energy slightly lower than E_g (Fig. 2.4b). The exciton state can decay when the electron falls back to the valence band, with a photon emitted according to Eq. 2.3 with an energy slightly less than E_g . Because optical measurements often show this apparent reduction in the band gap, the energy $E_{exciton}$ is sometimes referred to the *optical band gap*, to distinguish it from the *electronic band gap* E_g . In MoS_2 the optical band gap is 1.9 eV.

To add yet more detail, in monolayer MoS₂ an even lower energy bound state also exists, called the *trion*, which is formed when a neutral exciton binds to an electron (Fig. 2.4b). The trion has negative charge and a larger binding energy than excitons (Mak et al., 2013), but apart from that they act in much the same way for the purposes of this thesis.

Optical properties of MoS₂

We can now use the optical signatures of a semiconductor, in our case monolayer MoS₂, to deduce its underlying electronic band structure. There are two primary ways to do this, using either light emission or light absorption. *Absorption spectroscopy* entails measuring the fraction of light of different wavelengths that is absorbed by a material. The absorption spectrum of MoS₂ is shown in Fig. 2.5a, which has two distinct peaks, which are caused by the production of excitons at those energies. MoS₂ has two conduction bands right next to each other, split by the spin-orbit interaction, which means that there are two possible exciton states with similar energies called the *A* and *B* excitons. At energies beneath the optical band gap, little light can be absorbed, whereas at higher energies the electrons have enough energy to span the band gap and the absorbance is therefore large.

We can also probe the electronic band structure of MoS₂ by measuring the light emitted by the material, with the method of *photoluminescence spectroscopy*. The sample is irradiated with 2.33 eV photons, which is enough energy for excitons to be formed.

After excitons decay the emitted light is collected in a spectrometer and plotted as in Fig 2.5b. We can again see two peaks for the monolayer sample, showing intense emission of light at 1.9 and 2.1 eV which are again signatures of the *A* and *B* excitons (the *B* peak has a much lower intensity than the *A*). Multilayer MoS₂ crystals with a thickness of ≥ 2 layers have much weaker emission, and also have an additional *I* peak in the spectrum at around 1.6 eV (Fig. 2.5b). The difference between the PL in single and multilayer MoS₂ is due to differences in band structure – monolayers are direct gap semiconductors while multilayers have indirect band gaps. Multilayers have an additional peak due to electron decay across this indirect gap, and have a PL intensity roughly x1000 weaker than the direct gap monolayers.

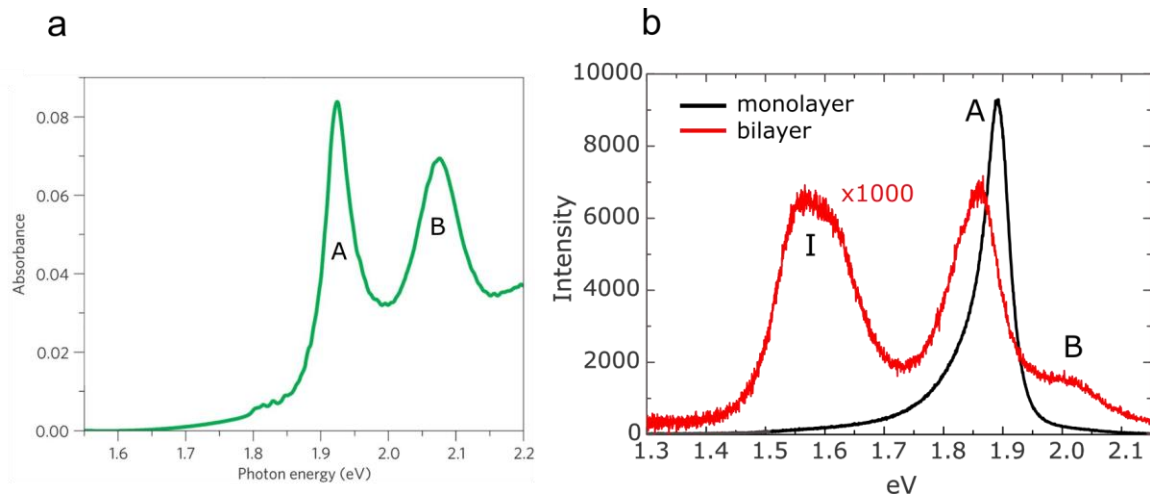


Figure 2.5 a) Absorption spectrum of monolayer MoS₂, taken at 10K with a -100V gate voltage (Mak et al. 2013). b) Photoluminescence spectrum of monolayer and bilayer MoS₂ (taken at room temperature). Both curves have peaks corresponding to the *A* and *B* excitons, and the bilayer has the additional *I* peak caused by emission across the indirect band gap. The bilayer curve has been scaled by a factor of x1000 for comparison.

2.4 Raman scattering and spectroscopy

Acoustic waves can propagate through solid materials[‡], with the energy carried via the movement and potential energy of the atoms they consist of. In crystals these vibrational waves have a quantum mechanical equivalent called *phonons*, which are thought of as discrete particles produced by lattice vibrations. Just like we saw for electrons, the periodic structure of the lattice puts restrictions on the possible energies and momenta that these phonons can carry, which can be represented as a *phonon band structure*. Fig. 2.6a shows the phonon band diagram for monolayer MoS₂, with each band corresponding to a particular vibrational mode of the crystal. The lower set of bands (blue) are due to vibrations in which the whole unit cell oscillates (called acoustic modes), and the higher set of bands (red) caused by atomic vibrations within each unit cell (optical modes). The most important modes are the A_{1g} and the E¹_{2g} (Fig. 2.6b) which correspond to out-of-plane and in-plane modes respectively.

These modes can be detected optically by the phenomenon of *Raman scattering*. An incoming photon can scatter off a crystal phonon, with the outgoing photon carrying a slightly different energy and momentum to ensure these quantities are conserved. We can then collect the scattered light and pass it through a spectrometer to see the intensity of the scattered light as a function of wavelength. This is *Raman spectroscopy*, and a Raman

[‡] Confirmed independently by the author in a sealed bedroom adjacent to Green Line construction work. The experiment ran nightly for 6 months; data and expletives were submitted to Brookline town hall and remain under review.

spectrum for monolayer MoS₂ is shown in Fig 2.6c. The data is plotted with the x axis being the ‘Raman shift’ – the difference in energies of the incoming and outgoing light – in units of wavenumber (cm^{-1}) because the shifts are typically of very low energy. For monolayer MoS₂, A_{1g} and E¹_{2g} peaks have wavenumbers of 404 cm^{-1} and 384 cm^{-1} respectively.

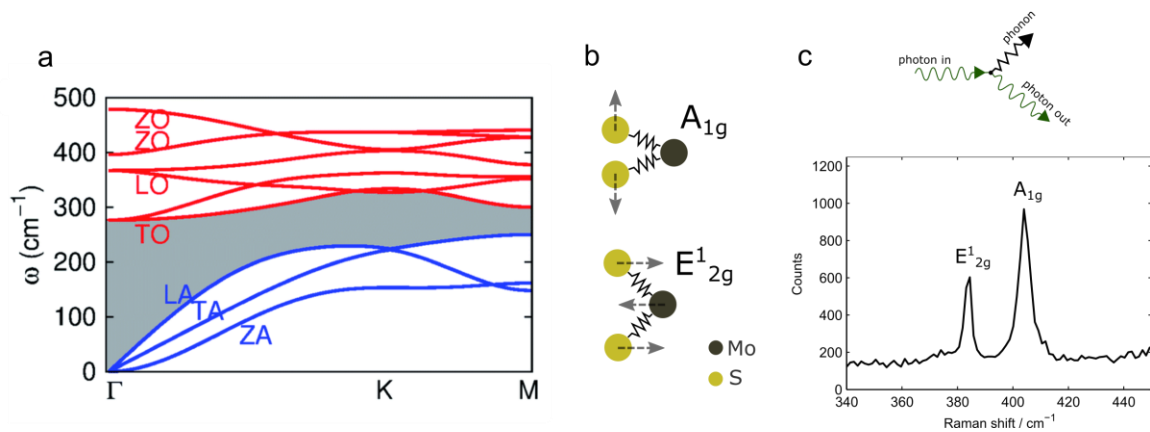


Figure 2.6 a) The phonon band structure (J. W. Jiang, 2014). The labels represent types of mode, e.g. LA = longitudinal acoustic. b) Schematic of the main vibrational modes, and c) Raman peaks of MoS₂.

The primary use of Raman spectroscopy is for identifying crystals and molecules by their distinctive pattern of Raman peaks. In 2D materials research it is also extremely helpful for determining the thicknesses of samples. The addition of just single atomic layers to a 2D crystal will typically change the energy or intensity of its Raman peaks, because of the effects of either optical interference, van der Waals forces, stacking induced structural changes, or others (C. Lee, Yan, et al., 2010). For MoS₂, the separation between the two modes increases with each additional layer (Fig. 2.7a), a fact that was used extensively in chapter 4 for confirming the thicknesses of CVD grown samples. The

Raman peaks are also sensitive to electrical doping and mechanical strain. Fig. 2.7b shows a splitting of the E'_{2g} Raman mode, as uniaxial strain breaks the symmetry of the crystal and reduces the spring constant between Mo and S atoms in one direction. We will investigate the effect of biaxial strain on the Raman mode energies in chapter 5.

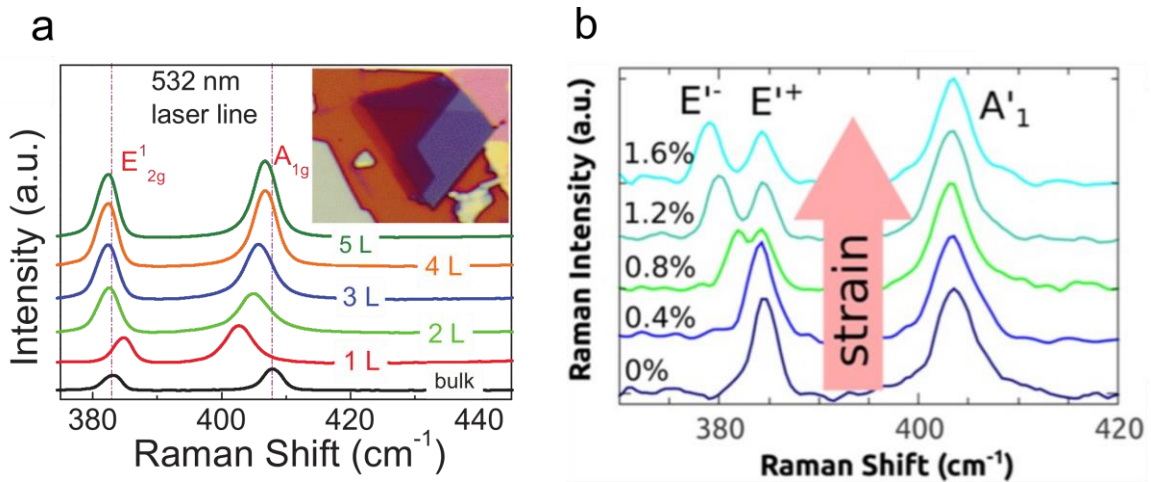


Figure 2.7 a) The separation between the two Raman modes increases with MoS₂ layer thickness (H. Li et al., 2012). b) The Raman peaks are also effected by mechanical strain (Conley et al., 2013a).

2.5 Spectroscopy experimental setup

All Raman and PL measurements in this thesis were taken with a Renishaw Raman InVia microscope. A schematic for the optics of this machine is shown in Fig. 2.8a. Light from a 532 nm CW laser is focused on to the sample with a 100x objective, producing a spot size of $\sim 1 \mu\text{m}$. Photons emitted by photoluminescence (PL), or scattered by Raman scattering, pass back through the objective and on to a diffraction grating. This acts like a prism to spread the beam out into different angles as a function of

the wavelength. The beam is then directed onto a CCD camera which can measure the relative intensity of each wavelength. We use a 600 lines/mm grating for PL measurements and a higher resolution 2400 lines/mm grating for Raman spectroscopy.

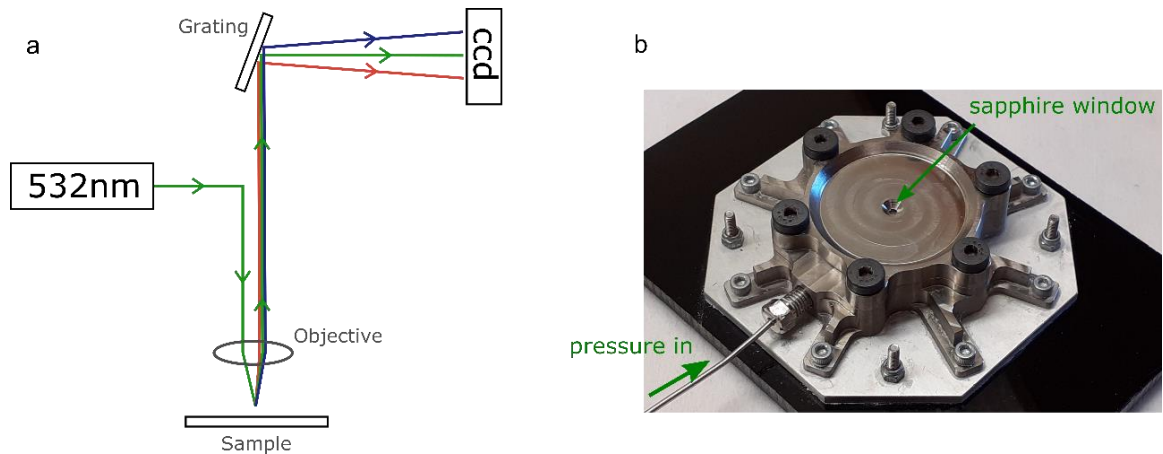


Figure 2.8 a) Raman microscope schematic. b) Pressure chamber which allows Raman and PL measurements to be taken on pressurized samples.

Some measurements in chapter 5 use a custom-built pressure chamber with a sapphire optical window (Fig. 2.8b). This allows spectroscopic measurements to be taken while subjecting the samples to up to 15 atm of gas pressure. For these measurements I used a 50x long working distance objective to focus on the sample.

CHAPTER THREE: NANOMECHANICS

Later chapters will be concerned with using pressure to deform atomically thin membranes in order to investigate their mechanical properties. In this chapter I will outline the mechanics that we will use to model this interaction between pressure and deformation. Much of the theory I will cover has already been thoroughly discussed in previous theses[§], so I will introduce only the most important concepts and equations here, along with any novel material not covered in those works.

3.1 Bulge testing

Bulge testing is a method that can be used to interrogate, among other things, a materials Young's modulus, adhesion energy, and residual stresses (Beams, 1959; Koenig, 2013). It involves fixing the material of study over an aperture or cavity, and applying a pressure difference across it, which induces a deformation in the material which can be measured (Fig. 3.1a). By measuring this deformation response over a range of pressures, one can deduce mechanical constants of the material, provided one has a model which can connect these two variables: the pressure difference and the deformation.

In our case we will use the *Hencky model*, which describes isotropic membranes that are suspended over circular apertures, and subject to a uniform pressure (Fichter,

[§] See Scott Bunch 2008, Steven Koenig 2013, Xinghui Liu 2014.

1997). The model accounts only for lateral loading of the membrane since the radial component of the pressure is omitted to simplify the analysis. The effect of this omission is negligible for the range of parameter space relevant to the experiments in this thesis. I will trace an outline of the Henky's solution here, with the discussion closely following Fichter, 1997. The basic idea of the model is to assume the meridional stress σ_r , and the vertical deflection profile $z(r)$ of the membrane can be approximated as an infinite summation of even powers of radius r .

$$\sigma_r = \frac{1}{4} \left(\frac{\Delta p a_0}{Et} \right)^{2/3} \sum_0^\infty b_{2n} \left(\frac{r}{a_0} \right)^{2n} \quad (\text{Eq. 3.1})$$

$$z(r) = a \left(\frac{\Delta p a_0}{Et} \right)^{1/3} \sum_0^\infty c_{2n} \left(1 - \left(\frac{r}{a_0} \right)^{2n+2} \right) \quad (\text{Eq. 3.2})$$

with a pressure difference Δp , cavity radius a_0 , 3D Young's modulus E , and membrane thickness t . A profile of $z(r)$ is shown in Fig. 3.1a. We will solve the governing equations of the system to find the coefficients b_{2n} and c_{2n} in these two equations.

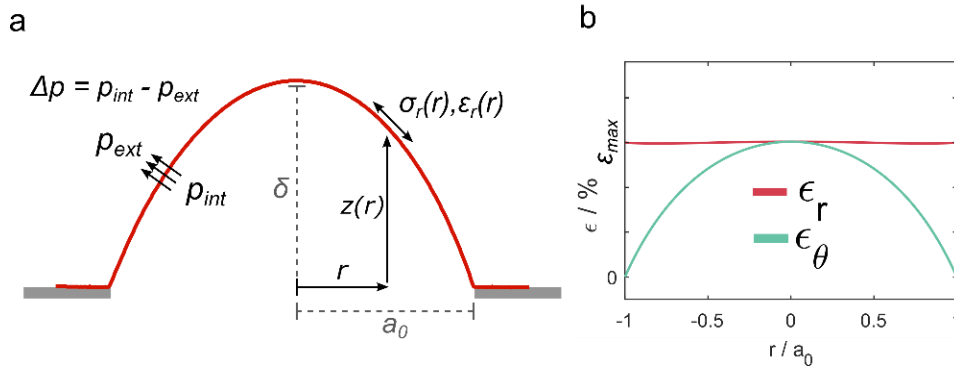


Figure 3.1 a) A membrane subjected to a pressure difference across a sealed aperture. b) The radial and tangential strains in the membrane as a function of radius r . At $r = 0$ the membrane experiences biaxial strain.

By assuming the uniform lateral loading of the membrane, the governing equations can be written in terms of radius r and pressure difference Δp as,

$$\sigma_r \frac{dz}{dr} = -\frac{\Delta p r}{2} \quad (\text{Eq. 3.3})$$

$$\sigma_\theta = \frac{d}{dr}(r\sigma_r) \quad (\text{Eq. 3.4})$$

which represent the equations for static equilibrium. We also have the linear stress-strain relationships,

$$\sigma_r - \nu\sigma_\theta = Et\varepsilon_r \quad (\text{Eq. 3.5})$$

$$\sigma_\theta - \nu\sigma_r = Et\varepsilon_\theta$$

The coefficients b_{2n} and c_{2n} are found by plugging Eq. 3.1 & Eq. 3.2 into Eqs. 3.3-3.5 under the boundary condition that the deformation is zero at the clamped edge ($r = a_0$). These equations were solved using a MATLAB code for $n = \{0, \dots, 10\}$.

Armed with these coefficients we can now relate the pressure difference across the membrane Δp to the maximum height of the bulge $\delta \equiv z(r=0)$. From Eq. 3.2 we can write

$$\delta = a_0 \left(\frac{\Delta p a_0}{Et} \right)^{1/3} \sum_0^\infty c_{2n} \quad (\text{Eq. 3.6})$$

and tidy this up a bit further by setting the summation to a constant $K(\nu)$ and setting $Et \equiv E_{2D}$, the 2D Young's modulus^{**}. Our simplified equation now reads

$$\Delta p = \frac{K(\nu)E_{2D}\delta^3}{a_0^4} \quad (\text{Eq. 3.7})$$

We will use this relationship in chapter 6 to measure E_{2D} for single and multilayer MoS₂ experimentally. It will also be useful for us later to find the volume created beneath the bulge V_b , by integrating $z(r)$ in Eq. 3.2 over the radius $0 \rightarrow a_0$. Doing so yields

$$V_b = C(\nu)\pi a_0^2 \delta \quad (\text{Eq. 3.8})$$

where $C(\nu)$ is a constant produced by a summation of c_{2n} 's. The constants C and K depend only on the Poisson's ratio ν , and their values for various 2D materials are tabulated in Table 3.1.

	Poisson's Ratio ν	$K(\nu)$	$C(\nu)$
MoS ₂	0.29 (Cooper et al., 2013)	3.54	0.522
Graphene	0.16 (Blaklee, Proctor, Seldin, Spence, & Weng, 1970)	3.09	0.524
hBN	0.22 (Peng, Ji, & De, 2012)	3.28	0.523
Black Phosphorus	0.4 (J.-W. Jiang & Park, 2014)	4.07	0.519

Table 3.1 Values for constants $C(\nu)$ and $K(\nu)$ for several 2D crystals, calculated using Hencky's solution.

^{**} The 2D Young's modulus is generally used for 2D materials where the true value of the thickness t becomes spurious. Where can the edge of a one atom thick crystal be said to begin?

We can also calculate the strain distribution in the device using Eqs. 3.1, 3.4 and 3.5, which is plotted in Fig. 3.1b. The region around $r = a_0$ is purely uniaxial strain, and the region at $r = 0$ is purely biaxial. We can derive the relationship between δ , a_0 , and the biaxial strain in the center of the device $\varepsilon_b \equiv \varepsilon_r(r=0)$, by combining Eq. 3.1 and Eq. 3.5. The final expression for biaxial strain is then written as,

$$\varepsilon_b = \left(\frac{\delta}{a_0}\right)^2 \frac{b_0(v)(1-v)K(v)^{2/3}}{4} \quad (\text{Eq. 3.9})$$

in terms of two numerical constants b_0 and K which both depend only on Poisson's ratio v . For MoS₂ we have $v = 0.29$, which leads to $K = 3.54$ and $b_0 = 1.72$. We can further simplify Eq. 3.9 to have a single proportionality constant and write

$$\varepsilon_b = \sigma \left(\frac{\delta}{a_0}\right)^2 \quad (\text{Eq. 3.10})$$

For MoS₂ we have a value of $\sigma = 0.709$. Note that if one simply assumes the bulge is spherical, one can quickly derive the same expression with $\sigma = 2/3$ (X. Liu, 2014). We will use Eq. 3.10 substantially in chapter 5.

3.2 Measuring the adhesion energy

The adhesion energy Γ of a membrane to its substrate can also be found with the bulge testing method (Koenig, Boddeti, Dunn, & Bunch, 2011; Wan & Mai, 1995). When a critical pressure is applied, the membrane will begin to delaminate from the substrate,

as pressure forces overcome the adhesive forces clamping the membrane to the substrate. In this case the membrane not only increases its vertical deflection δ , but also the radius of the bulge a so that $a > a_0$.

This section closely follows Koenig, 2013 and Boddeti, 2014, but with the model adapted to include the interesting additional effect of *adhesion hysteresis* in these systems. This effect refers to the cases when the energy required to separate the membrane from the surface Γ_{sep} is greater than the energy returned to the system as the membrane re-adheres Γ_{adh} , with $\Gamma_{adh} < \Gamma_{sep}$. We will begin by considering just Γ_{sep} which determines the mechanics of the membrane delamination under applied pressure. We will then include Γ_{adh} , which allows us to model occasions when the pressure is reduced and the membrane begins to stick back down to the substrate.

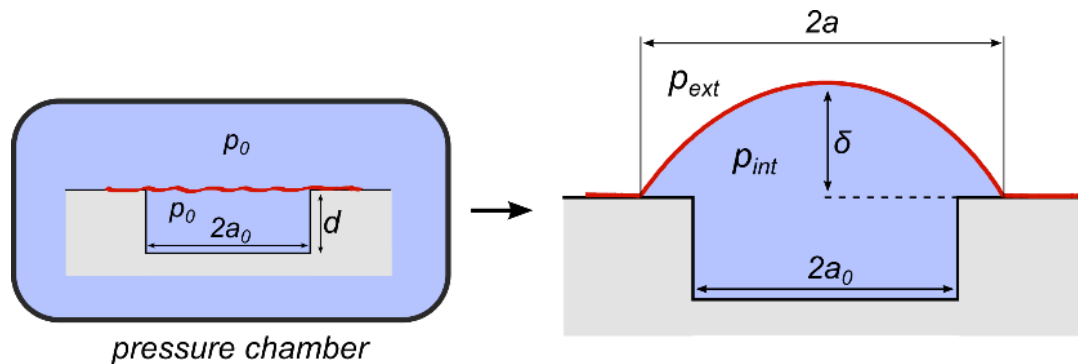


Figure 3.2 A sealed cavity is filled with pressurized gas after being left to equilibrate in a pressure chamber at p_0 as the gas leaks slowly through the substrate. When it is removed the bulge expands and the internal pressure reduces. The membrane can also delaminate ($a > a_0$).

The adhesion energy can be measured using a membrane suspended over a cavity (Fig. 3.2). The cavity can be filled with pressurized gas by placing it in a chamber at

pressure p_0 and allowing the gas to equilibrate by slowly diffusing through the partially permeable cavity substrate. The cavity contains a fixed number of gas molecules during the deformation and delamination process; for this reason this is referred to as a *constant N blister test* (Wan & Mai, 1995). We will use a free energy model to understand the mechanics of this system, writing the total free energy of the system F as,

$$F = \frac{(p_{int}-p_{ext})V_b}{4} + \Gamma\pi(a^2 - a_o^2) - p_o V_o \ln \left[\frac{V_o+V_b}{V_o} \right] + p_{ext}V_b \quad (\text{Eq. 3.11})$$

where V_o is the initial volume of the cavity, V_b is the additional volume created as the bubble expands. Γ is equal to Γ_{sep} in the case of delamination. The first two terms represent the elastic strain energy and the work to separate the membrane from the substrate respectively, and the final two terms account for the isothermal expansion of the gas.

After the pressure differential $p_{int} - p_{ext}$ has been established, the bubble volume expands until the free energy of the system F reaches a local minimum. We find this minimum by taking the derivative of F with respect to a , and substituting the pressure terms for the Hencky's result in Eq. 3.7 (with $\Delta p = p_{int} - p_{ext}$) yielding,

$$\frac{dF}{da} = 2\pi a \left[\Gamma - \frac{5}{4}CKE_{2D} \left(\frac{\delta}{a} \right)^4 \right] \quad (\text{Eq. 3.12})$$

Setting this formula equal to zero to find the radius at which the free energy is minimized leads to,

$$\Gamma_{sep} = \frac{5}{4}CKE_{2D} \left(\frac{\delta}{a}\right)^4 \quad (\text{Eq. 3.13})$$

Using this expression, we can determine Γ_{sep} of each device by measuring δ and a of the bubble with an AFM for any device that has begun to delaminate ($a > a_0$). This allows Γ_{sep} to be determined from δ and a without knowing p_0 , which avoids the long waiting times required for devices to reach equilibrium in the pressure chamber. Alternatively, the expression can be written including pressure terms, by rearranging and using the relationship $p_0V_0 = p_{int}(V_0 + V_b)$, to give

$$\Gamma_{sep} = \frac{5C}{4} \left(\frac{p_0V_0}{V_0 + V_b(\delta, a)} - p_{ext} \right) \delta \quad (\text{Eq. 3.14})$$

which allows us to measure Γ_{sep} by using the charging pressure of the pressure chamber p_0 , plus measured values of δ and a . We will use Eq. 3.13 and Eq. 3.14 extensively in chapter 6.

As the charging pressure p_0 is increased, the radius a of the device will increase. We can now understand this in terms of our free energy model by plotting $F(a)$ in Fig. 3.3a, which shows that the radius of the device changes to minimize the free energy for each pressure. As the pressure increases the radius of the device gradually increases. Depending on the geometry of the device, the delamination can initially occur via a discrete jump, which we call a *snap-out instability*.

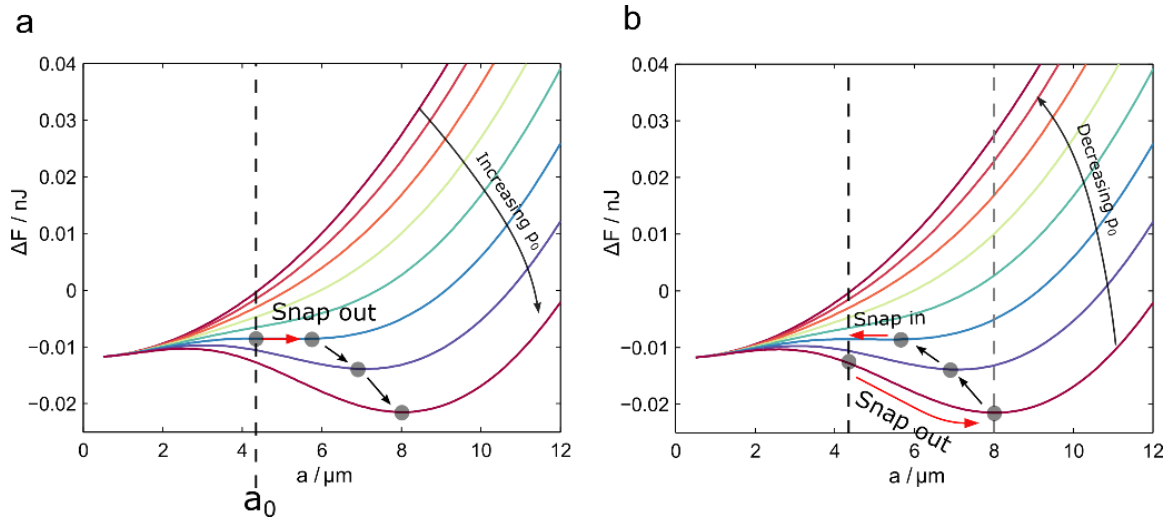


Figure 3.3 a) The free energy $F(a)$ as a function of radius a for different charging pressures p_0 . The grey circles represent the minimum of each curve corresponding to a given pressure p_0 . **b)** The expected trajectory of the device if the pressure reduces after delamination.

We can also consider the case that the membrane delaminates followed by a reduction in pressure. Under the assumption that the pressure changes very slowly, the device would be in quasi-equilibrium at all times. Given this, we would expect the device to minimize the free energy at each point as before, and so simply follow the reverse trajectory as shown in Fig. 3.4b. After the initial snap-out instability, the pressure reduces and the minimum point smoothly moves to a smaller radius until a critical point where there is no longer a valley in the free energy diagram. The free energy is then reduced the most (at this pressure) by the radius reducing fully to the radius of the cavity. We refer to this as a *snap-in instability*.

3.3 Membrane re-lamination and adhesion hysteresis

This model assumes that the adhesion energy remains constant throughout the experiment, however it has been found that for a wide range of adhesion phenomena, this is not always an accurate assumption. For instance, when a liquid is deposited on a surface a droplet will form with a contact angle determined by adhesive forces of the liquid and substrate. These are material properties that we would expect to remain constant, and so the contact angle should be constant too. If we reduce the volume of the droplet with a pipette, we find however that the contact angle does change (Fig. 3.4a), which is called *contact angle hysteresis*. This is analogous to the adhesion hysteresis we will explore in chapter 6, where there is a dramatic asymmetry between the geometry of our devices depending on whether they are being inflated or deflated. Fig. 3.4b shows that upon deflation, a device radius can remain pinned at a fixed radius before snap-in, which is contrary to the predictions of the model described in the last section.

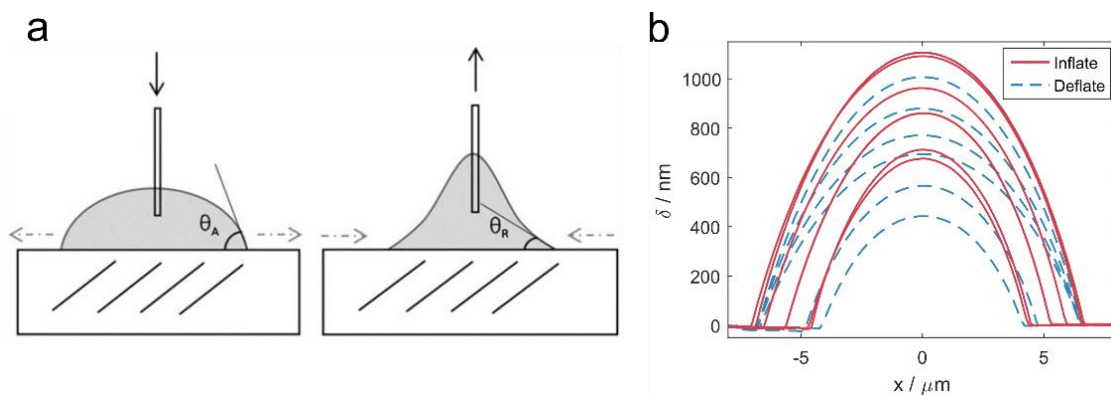


Figure 3.4 a) Contact angle hysteresis in sessile liquid drop experiment (Nowak, Combes, Stitt, & Pacek, 2013). b) Analogous behavior in delaminated pressurized membranes as the pressure is reduced. The radius of the device gradually increased as the device was inflated, but remained mostly pinned at a constant radius whilst it deflated.

The goal of this section will be to account for this phenomenon by adding the effects of adhesion hysteresis to the previous analysis. We do this by adding some new criteria for changes of the device radius Δa ,

$$\Gamma = \begin{cases} \Gamma_{adh}, & \Delta a < 0 \\ \Gamma_{sep}, & \Delta a > 0 \end{cases} \quad \& \quad \Gamma_{adh} < \Gamma_{sep} \quad (\text{Eq. 3.15})$$

which determines Γ for re-lamination and delamination respectively. When the membrane delaminates it minimizes F as before. But when the pressure reduces, the system can no longer lower its energy as much by reducing a , since the adhesion energy is smaller with $\Gamma = \Gamma_{adh}$. The free energy landscape now looks like Fig. 3.5, which is created by plotting Eq. 3.11 with different Γ according to the criteria in Eq. 3.15. In this example the device radius initially delaminates to 8 microns, where it remains pinned whilst the pressure is reduced due to the local free energy minimum it remains trapped in. We call this pinned radius a_p . Thus as the pressure reduces, only the deflection δ decreases according to Eq. 3.7, which can be seen in Fig 3.4b. When deflating, the radius a of the device will only decrease when $dF/da > 0$ for $\Delta a < 0$ (with $\Gamma = \Gamma_{adh}$) in order for the free energy to always be minimized. This point occurs when the dashed lines in Fig 3.5 turn horizontal. From examining Eq. 3.12 and considering that $\Gamma_{adh} < \Gamma_{sep}$, we can see this criterion will only occur when δ has decreased to below a critical value of $\delta = \delta_c$ after which the device radius can reduce in the form of a snap-in transition. The critical deflection δ_c marks the point where $dF/da = 0$ for $\Delta a < 0$ (i.e. $\Gamma = \Gamma_{adh}$), and from using Eq. 3.12 we can see that this occurs when the relationship,

$$\Gamma_{adh} = \frac{5}{4}CKE_{2D}\left(\frac{\delta_c}{a_p}\right)^4 \quad (\text{Eq. 3.16})$$

is satisfied. This equation allows us to determine Γ_{adh} by measuring a_p and δ_c , the deflection of the membrane right before re-lamination.

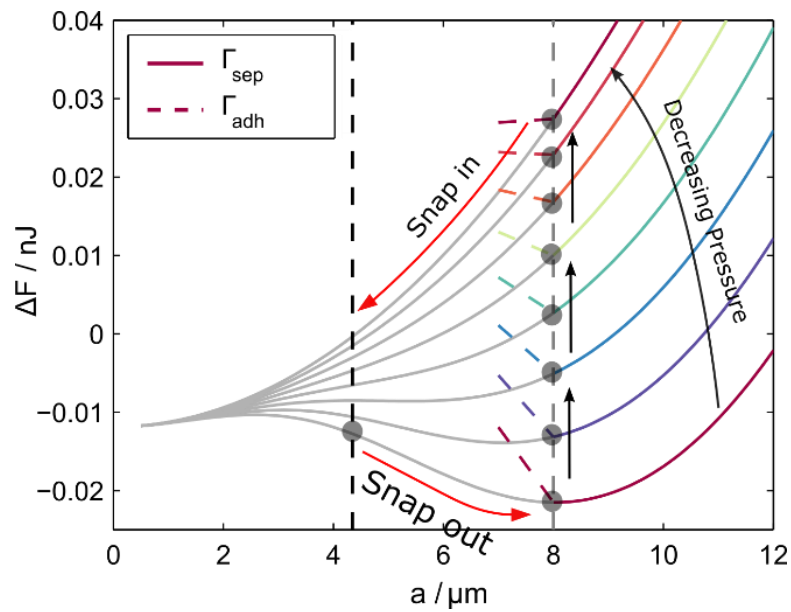


Figure 3.5. The modified free energy landscape if $\Gamma_{adh} < \Gamma_{sep}$. As the device reduces its radius its free energy is determined by the dashed lines. The device is now trapped in a free energy minima and snap-in only occurs when the gradient of the dashed line is greater than zero.

CHAPTER FOUR: CVD GROWTH AND CHARACTERIZATION

In this chapter I will describe methods for the large-scale growth of monolayer MoS₂ crystals. I will also cover how we fabricated devices of suspended MoS₂ crystals over micro-cavities in SiO_x, and the growth optimization methods we used to improve the yield of our samples.

4.1 Growing and transferring atomically thin semiconductors

Graphene and MoS₂ monolayers were first isolated using the ‘Scotch tape method’ of mechanical exfoliation. The method is simple and low cost, and produces very high quality samples. It is, however, time consuming and low yield, and generally produces only a handful of atomically thin crystals after several hours of labor. It was later discovered (X. Li et al., 2009) that single layer graphene could be reliably grown over large areas of copper foil by chemical vapor deposition (CVD), which was an essential step towards making graphene an economically viable material for commercial applications. Following in the footsteps of graphene, there are now many different CVD recipes that have been developed to grow large monolayer domains of MoS₂ and other TMDs (Zhang et al., 2019), which has facilitated research in the field and demonstrated that scalable production of the material is possible.

We initially used the most commonly used growth method of ambient pressure CVD, which uses MoO_3 and S_2 precursors (van der Zande et al., 2013). After the membranes grown with this method were transferred to the bulge test geometry described in chapter 3 we found that they were permeable to gas, which must be due to the presence of defects or tears produced during either the growth or transfer stage. To grow impermeable monolayer MoS_2 , we use a modified version of the growth method described in Wu et al., 2013. A powder source of MoS_2 is placed in the center of a furnace, and a SiO_x substrate is placed in a cooler region downstream. The SiO_x is cleaned with acetone, IPA, water and UV-Ozone for 5 mins immediately prior to the growth. The system is pumped down to 10 mTorr to remove any contaminating gases after which we flow 60 sccm Ar as a carrier gas, plus 0.065 sccm of O_2 and 1 sccm of H_2 gas. The furnace is heated to 900 °C and held at that temperature for 15 minutes after which it is left to cool naturally to room temperature. The O_2 and H_2 gases are turned off after the temperature is below ~650 °C to avoid any unwanted reactions with the grown material.

We found when using a fresh MoS_2 powder source, the first growth tends to produce a very low coverage of MoS_2 monolayers. When the powder is reused for the second and third growths, the coverage is optimum, with growth yields deteriorating for subsequent uses. After the third growth run we dispose of the used MoS_2 and replace it with fresh powder.

The process described in Wu et al., 2013 flows only argon gas, and depends on the sublimation of MoS_2 at the hottest part of the furnace which is carried downstream and condenses on the substrate in a cooler region. We found the PVD method to be very unreliable and usually produced only small monolayer domains of $\sim 20\mu\text{m}$ side length, which were too small for our purposes. The addition of small amounts of oxygen and hydrogen greatly improved the yield, leading to a large monolayer coverage with triangular grains of side length as large as $150\mu\text{m}$. The likely mechanism for this improvement is that the O_2 reacts to form either MoO_2 or MoO_3 , thus liberating 2S . These molecules then flow downstream to react on the surface of the substrate. This method may therefore be analogous to several other methods in the literature in which a molybdenum oxide and sulfur powder precursors are used.

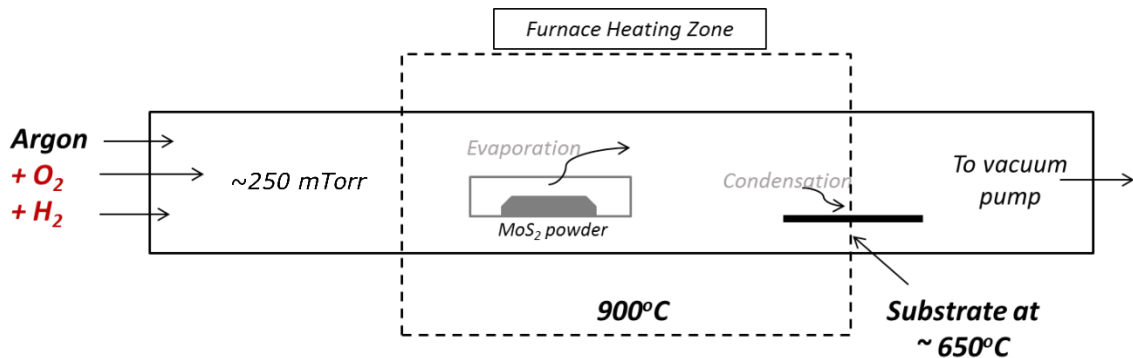


Figure 4.1 Vacuum furnace set up. Results are improved by adding O₂ and H₂.

Membranes produced by our modified CVD technique are highly impermeable to gas, and can sustain very high strains across large areas (this will be discussed in chapter 5). This means that they have a low density of defects or vacancies, and that pressurized

gas can be used to deform the membranes using the bulge test geometry described in chapter 3. An example of a typical triangular domain of monolayer MoS₂ can be seen in Fig. 4.2a.

After the growth the MoS₂ crystals need to be transferred to the target substrate – in our case a SiO_x wafer containing RIE etched microcavities. The following transfer process is a modified version of that described in Suk et al., 2011. After the growth we spin A3 950 PMMA on the growth wafer at 900 rpm, followed by a 5 min bake on a hotplate at 90 °C. This should be done as soon as possible after the growth to avoid any degradation of the membranes in air. We then cut a hole in a piece of thermal release tape (TRT), which is just smaller than the size of the wafer. The TRT is centered and stuck on the wafer, and this stack is then placed in a dish containing ~2” of water. The surface tension of the water keeps the stack afloat. The water gradually seeps between the PMMA and the SiO_x until the wafer drops away, leaving the MoS₂ on the PMMA window. The TRT (with a PMMA window) is carefully removed without damaging the PMMA, and left to dry for > 30mins. The target substrate is thoroughly cleaned in O₂ plasma and UVO (this improves the adhesion to the PMMA) and is placed on a hotplate at 120 °C. The TRT is placed on the substrate, where the PMMA melts and sticks to it (this can be encouraged by poking it down with some tweezers). If the PMMA doesn’t stick down, we increase the temperature until it does (usually 180 °C is enough for most substrates). The TRT should have detached at this point and can be peeled off. The sample can then be annealed at 340 °C for 6 hours in a vacuum furnace flowing Ar : H₂ ;

200 : 100 sccm to remove the PMMA.

When our substrates contain microcavities air gets trapped beneath the MoS_2 membranes. The trapped oxygen then destroys the membranes during the annealing process. To avoid this, we place the devices in a vacuum desiccator for 2 days after the transfer, to allow the oxygen to leak out through the SiO_x . A result of a typical transfer to microcavities is shown in Fig. 4.2b.

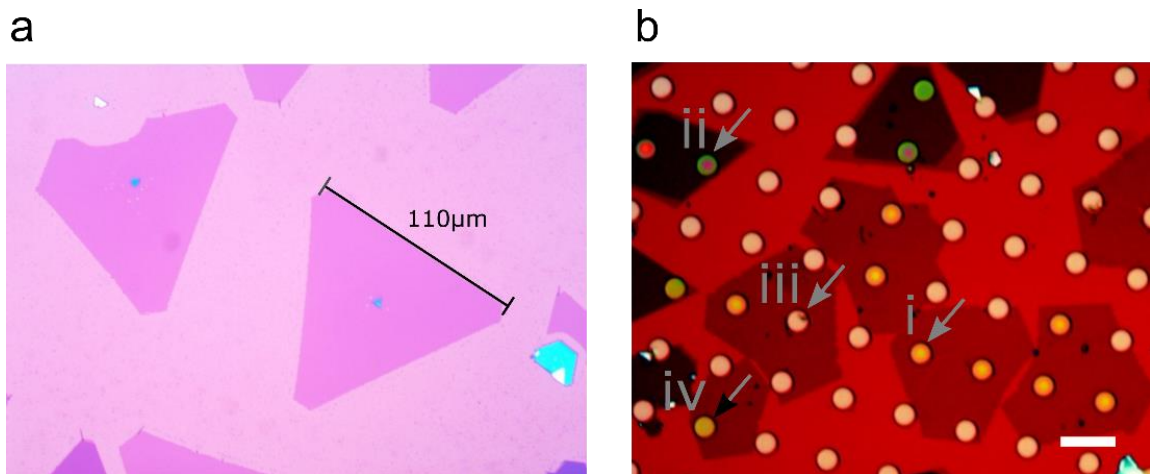


Figure 4.2 a) A typical growth of large monolayer MoS_2 domains on a SiO_x substrate. Additional layers tend to grow outwards from the initial crystal seed in the center of each grain. b) A transfer to an array of microcavities. The yield can immediately be determined using an optical microscope. The colored rings in i) show that these monolayer membranes are bulging down and are therefore impermeable. ii) shows the same for a bilayer. iii) shows a broken device and iv) shows a suspended device with no Newton rings – this device is therefore permeable and is likely torn. Scale bar is 20 μm .

4.2 Characterizing membrane strength and quality

The ideal CVD growth would produce perfect monolayer crystals with no crystal defects of any kind. The reality is unfortunately much messier. While MoS₂ crystals can be grown that have the expected Raman and PL signatures, one cannot determine from these parameters alone whether the membrane is immaculately crystalline or as holey as Swiss cheese. Growth optimization depends on accurate and rapid characterization – without this feedback it becomes impossible to know whether tweaks to the growth recipe are helping or hindering. This section includes a few possible characterization techniques to aid the process of getting this feedback and refining the growth method.

Transfers to microcavities

The most useful method for the purposes of this thesis was to transfer membranes to arrays of micro-cavities and to measure the yield of suspended and impermeable devices that survive the transfer process. This yield can be determined within a couple of minutes after growth by using an optical microscope to count the number of devices that have a tell-tale Newton ring pattern, as shown in Fig 4.2b. These rings are produced by interference when the membrane is bulged down towards the bottom of the cavity. The membranes are only bulged down when there is a vacuum pressure within the cavity (produced during the vacuum anneal), and this vacuum can only be maintained if the membrane is somewhat impermeable. Thus the Newton rings indicate a slow leak rate of

gases across the membranes after growth. Tweaking growth parameters to optimize the yield of such devices is a good way to get membranes that are of high mechanical strength and that contain few large pores or tears.

Membrane gas permeability

For a closer examination of the density of nanoscale pores, one can also measure the exact permeability of these devices by measuring the leak rates out of the cavities for a set of different gas species. Fig. 4.3a shows the how the maximum membrane deflection δ slowly reduces when gas leaks out of a sealed microcavity. Using the Hencky model described in chapter 3, we can derive the rate at which gas molecules are leaving the sealed micro-cavities. By comparing to data presented in Koenig et al., 2012, we found that the best MoS₂ membranes measured had a permeability roughly equivalent to that of pristine graphene (Fig 4.3b). This suggests a complete absence of even sub-nanometer scale defects, however the PMMA residue introduced during the MoS₂ dry transfer may be blocking any pores that are present, which would render them invisible with this method. Data like that in Fig. 4.3 however, does prove the absence of the larger 10–100nm pores.

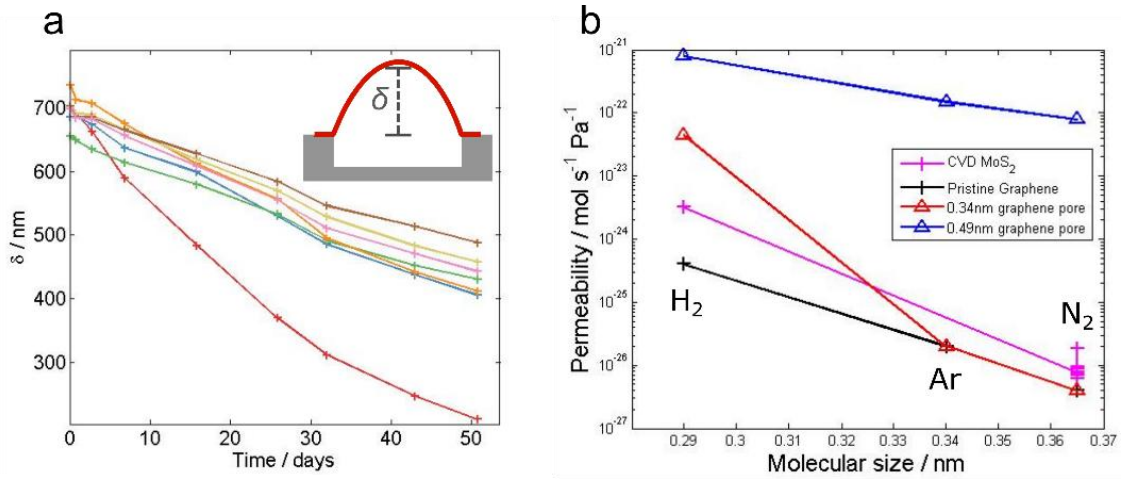


Figure 4.3 a) Most devices measured had extremely low gas permeabilities, so that devices left out in ambient conditions remained inflated for several months. Different colors represent different devices. b) Gas permeability plotted against gas molecular size. We compare the CVD grown MoS₂ membranes to the pristine and nanoporated graphene samples presented in Koenig et al., 2012. The data suggests CVD grown MoS₂ has a permeability roughly comparable to pristine graphene.

Photoluminescence spectroscopy

Finally, the PL can be used to give some indication of the defect density of the grown membranes by monitoring the intensity of the PL peak in monolayer crystals. O₂ or N₂ molecules can adsorb to and react with MoS₂, forming defects which change the doping level of the crystal and provide stable binding sites for excitons to avoid non-radiative recombination (Nan et al., 2014), and thus enhancing the PL intensity. S₂ or Mo vacancies or substitutions also dope the crystal (Suh et al., 2014), which can also affect the PL intensity (Lien et al., 2019). Therefore, very high or very low PL signals indicate that there may be a high density of defects of one of these kinds. For instance, Fig. 4.4 shows an MoS₂ crystal grown in a furnace which contained a leak that allowed extra O₂

and N₂ molecules to be present during growth, which resulted in a PL intensity which is more than an order of magnitude larger than seen in normal growths or exfoliated samples.

Samples with such an enhanced PL were found in general to produce a much lower yield of suspended impermeable membranes, likely because the increased defect density was causing this PL enhancement. PL spectroscopy can therefore be a handy way to discard abnormal samples early and to indicate leaks in the system. This method should be used with caution however, since the PL intensity is sensitive to a range of competing influences, and so is best used to check only that the PL intensity is not egregiously abnormal.

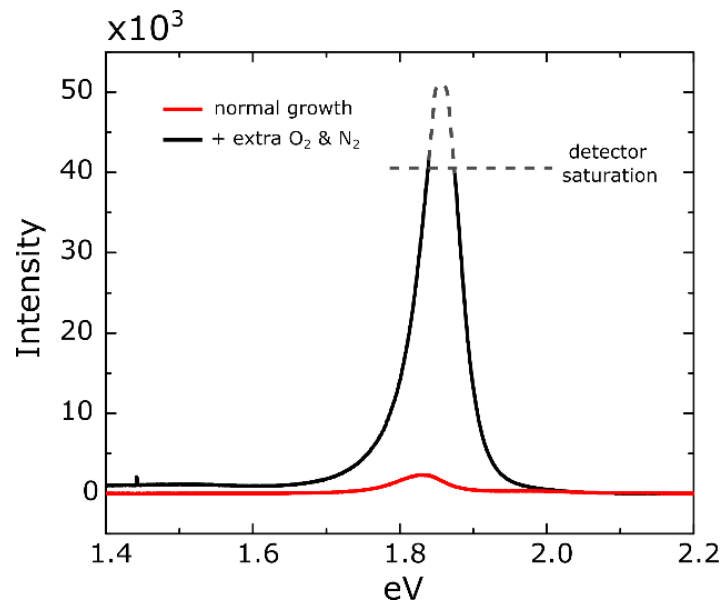


Figure 4.4 The PL enhancement of membranes that were exposed to additional O₂ and N₂ gas during growth. The PL intensity of the black curve saturated the detector – the dashed line is an estimate of the true maximum intensity.

Transmission electron microscopy

Transmission electron microscopy (TEM) has the resolution to resolve individual atoms in a crystal, so can be used to accurately measure the crystal defect density. By transferring MoS₂ samples to SiN_x chips with through-holes, we could use TEM to confirm that our crystals are largely free of defects Fig. 4.5a, although some single atom vacancies could be detected Fig. 4.5b. There were also occasionally much larger defects such as Fig. 4.5c, which take on shapes corresponding to the symmetry of the crystal.

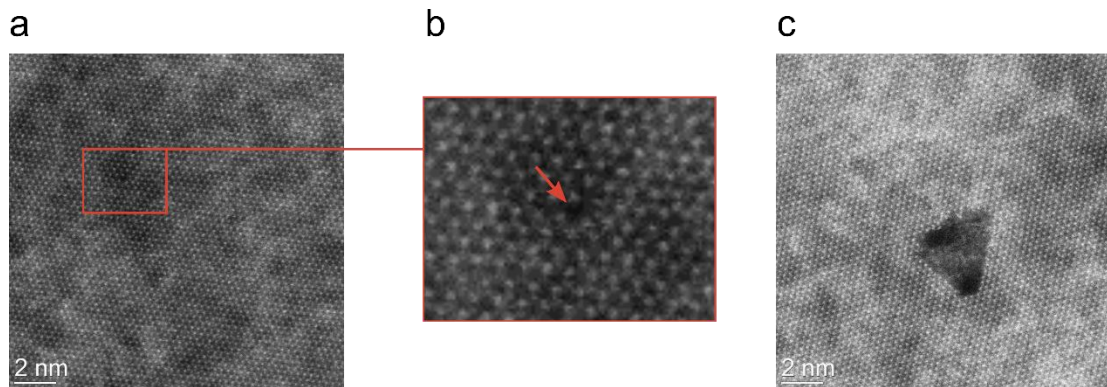


Figure 4.5 a) TEM image of CVD grown monolayer MoS₂. There are some single atom vacancies (b) and in some samples are larger nm scale defects (c). The white dots are Mo or S atoms in a hexagonal lattice, with the white haze caused by hydrocarbon contamination stuck to the surface of the membrane.

Unfortunately, the long preparation time and scarce access to TEM's means that this characterization method is in most cases impractical, at least for the initial optimization. Many hundreds of growths are required to dial in the good parameters, so the alternative techniques described above were in the end far more valuable.

4.3 Optimized growth parameters and troubleshooting

Sometimes projects may be better suited to different growth parameters. Here is a short guide to tweaking the gas flow parameters of the growth to get growths of either i) large individual grain size ii) large monolayer coverage or iii) high mechanical strength membranes.

i) Large individual grain size

Ar : O₂ : H₂ : (N₂)
60 : 1.5 : 1 : (0.025) sccm

Adding lots of O₂ always results in a much larger deposition of material on the SiO_x wafer. Individual grains of many 100's of microns in side length can be grown this way. Membranes grown with these settings have a very high PL intensity, due to doping likely produced by defect sizes introduced by the O₂, and also tend to be mechanically weak.

One can also add a small amount of N₂ which seemed to encourage large monolayer grain sizes.

ii) High monolayer coverage

Ar : O₂ : H₂
60 : 0.065 : 10 sccm

As monolayer MoS₂ grows outward from the nucleation point, additional layers frequently begin to seed above the initial layer and form a terraced multilayer structure. We found that adding more H₂ suppresses the growth of the additional layers, resulting in a high coverage of monolayer film.

The downside is that the apparently continuous film actually consists of fairly small grains ($<10\ \mu\text{m}$). The film is very weak at the grain boundaries, which nearly always break if suspended over a cavity.

iii) High mechanical strength

*Ar : O₂ : H₂
60 : 0.065 : 1 sccm*

We settled on these parameters by optimizing for the highest yield of suspended and impermeable devices after transfer to an array of microcavities (described in the last section). These settings produce a fair amount of multilayer MoS₂, but targeting a higher monolayer coverage reduced the overall yield of suspended membranes.

I found the best strategy for improving the membrane yield strength was to add as little O₂ as possible (while still retaining a workable growth coverage), in order to reduce the number of crystal defects caused by oxidation.

In normal operation the CVD growths should be quite reliable. The best way to ensure consistency is to make sure anything that goes in and out of the tube is clean, and to be vigilant for signs of any air leaks in the system. Replacing the tube and fixing leaks is time consuming and should be avoided as much as possible. Below is a troubleshooting table to get the system up and running quickly if problems appear, and also some fixes for transfer issues.

Growth troubleshooting table

Problem	Solution
No growth / very small monolayer growth yield	<p>The most likely cause is a leak somewhere in the system, particularly at the seals between the quartz tube and the CF flange adapters. Use He leak tester to check for leaks.</p> <p>This can also happen when the MoS₂ powder source is old. Try using freshly bought powder, and always store it in a vacuum desiccator.</p> <p>Another cause is that there is too much growth material deposited on the tube at the downstream end of the furnace. Every few weeks/months you can shift the furnace a couple of inches upstream, so the growth substrate is in an area of clean quartz again. Then see the next problem...</p>
Low yield after changing tube or shifting furnace	<p>The deposited MoS₂ on the quartz tube seems to be necessary to get the best growths. The clean tube needs to be 'worn in' by doing a growth with a 30 min hold at 900 °C. Replace the powder after this and continue as normal.</p>
Non-crystalline material (colored rings, speckles etc) are deposited all over the sample	<p>Contamination is getting in the tube. Anything going inside the tube (substrate, the crucible, and the sample rod) must be kept clean. If the problem persists with the cleanest substrate, try cleaning the tube and crucible with O₂ annealing. Flow 0.6 sccm O₂ and 20 sccm Ar at 1000 °C in vacuum for about an hour. Contaminants should be picked up and condense downstream.</p>

Table 3.1

Transfers trouble shooting table

Problem	Solution
PMMA window doesn't stick to the target substrate	<p>Clean the substrate thoroughly in O₂ plasma at a high power, then (if possible) do UVO treatment right before transfer.</p> <p>Increase the hotplate temperature. The cost of doing so is that the higher temperatures cause the PMMA to become more fluid, which can result in more stretching/tearing/crumpling of the membranes during the transfer.</p>
PMMA window breaking easily due to e.g. the water surface tension	Spin a thicker layer of PMMA (700rpm – 1200rpm is a good range to consider).
PMMA residue is not fully removed by annealing	Check the PMMA bottle isn't expired or contaminated
The PMMA window doesn't peel off the growth wafer	Do the transfers soon after the PMMA has dried. It seems to stick to the wafer more if left for a few days.
Membranes keep breaking	<p>Check for wrinkles and tears in the transferred membranes, which suggest the PMMA is stretching too much during the transfer.</p> <p>Check the membranes in an optical microscope before the transfer whilst they are still on the PMMA windows. With the right PMMA thickness they should be visible. You can then check if they are already damaged by this point in the procedure.</p> <p>Modify growth parameters (see above)</p>

Table 3.2

CHAPTER FIVE: BAND GAP ENGINEERING WITH ULTRA-LARGE BIAXIAL STRAINS IN SUSPENDED MONOLAYER MoS_2

In this chapter we will demonstrate the continuous and reversible tuning of the optical band gap of suspended monolayer MoS_2 membranes by as much as 500 meV by applying very large biaxial strains. By using chemical vapor deposition (CVD) to grow crystals that are highly impermeable to gas, we are able to apply a pressure difference across suspended membranes to induce biaxial strains. We observe the effect of strain on the energy and intensity of the peaks in the photoluminescence (PL) spectrum, and find a linear tuning rate of the optical band gap of 99 meV / %. This method is then used to study the PL spectra of bilayer and trilayer devices under strain, and to find the shift rates and Grüneisen parameters of two Raman modes in monolayer MoS_2 . Finally, we use this result to show that we can apply biaxial strains as large as 5.6% across micron sized areas, and report evidence for the strain tuning of higher level optical transitions.

5.1 Introduction

The ability to produce materials of truly nanoscale dimensions has revolutionized the potential for modulating or enhancing the physical properties of semiconductors by mechanical strain (J. Li, Shan, Ma, & Editors, 2014). Strain engineering is routinely used in semiconductor manufacturing, with essential electrical components such as the silicon transistor or quantum well laser using strain to improve efficiency and performance

(Adams, 2011; Y. Sun, Thompson, & Nishida, 2007). Nano-structured materials are particularly suited to this technique, as they are often able to remain elastic when subject to strains many times larger than their bulk counterparts can withstand (T. Zhu & Li, 2010). For instance, bulk silicon fractures when strained to just 1.2%, whereas silicon nanowires can reach strains of as much as 3.5% (Lugstein, Steinmair, Steiger, Kosina, & Bertagnolli, 2010). Parameters such as the band gap energy or carrier mobility of a semiconductor, which are often crucial to the electronic or photonic device performance, can be highly sensitive to the application of only small strains. The combination of this sensitivity with the ultra-high strains possible at the nanoscale could lead to an unprecedented ability to modify the electrical or photonic properties of materials in a continuous and reversible manner.

Monolayer MoS₂, a 2D atomic crystal, has been shown in both theory (T. Li, 2012; Steinhoff et al., 2015) and experiment (Castellanos-Gomez et al., 2013; Conley et al., 2013b; He, Poole, Mak, & Shan, 2013; Plechinger et al., 2015; Yeung Yu Hui, Xiaofei Liu, Wenjing Jie, Ngai Yui Chan, Jianhua Hao, Yu-Te Hsu, Lain-Jong Li, Wanlin Guo, 2013) to be an ideal candidate for strain engineering. It belongs to the class of 2D transition metal dichalcogenides (TMD's), and as a direct-gap semiconductor (Mak et al., 2010) has received significant interest as a channel material in transistors (Radisavljevic, Radenovic, Brivio, Giacometti, & Kis, 2011a), photovoltaics (Tsai et al., 2014) and photodetection (H. S. Lee et al., 2012) devices. It has a breaking strain of 6-11% as measured by nanoindentation, which approaches its maximum theoretical strain

limit (Bertolazzi, Brivio, & Kis, 2011) and classifies it as an ultra-strength material. Its electronic structure has also proven to be highly sensitive to strain, with experiments showing that the optical band gap reduces by ~ 50 meV / % for uniaxial strain (Conley et al., 2013b; He et al., 2013), and is predicted to reduce by ~ 100 meV / % for biaxial strain (Peelaers & Van De Walle, 2012; Scalise, Houssa, Pourtois, Afanas'ev, & Stesmans, 2012). This reversible modulation of the band gap could be used to make wavelength tunable phototransistors (H. S. Lee et al., 2012), or MoS₂ strain sensors that have a sensitivity comparable to their state of the art silicon counterparts (Manzeli, Allain, Ghadimi, & Kis, 2015b). Moreover it has been suggested that strain could also improve the performance of MoS₂ transistors (S. Yu, Xiong, Eshun, Yuan, & Li, 2015), or could be used to create broadband light absorbers for energy harvesting (Ji Feng, Qian, Huang, & Li, 2012).

The effect of strain on the band gap of 2D TMD's has been reported in a number of studies (Castellanos-Gomez et al., 2013; Conley et al., 2013b; Manzeli et al., 2015b; Nayak et al., 2014; Plechinger et al., 2015; Roldan, Castellanos-gomez, & Cappelluti, 2015; Yeung Yu Hui, Xiaofei Liu, Wenjing Jie, Ngai Yui Chan, Jianhua Hao, Yu-Te Hsu, Lain-Jong Li, Wanlin Guo, 2013), including uniaxial strains of up to ~ 4 % (Y. Wang et al., 2015) and biaxial strains of up to ~ 3 % produced in highly localized sub-micron areas (H. Li et al., 2015). Band gap shifts in MoS₂ of ~ 300 meV have been induced by using very large hydrostatic pressures (Nayak et al., 2015), and tensile strain has induced shifts of as much as ~ 100 meV (Conley et al., 2013b). However, the

combination being both an ultra-strength material and having a band gap highly sensitive to strain imply that a much larger band gap tuning must be possible. By contrast, tensile strain has been used to reduce the band gap by as much as 290 meV in 1D nanowires (Signorello, Karg, Björk, Gotsmann, & Riel, 2013).

In this paper, we use a geometry which allows us to take the first measurements of the Raman mode and band gap shift rates of suspended MoS₂ membranes under large biaxial strains, and study single and multilayer samples prepared by both CVD and mechanical exfoliation. We conclude that micron scale CVD grown monolayer MoS₂ can be biaxially strained by over 5% resulting in an optical band gap reduction of ~500 meV, or over 25%.

5.2 Device geometry

Our geometry exploits the fact that monolayer MoS₂, like graphene, is impermeable to all standard gases (Bunch et al., 2008). By applying a pressure difference across a MoS₂ membrane suspended over a cylindrical cavity (Fig. 5.1a) a bulge is formed, and this deformation produces a biaxial strain at the center of the device. To fabricate our devices, we first suspend MoS₂ films over cylindrical micro-cavities etched into a SiO_x/Si substrate by the transfer of CVD grown MoS₂ using a PMMA transfer method (Suk et al., 2011). Fig 5.1b shows a typical transfer with a high yield of undamaged suspended devices. We used a novel CVD growth recipe (see chapter 4 for

details) which produces highly impermeable monolayer membranes. With our best growths, a single transfer can produce several hundred suspended monolayer devices which are impermeable to the larger gas species.

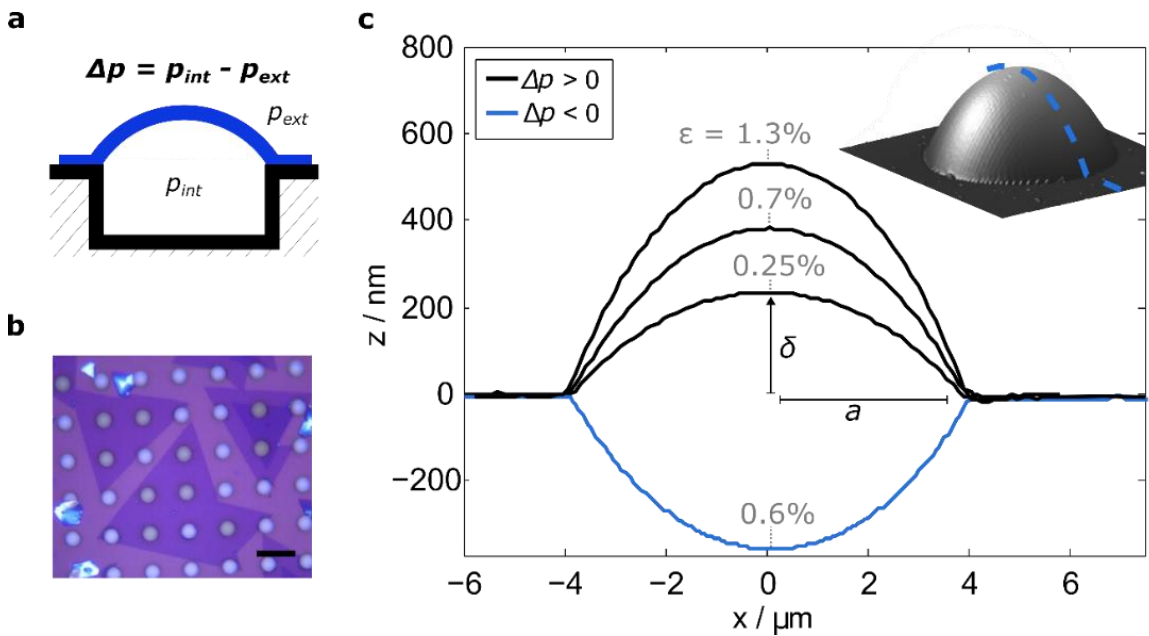


Figure 5.1 a) Device schematic. b) A typical sample of CVD grown MoS₂ membranes suspended over cylindrical cavities after transfer (scale bar is 20 μm). c) An AFM cross section of a device at various p_{int} , resulting in different biaxial strains at the center of the device. Devices can be bulged up or down depending on whether Δp is positive or negative.

Fig. 5.1c shows atomic force microscopy (AFM) cross sections of one of these devices under ambient external pressures ($p_{ext} = p_{atm}$) but with increasing internal pressures (p_{int}), resulting in increasing center membrane deflections δ . The device can be bulged up ($\delta > 0$) or down ($\delta < 0$) depending on whether the pressure difference across the membrane, $\Delta p = p_{int} - p_{ext}$, is positive or negative. We vary p_{int} by placing the devices in a chamber filled with pressurized N₂ gas, which is able to slowly diffuse through the

silicon oxide substrate and into the sealed micro-cavities. They are left there for several days until p_{int} equilibrates with the pressure of the N_2 gas (Bunch et al., 2008). After the devices are removed from the chamber, the new p_{int} results in a different δ and biaxial strain ε in the center of the device.

Following Hencky's model for circular, pressurized membranes with a negligible bending stiffness (Fichter, 1997), the biaxial strain produced at the center of the device can be written as,

$$\varepsilon = \sigma(\nu) \left(\frac{\delta}{a}\right)^2 \quad (\text{Eq. 5.1})$$

where $\sigma(\nu)$ is a numerical constant which depends only on Poisson's ratio ν (see supporting information). For MoS_2 we take the value of $\nu = 0.29$ (Cooper et al., 2013), resulting in $\sigma = 0.709$. This model has been shown to accurately describe graphene membranes in this geometry (Koenig et al., 2011). We can therefore measure ε at each p_{int} by using an AFM to find δ and a , and by varying the magnitude of p_{int} we can take optical measurements of the band gap and Raman shifts over a range of known strains.

5.3 Strain tuning the band gap and Raman modes

We first studied the effect of strain on the PL of CVD and mechanically exfoliated monolayer devices, and Fig. 5.2a shows the PL spectra of a monolayer device over the range of 0 – 2% biaxial strain. We incrementally increased p_{int} up to ~0.75 MPa

corresponding to a strain of $\sim 2\%$, and at successive pressures a PL, Raman and AFM measurement was taken. At higher p_{int} , the membranes begin to delaminate from the surface as the force from Δp overcomes the adhesion to the substrate (Koenig et al., 2011), which limits the maximum possible strain with $\Delta p > 0$ to $\sim 2\%$. Membranes in this geometry may slide at the edge of the well under high pressure (Kitt et al., 2013), however we only present data for devices which show no evidence of significant sliding (see appendix Fig. A1). For optical measurements we used a 532 nm laser with a spot size of $\sim 1 \mu\text{m}$ in diameter. Our devices were $8 \mu\text{m}$ in diameter, allowing us to focus the laser spot only on the region of biaxial strain in the center of the device. We observed that the PL peak redshifted with increasing strain and also rapidly decreased in intensity, consistent with previous work (Conley et al., 2013b) and theoretical predictions (Steinhoff et al., 2015) (see appendix Fig. A2).

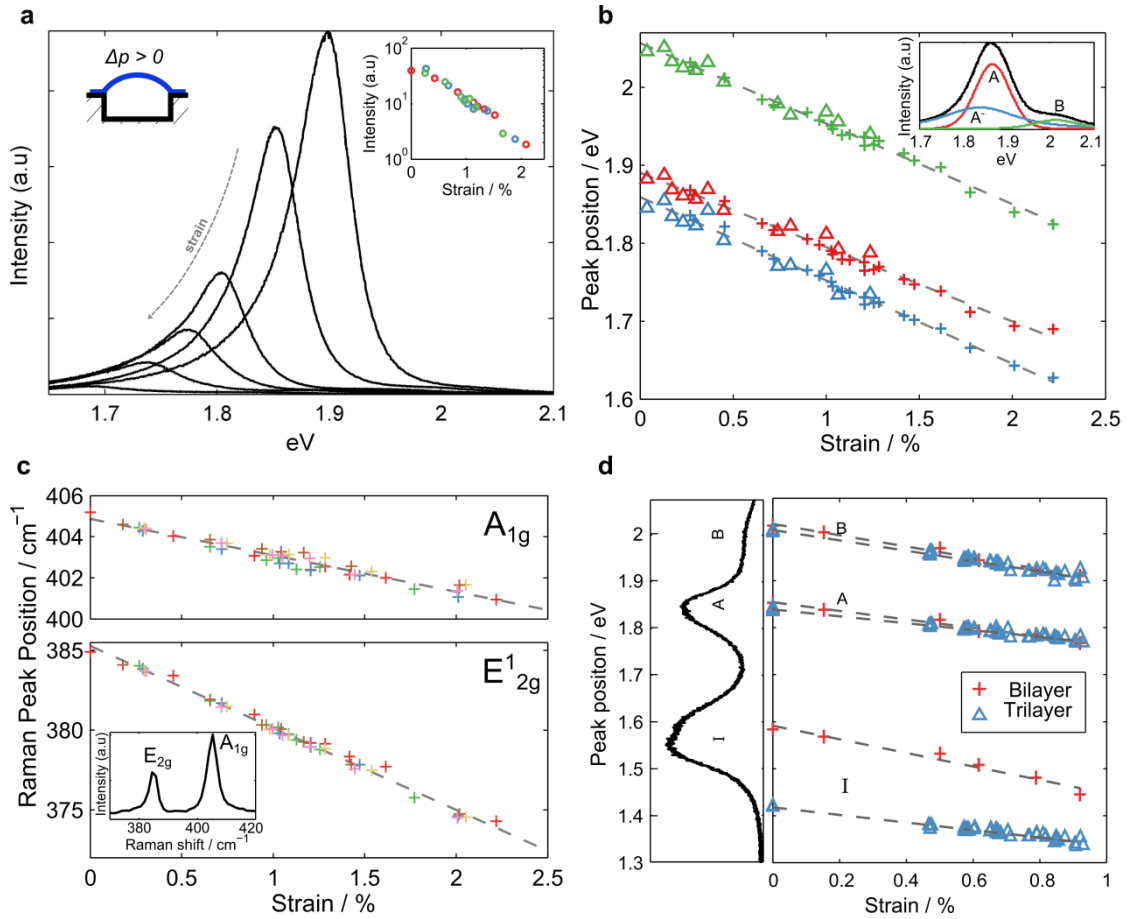


Figure 5.2 a) The PL spectra for monolayer MoS₂ at different biaxial strains corresponding to different p_{int} , and the relationship between strain and A peak intensity (inset). Intensities are normalized to the A_{1g} Raman peak. b) The peak positions of the A (red), A' (blue) and B (green) excitons as a function of biaxial strain for CVD (crosses) and exfoliated (triangles) monolayer devices. The peaks were fitted using three Voigt functions. c) The E_{2g} and A_{1g} Raman modes for unstrained MoS₂ (inset) and peak positions as a function of biaxial strain. Colors represent different devices. d) A bilayer PL spectrum, and the peak positions of the A, B and indirect I peak as a function of biaxial strain for exfoliated bilayer and trilayer devices.

Each spectrum in Fig. 5.2a contains peaks resulting from the decay of the neutrally charged A and B excitons at approximately 1.89 eV and 2.05 eV respectively (Mak et al., 2010), which form when electrons are excited across the direct band gap at the K-point and are bound to holes in the spin-split A and B valence bands. There is also

a third peak (A^-) centered at 1.86 eV (Mak et al., 2013) which results from the decay of negatively charged trions which form when additional conduction band electrons bind to A excitons. To determine how all three peaks were affected by strain, we fitted three Voigt functions to each of our PL spectra (Fig. 5.2b inset), and plotted the peak position of the A^- , A and B peaks in Fig. 5.2b. We found there was no difference in the shift rate between exfoliated and CVD grown devices, and that all three peaks had an approximately equal peak shift rate of -99 ± 6 meV / % which agrees well with theoretical predictions of 105 meV / % (Plechinger et al., 2015).

We also took a corresponding Raman spectrum at each p_{int} , so we can similarly find the shift rate of the Raman modes with strain (Fig. 5.2c). The two characteristic peaks of unstrained MoS₂, relating to in-plane (E_{2g}^1) and out-of-plane (A_{1g}) vibrations, are found at 385 cm⁻¹ and 405 cm⁻¹ respectively. By fitting a Voigt function to each mode, we found that the modes shifted linearly at a rate of -1.7 cm⁻¹/% for the A_{1g} , and -5.2 cm⁻¹/% for the E_{2g}^1 which agrees well with theoretical predictions (Scheuschner et al., 2014) and previous experiments (H. Li et al., 2015). The differences in these values to those found in hydrostatic pressure studies (Bandaru et al., 2014) (in which the A_{1g} mode has the higher shift rate) is likely due to the different type of deformation applied in the two cases. Using the formula (Zabel et al., 2012) $\gamma = [\omega - \omega_0]/[2\varepsilon\omega_0]$, we determine the Grüneisen parameters modes to be $\gamma_{E_{2g}^1} = 0.68$ which agrees well with the value of $\gamma_{E_{2g}^1} = 0.68$ and $\gamma_{A_{1g}} = 0.21$, which are also in good agreement with the values found in earlier studies (Rice et al., 2013; Y. Wang, Cong, Qiu, & Yu, 2013), The position of the A_{1g}

peak is known to vary with doping (Chakraborty et al., 2012), however as this is not the case with the more strain sensitive E_{2g}^1 mode, its peak position can be used as a reliable way to measure the internal strain of monolayer MoS₂.

Multilayer MoS₂ is also a promising material for strain based applications (Manzeli et al., 2015b), so we used the same procedure to take strain and optical measurements of one bilayer device and five trilayer devices prepared by mechanical exfoliation. For these devices we again observed the Raman mode softening for both peaks (Fig. 5.2c), but with smaller shift rates than were seen for monolayers (see Table 5.1). The PL spectrum of multilayer MoS₂ is distinguished from that of monolayers by the presence of a large additional peak resulting from indirect gap emission (Mak et al., 2010), referred to as the I peak. The peak positions for the I, A and B peaks are plotted against strain in Fig. 5.2d. We determined the A peak shift rate to be -91 meV/% for bilayers and -73meV/% for trilayers. The indirect I peak shifted considerably faster than the direct peaks in both bilayers and trilayers, at a rate of -144 meV / % and -110 meV/% respectively.

Thickness	E_{2g}^1 mode shift rate ($\text{cm}^{-1} / \%$)	A_{1g} mode shift rate ($\text{cm}^{-1} / \%$)
<i>Monolayer</i>	-5.2	-1.7
<i>Bilayer</i>	-4.2	-1.3
<i>Trilayer</i>	-3.0	-0.7

Table 5.1 Raman mode shift rates for each membrane thickness. A comparison of the strain dependencies of the Raman modes that we observed in Fig. 5.2c. These results show that both modes are less strain sensitive with increasing membrane thickness, an effect which was also observed in Rice et al., 2013.

The strain field we apply across our membranes is inhomogeneous (see chapter 3, Fig. 3.1b), which should produce a spatially varying band structure across our devices. To confirm this, we took a PL map of a strained device and plotted the peak position of the A peak at each pixel in Fig. 5.3a. We also plot line cuts through the center of the device along the axial and diagonal directions (Fig. 5.3b). The band gap is redshifted to ~ 1.7 eV at the center of the device where the membrane is subject to a pure biaxial strain. Around the edge of the device the strain becomes approximately uniaxial along the radial direction, which results in a lower band gap shift due to the smaller uniaxial band gap tuning rate in MoS₂. These results demonstrate that our device geometry produces an energy gradient which could allow excitons produced around the edge of the device to be funneled towards the lower energy region at the center of the device (Ji Feng et al., 2012; Harats, Kirchhof, Qiao, Greben, & Bolotin, 2020).

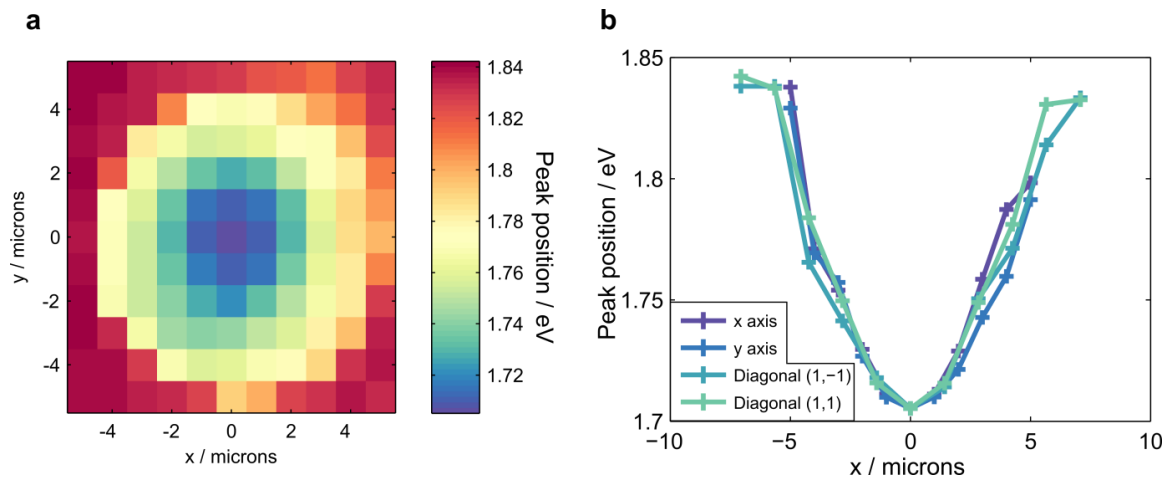


Figure 5.3 a) A PL map of a device with $p_{int} \sim 0.75$ MPa and $p_{ext} = 1$ atm, with colors representing the A peak position. **b)** Line cuts through the center of the device along the x, y, (1,1) and (1,-1) directions.

5.4 Applying Ultra-large Strains

To overcome the limitation in the magnitude of the applied strain imposed by delamination when $\Delta p > 0$, we can instead increase p_{ext} of the devices which deflects the membrane downwards. To do this, the devices were placed in a custom-built pressure chamber with a sapphire window which allows optical measurements to be taken at various p_{ext} (Kitt et al., 2013). The internal pressures of the cavities were $p_{int} = 0$, as the devices had been left to equilibrate in a vacuum chamber for several days prior to measurements. By pressurizing the chamber with N_2 gas, the greater $-\Delta p$ across the membrane deflects it further downwards and produces an increased biaxial strain at the center of the device.

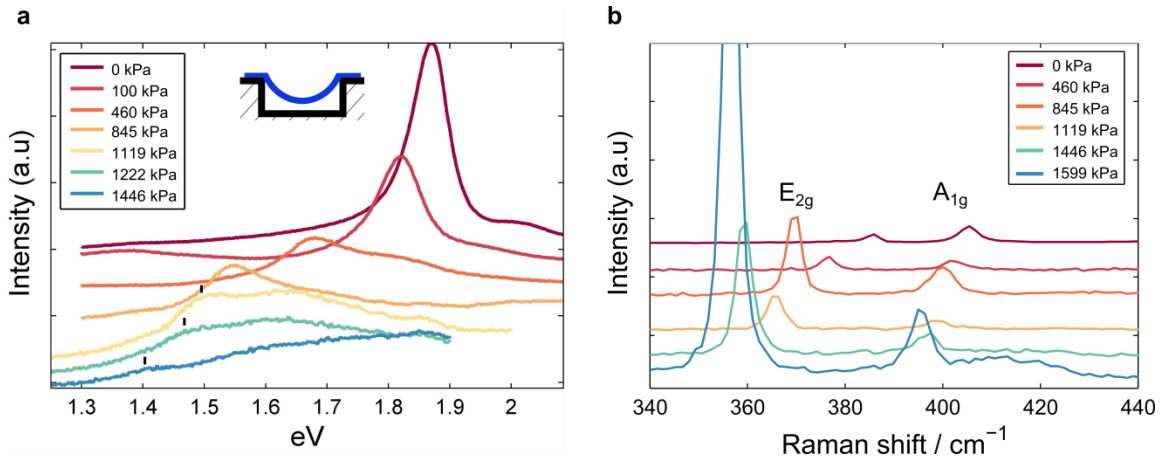


Figure 5.4 *In-situ* measurements of a) PL spectra for a monolayer device (scaled for comparison with ticks marking A peak position), with the largest pressure difference representing $\sim 5\%$ strain. b) Raman spectra at increasing chamber pressures. Labels refer to the negative pressure difference $-\Delta p$ across the membrane, and Raman peaks are normalized to the silicon peak intensity.

Fig. 5.4a shows the PL spectrum as Δp is varied from 0 to -1.45 MPa. As before, the A peak redshifts with increasing strain, and also rapidly decreases in intensity. The A peak intensity decreased faster than the B peak, so at the largest strains the peaks were of a comparable intensity. At high strains, very long exposure times are required to perceive these features above the background noise. As determined from the energy shift of the A peak, we find that we can shift the band gap in this manner by as much as 500 meV.

At each p_{ext} a Raman spectrum was also taken along with its corresponding PL spectrum. The data is normalized to the silicon peak and plotted in Fig. 5.4b. We saw the softening of both modes with increasing strain as before, and also observed the strain tuning of the second order 2LA(M) mode (H.-L. Liu et al., 2015) (Fig. 5.5b). Due to the changing deflection of the bulge with pressure, the optical interference between light scattered off the membrane and light reflected off the silicon substrate is altered, which produces the oscillatory behavior in both the peak intensities with increasing pressure (see appendix A3). As strains are increased, we observe a dramatic increase in the intensity of the E_{2g}^1 mode relative to A_{1g} mode (Fig. 5.5a), which is an effect not reported in other studies.

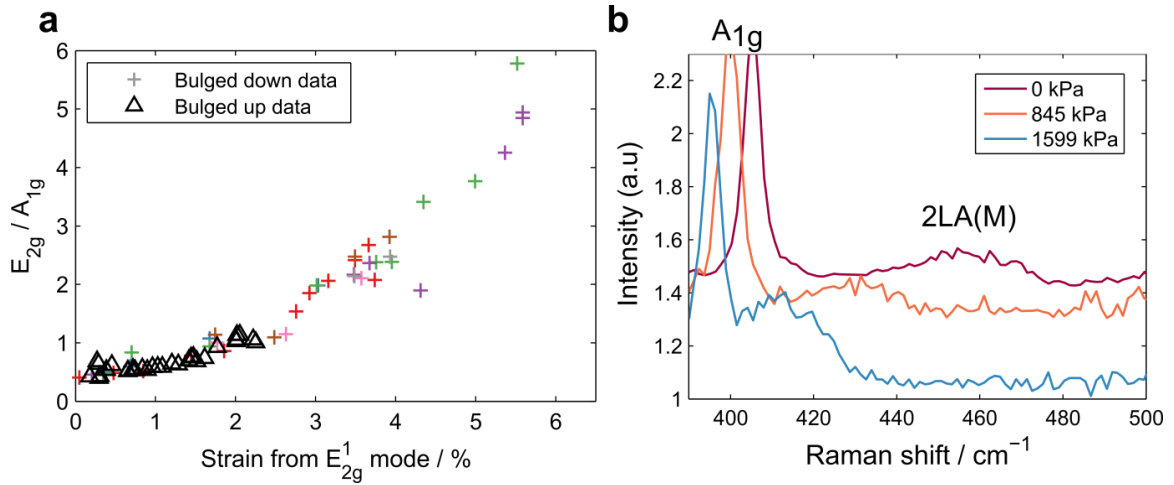


Figure 5.5 a) The Raman intensity ratio E_{2g}^1 / A_{1g} for bulged up (black triangles) and bulged down (colored crosses) devices. b) A zoomed in version of Fig. 5.4b to highlight the 2LA(M) mode.

Finally, by assuming the linear relationship we found earlier between the E_{2g}^1 Raman mode and biaxial strain holds at the higher strains we are now considering, we use the position of the strain sensitive E_{2g}^1 peak to determine the biaxial strain that was produced at each p_{ext} in Fig. 5.4, and we can therefore determine the strain in our devices by optical measurements only.

The A peak position is plotted against this strain in Fig. 5.6a, showing that biaxial strains as high as 5.6% can be achieved before membrane rupture. The relationship between the band gap shift and strain remains approximately linear at these high strains with a shift rate of 92 ± 6 meV/%, which is consistent with our earlier findings of 99 ± 6 meV/%.

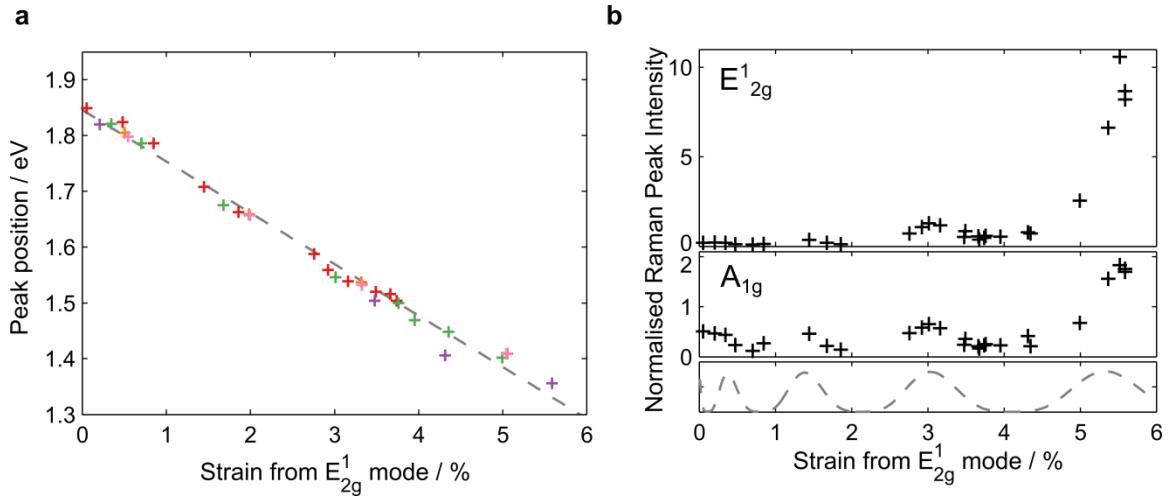


Figure 5.6 a) The A peak position of the PL spectrum plotted against the strain as determined from the E_{2g}^1 peak shift. In this case we fitted a single curve to the A peak feature, as the large decrease in PL intensity meant that the individual A and A^- peak contribution could not be resolved. Different colors represent different devices. **b)** The ratio of the integrated intensities of the E_{2g}^1 and A_{1g} modes normalized to the silicon peak and plotted against strain. The expected intensity modulation due to interference is also plotted for comparison.

We also plot the integrated intensities of both peaks (normalized to the silicon peak) against the strain as determined by the E_{2g}^1 peak position (Fig. 5.6b). At the highest strains, there was a three-fold enhancement of the A_{1g} peak, and more than a twenty-fold enhancement of the E_{2g}^1 peak. By using the Fresnel equations to model the effects of optical interference on our measurements due to the changing δ with pressure (Fig. 5.6b bottom panel and appendix A3), we find that interference effects cannot explain these enhancements, nor the relative enhancement of E_{2g}^1 over A_{1g} . We also rule out the changing curvature of our devices when strained as the source of this intensity increase (appendix A4).

Similar enhancements of the Raman peak intensities have been observed when laser excitation energies are resonant with an electronic transition (Carvalho, Malard, Alves, Fantini, & Pimenta, 2015, 2016; H.-L. Liu et al., 2015). Here, we maintain a constant laser energy of 2.33 eV, however as biaxial strain induces large changes to the electronic band structure, some transition energies may be moved closer to resonance with the laser excitation energy. We therefore attribute the increase in intensity of both peaks relative to the silicon peak, and the enhancement of E_{12g}^1 / A_{1g} , to resonant Raman scattering resulting from the strain tuning of a higher level energy transition to be in resonance with the laser. A likely candidate for this transition is the C exciton at ~ 2.8 eV (Carvalho et al., 2015, 2016; Yiling Yu et al., 2015), since the redshift required to lower its energy to resonance with our laser would be ~ 500 meV, a value consistent with the shift of the A peak at our highest strains. These results demonstrate not only that CVD grown monolayer MoS_2 films can withstand the remarkably high strains of 5.6% over micron sized areas, but that higher level optical transitions may also be tuned with strain.

5.5 Conclusions

The ability to continuously and reversibly modulate the optical band gap of monolayer MoS_2 by up to 25% allows significant control over the optical and electrical properties of the material, an effect which could be used to produce sensitive piezoresistive pressure sensors or broadband light absorbers. We also grew atomically thin membranes by CVD which are highly impermeable to gases and can withstand large

pressure differences across them, suggesting that CVD grown MoS₂ could be promising as a gas separation membrane. The method used in this work may be extended to study the effects of biaxial strain on other 2D semiconducting materials, and could also be used to determine the effects of very high strains on other strain dependent phenomena, such as magnetism (Manchanda, Sellmyer, & Skomski, 2015), chemical adsorption (Kou, Du, Chen, & Frauenheim, 2014) or piezoelectricity (W. Wu et al., 2014).

CHAPTER SIX: ADHESION, STIFFNESS, AND INSTABILITY IN ATOMICALLY THIN MoS₂ BUBBLES

In this chapter we measure the work of separation of single and few-layer MoS₂ membranes from a SiO_x substrate using a mechanical blister test, and found a value of 220 ± 35 mJ/m². Our measurements were also used to determine the 2D Young's modulus (E_{2D}) of a single MoS₂ layer to be 160 ± 40 N/m. We then studied the delamination mechanics of pressurized MoS₂ bubbles, demonstrating both stable and unstable transitions between the bubbles' laminated and delaminated states as the bubbles were inflated. When they were deflated, we observed edge pinning and a snap-in transition which are not accounted for by the previously reported models. We attribute this result to adhesion hysteresis and use our results to estimate the work of adhesion of our membranes to be 42 ± 20 mJ/m².

6.1 Introduction

Adhesive forces play an important role in shaping the mechanical behavior of atomically thin materials such as graphene or molybdenum disulfide, MoS₂. These forces keep the material clamped to the substrate, and also influence how the membrane folds (Cranford, Sen, & Buehler, 2009), slides (Suzhi Li et al., 2016), and peels (Annett & Graham, 2016). An understanding of adhesion in these materials is important in the fabrication of nanoelectromechanical systems (Bunch et al., 2007), flexible electronic

devices (Akinwande, Petrone, & Hone, 2014), graphene origami (Cranford et al., 2009; Ebbesen & Hiura, 1995), graphene separation membranes (Koenig et al., 2012), and stacked heterostructures formed from 2D materials. Atomically thin crystals may also provide a fruitful system in which to study novel features of friction and adhesion present only at the nanoscale (Carpick & Salmeron, 1997; Koren, Lörtscher, Rawlings, Knoll, & Duerig, 2015; C. Lee, Li, et al., 2010; Suzhi Li et al., 2016). In terms of device performance, adhesive forces determine the maximum strain 2D materials can support which is important in designing stretchable electronic devices (W. Wu et al., 2014) and pressure sensors (Smith et al., 2016).

The study of bubbles formed by atomically thin sheets has proven to be useful for discovering the adhesive and mechanical properties of these materials, and has allowed measurements of the adhesion energies (Koenig et al., 2011), friction coefficient (Kitt et al., 2013), and Young's modulus of graphene and other 2D materials (Khestanova, Fumagalli, Geim, & Grigorieva, 2016). In particular, Koenig et al. used a mechanical blister test to measure the adhesion energy between graphene and SiO_x of $\sim 450 \text{ mJ/m}^2$. Like graphene, atomically thin MoS_2 is a mechanically exceptional material (Cooper et al., 2013), whilst also being piezoelectric (W. Wu et al., 2014; H. Zhu et al., 2014) and a direct gap semiconductor with a highly strain sensitive band gap (Castellanos-Gomez et al., 2013; Conley et al., 2013b; He et al., 2013; Lloyd et al., 2016). A good understanding of the mechanical stiffness and adhesion to the substrate is therefore of particular

importance to this material which has applications involving the interplay between adhesive and tensile forces.

6.2 Device geometry

In this paper, we measure the work of separation (sometimes referred to as the adhesion energy) between MoS₂ and the substrate by employing the same geometry as used in our previous work (Bunch et al., 2008; Koenig et al., 2011, 2012), in which we suspend mechanically exfoliated or chemical vapor deposition (CVD) grown membranes over cylindrical microcavities etched into a silicon oxide (SiO_x) substrate (Fig. 6.1a and 1b). The devices are then placed in a pressure chamber filled with a gas of pressure p_0 , which gradually leaks into the cavities through the SiO_x substrate until the internal pressure p_{int} reaches that of the chamber ($p_{int} = p_0$). We used either N₂, Ar, H₂ or He gas which allowed us to choose a convenient leak rate of the gas into the microcavities. When the devices are removed from the pressure chamber the internal pressure (p_{int}) is greater than the external pressure ($p_{ext} = 1$ atm), and this pressure difference ($\Delta p = p_{int} - p_{ext} > 0$) causes the membrane to bulge up (Fig. 6.1c and d). For each charging pressure p_0 we measure the deflection δ and radius a of the bubble using an atomic force microscope (AFM) after which the devices are returned to the pressure chamber at a higher p_0 and the process is repeated. We fabricated devices of 1-3 layer thickness by mechanical exfoliation, and made monolayer devices from CVD grown MoS₂ using a PMMA transfer method (see chapter 4 for details). We transferred 6 different growths to produce

CVD samples *NI-6*, with each containing many individual devices. The SiO_x substrates were O_2 plasma cleaned prior to transfer.

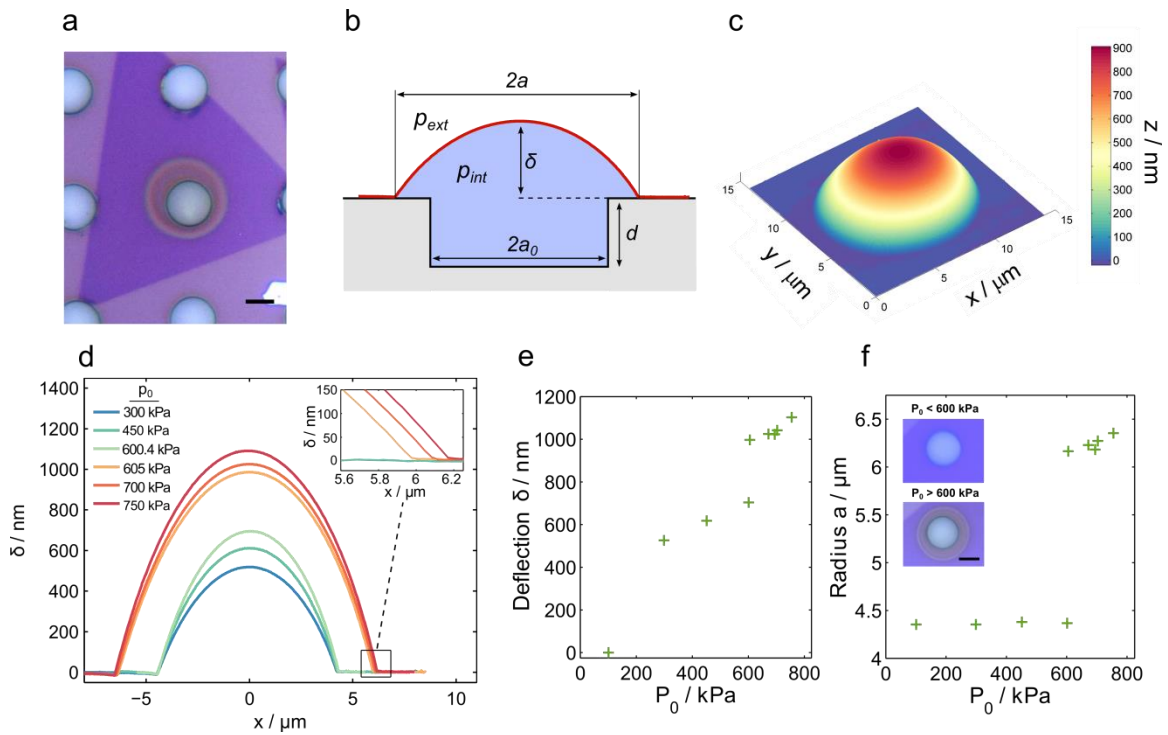


Figure 6.1 a) Microscope image of a delaminated device (scale bar is $5\mu\text{m}$). b) Device schematic. c) AFM image and d) AFM cross sections. e) Deflection δ and f) radius a plotted against input pressure p_0 . Inset microscope images show a device before and after snap-out (scale bar is $5\mu\text{m}$).

As can be seen in Fig. 6.1d-f, increasing p_0 causes δ to increase with a initially remaining pinned at the radius of the cylindrical microcavity, a_0 . After a critical pressure is reached ($p_0 \sim 600$ kPa), the force from the pressure difference across the membrane overcomes the adhesive forces keeping the membrane clamped to the substrate, and delamination occurs in the form of a snap-out transition of the radius from $4.4\mu\text{m}$ to 6

μm . After the snap-out transition, both a and δ continue to gradually increase as p_0 is increased.

6.3 Finding the Young's modulus and the work of separation

We begin by using our values for p_0 , δ and a to determine the Young's modulus of MoS_2 with a formula developed in Hencky's model for clamped pressurized membranes (Fichter, 1997), which relates the pressure difference across the membrane Δp to the deflection δ and radius a by the formula,

$$\Delta p = \frac{K(\nu)E_{2D}\delta^3}{a^4} \quad (\text{Eq. 6.1})$$

with a Poisson's ratio $\nu = 0.29$ (Cooper et al., 2013), numerical constant $K(\nu) = 3.54$ and a two dimensional Young's modulus E_{2D} equal to the bulk Young's modulus multiplied by the thickness of the material. The pressure difference, Δp , is calculated from p_0 by assuming isothermal expansion of a fixed number of ideal gas molecules from the initial volume of the cavity (V_0) to its final volume ($V_0 + V_b$), such that $p_0V_0 = p_{int}(V_0+V_b)$. From Hencky's model, the volume created beneath the bubble can be found from the device geometry using the expression $V_b = C(\nu)\pi a^2\delta$, and a numerical constant $C(\nu) = 0.522$. We neglect the effect of the membrane pre-tension (see appendix B1 for details).

We measured the E_{2D} of 3 CVD samples (NI-3), and of exfoliated monolayer and

trilayer flakes containing 2 and 16 devices respectively. Fig. 6.2a shows a plot of Δp against $K(v) \delta^3/a^4$ for each of our CVD monolayer and bilayer devices in sample N2, including linear fits which are used to determine E_{2D} for each device. The E_{2D} of each device in these samples is plotted in Fig. 6.2b. In Fig. 6.2c we plot the mean E_{2D} for each sample divided by the number of layers n in the membranes in order to compare estimates for the E_{2D} of a single MoS₂ layer. Error bars represent the standard deviation.

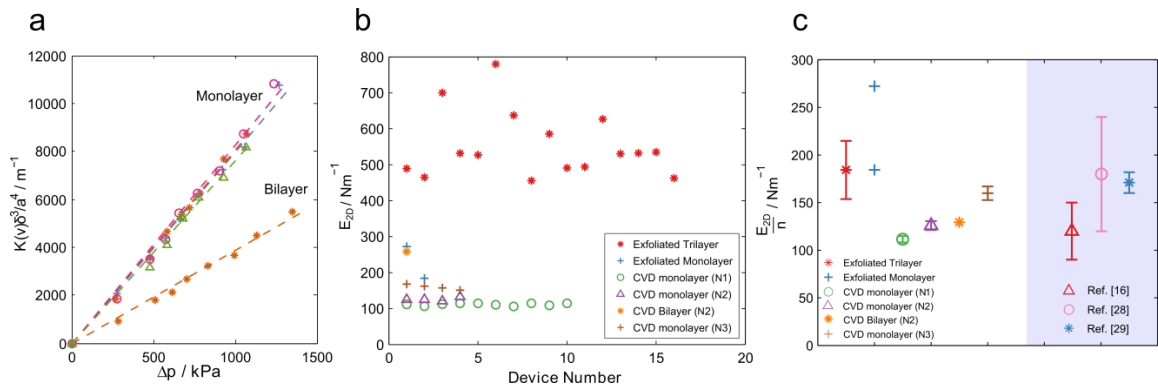


Figure 6.2 a) Plots for CVD monolayer and bilayer devices (different symbols/colors represent each device), with linear fits (dashed lines) used to find E_{2D} . b) E_{2D} for each device in our exfoliated samples, and three of our CVD samples (N1-3) c) E_{2D} divided by number of layers n for each sample. Data points and error bars represent the mean and standard deviation respectively for each sample. Results from nanoindentation measurements in references 16, 28 and 29 are plotted for comparison.

For our exfoliated devices we find an average E_{2D} per layer of 190 ± 35 N/m, and for our CVD grown MoS₂ monolayers we find an average E_{2D} of 128 ± 20 N/m. There is a low variance of E_{2D} within each CVD grown sample, however there is a significant difference between the average E_{2D} for each CVD sample. The discrepancy between CVD and exfoliated samples and among different CVD samples may be due to

differences in defect densities (López-Polín et al., 2015; Zandiatashbar et al., 2014) which occur during CVD growth, as an increased sulfur vacancy density (Hong et al., 2015) is predicted to lower E_{2D} in MoS₂ (Gan & Zhao, 2014). The average of all our exfoliated and CVD grown samples is 160 ± 40 N/m, which falls within the same range of values as found in previous studies (Bertolazzi et al., 2011; Cooper et al., 2013; K. Liu et al., 2014), which we plot in Fig. 6.2c for comparison.

We next determined the work of separation, Γ_{sep} , using our values for p_0 , δ and a , and a free energy model described in detail by others (Boddeti et al., 2016; Wan & Mai, 1995). Briefly, we can write the total free energy of the system F as,

$$F = \frac{(p_{int}-p_{ext})V_b}{4} + \Gamma\pi(a^2 - a_0^2) - p_0V_0 \ln \left[\frac{V_0+V_b}{V_0} \right] + p_{ext}V_b \quad (\text{Eq. 6.2})$$

where V_0 is the initial volume of the cavity, V_b is the additional volume created as the bubble expands. Γ is the adhesion energy, which is equal to Γ_{sep} in the case of delamination. The first two terms represent the elastic strain energy and the work to separate the membrane from the substrate respectively, and the final two terms account for the isothermal expansion of the gas.

When a device is removed from the pressure chamber, the bubble volume expands until the free energy of the system F reaches a local minimum. We minimize F with respect to a by setting $dF/da = 0$ and using the relationship $p_0V_0 = p_{int}(V_0 + V_b)$.

This yields the expression for the work of separation:

$$\Gamma_{sep} = \frac{5C}{4} \left(\frac{p_0 V_0}{V_0 + V_b(\delta, a)} - p_{ext} \right) \delta \quad (\text{Eq. 6.3})$$

with the constant $C(\nu) = 0.522$ for $\nu = 0.29$ (Cooper et al., 2013). Using this expression, we can determine Γ_{sep} of each device using the charging pressure of the pressure chamber p_0 , and δ and a of the bubble measured using an AFM. We can also substitute the pressure terms in Eq. 6.3 with Hencky's result in Eq. 6.1 which yields,

$$\Gamma_{sep} = \frac{5}{4} C K E_{2D} \left(\frac{\delta}{a} \right)^4 \quad (\text{Eq. 6.4})$$

which holds for all devices which have started to delaminate ($a > a_0$). This allows Γ_{sep} to be determined from δ and a without knowing p_0 , which avoids the long waiting times required for devices to reach equilibrium in the pressure chamber. For our exfoliated devices we calculated Γ_{sep} using Eq. 6.4 (using the mean value of $E_{2D} = 190$ N/m per layer we found earlier for exfoliated samples), and used Eq. 6.3 to calculate Γ_{sep} for our CVD devices where p_0 was well known.

We find no significant difference in Γ_{sep} between single and few layer samples, or CVD and exfoliated samples (Fig. 6.3). By averaging over all samples we find the mean work of separation to be $\Gamma_{sep} = 220 \pm 35$ mJ/m², which is close to the value of 170 ± 30

mJ/m² measured for many layer MoS₂ (Deng, Gao, Xu, & Berry, 2017) and is in the same range of values as found for graphene (Akinwande et al., 2017; Cao et al., 2013; Koenig et al., 2011; Suk et al., 2016; Zong, Chen, Dokmeci, & Wan, 2010).

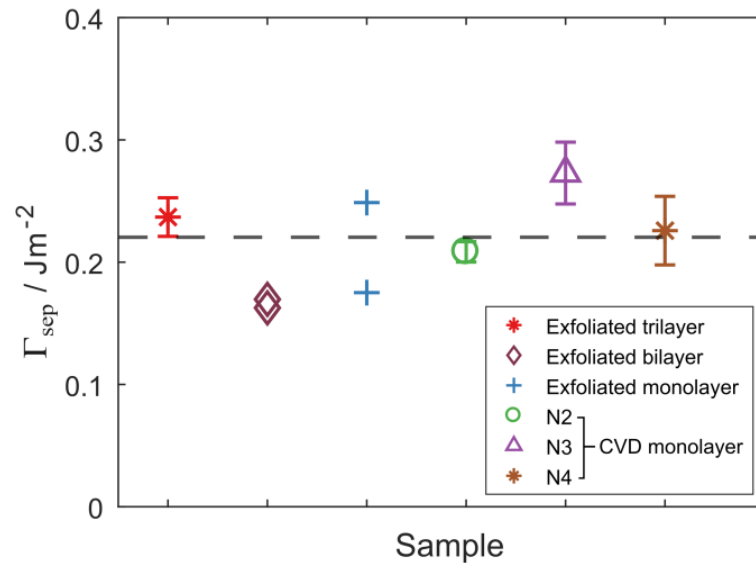


Figure 6.3 Work of separation of membranes of 1 to 3 layer thickness. The data includes measurements of CVD monolayer devices from three separate growths and transfers (N2-4). Several devices are measured per sample, with data points and error bars representing the means and standard deviations respectively. For samples with fewer than 3 measurements the data points represent each device measured. The dashed line marks the mean of the 6 samples.

The devices shown in Fig. 6.1d-f exhibit unstable delamination, whereby a discontinuously increases from the initial radius a_0 when $p_0 \gtrsim 600$ kPa. The etched depth of the microcavities in that case was $d = 1500$ nm. We also fabricated devices with cavity depths of $d = 650$ nm, and again performed measurements of δ and a at increasing p_0 (Fig. 6.4) using the method described earlier. With this cavity depth, the devices show no snap-out transition, and rather stably delaminate with a continuously increasing from a_0 .

The difference in behavior in these two cases has been observed and modeled by others (Boddeti et al., 2016; P. Wang, Liechti, & Huang, 2016), and Boddeti et al. found that the transition from unstable to stable delamination occurs when the parameter $S = 2V_b/V_0$ satisfies the condition $S > 1$ just before the point of delamination (Boddeti et al., 2016). Reducing the well depth decreases the volume of the cavity relative to the volume of the bubble which increases S . By making various device geometries and finding S from AFM measurements we confirmed empirically that this transition occurs in the range $0.74 < S < 1.11$, and we obtained the same value for Γ_{sep} for both stable and unstable delamination.

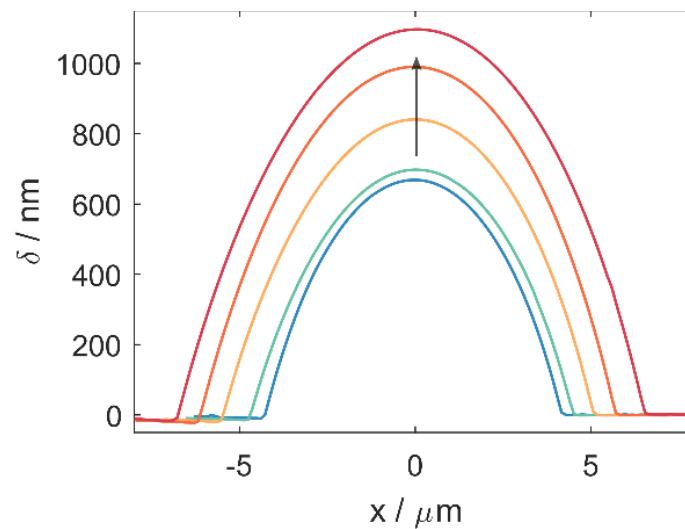


Figure 6.4 Stable delamination with increasing pressure.

6.4 Adhesion hysteresis and finding the work of adhesion

After the devices with $d = 1500$ nm (on sample $N2$) had been delaminated to their largest radii, they were left out in ambient conditions to deflate over the course of ~ 48 hours. During this time AFM scans captured δ and a as the number of gas molecules N decreases from the initial value of $N_0 (= p_0 V_0 / k_b T)$. AFM cross sections of a bubble are shown in Fig. 6.5a during the inflation (increasing N_0) and deflation (decreasing N) of the device. Initially as the device is inflated, δ increases and a remains pinned at a_0 . When $p_0 \gtrsim 600$ kPa the snap-out transition occurs and a jumps to a larger value, after which both a and δ increase together as N_0 increases. When devices are left to deflate, δ decreases from an initial value of δ_0 , however a now does not change from its radius at the beginning of deflation, which we refer to as the ‘pinned radius’ a_p . After the deflection of the devices reaches a critical value $\delta = \delta_c$ the devices undergo a snap-in transition where the radius jumps from a_p to a_0 , and δ continues to decrease to zero. Values for δ and a throughout this process are shown in Fig. 6.5b, which shows devices deflating at a number of different a_p . To rule out any influence of tip-sample forces from the AFM affecting the measurements of deflating devices, we used both photoluminescence spectroscopy (see appendix B7 for details) and a high speed camera to observe the same snap-in behavior in the absence of an AFM tip. The high speed camera footage^{††} shows the snap-in transitions occur in less than $500 \mu\text{s}$.

^{††} Videos of the snap-out and snap-in transitions can be found online in the paper’s supporting information at <https://pubs.acs.org/doi/abs/10.1021/acs.nanolett.7b01735>

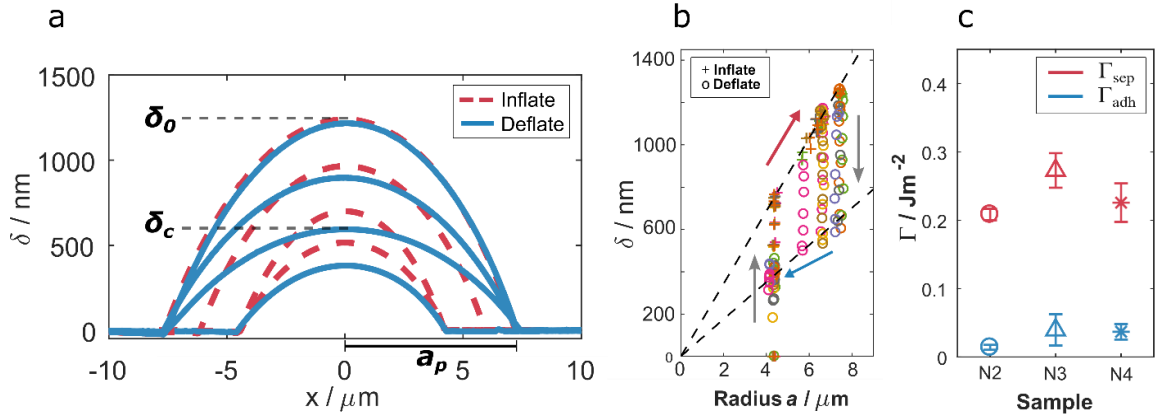


Figure 6.5 a) AFM cross sections of a device during inflation (increasing N) and deflation (decreasing N). Arrows mark the snap transitions. b) δ and a of devices during inflation and deflation. Different colors represent different devices on sample N2. More data can be found in the supplementary information which is not shown here for reasons of clarity. Red and blue arrows mark snap-out and snap-ins respectively. The upper and lower dashed lines correspond to solutions to Eq. 6.4 and Eq. 6.7 respectively. c) A comparison between the works of separation and adhesion for samples N2-4. Data points and error bars represent the means and standard deviations respectively of all the devices measured on each sample.

We can interpret this using the result derived in Eq. 6.4, which requires that after delamination the ratio δ/a remains constant, with the magnitude of this ratio being proportional to $\Gamma_{\text{sep}}^{1/4}$. We plot the line corresponding to this formula in Fig. 6.5b (upper dashed line) with the values of E_{2D} and Γ_{sep} determined earlier, and find our data for increasing N_0 follows this trend very well.

This formula is independent of whether N is increasing or decreasing, so when our devices are left to deflate we should expect δ and a to return along the same path as during inflation described by Eq. 6.4. As can be seen in Fig. 6.5a however, there is a significant difference in the geometry of the bubbles during inflation and deflation, which

suggests some element of our system is irreversible.

We attribute the difference between inflation and deflation we see in our data to the widely observed phenomenon of *adhesion hysteresis* (J. N. Israelachvili, 2011; Shull, 2002; Suk et al., 2016), whereby the energy required to separate the membrane from the surface Γ_{sep} is greater than the energy returned to the system as the membrane re-adheres Γ_{adh} , with $\Gamma_{adh} < \Gamma_{sep}$. We can summarize these criteria as

$$\Gamma = \begin{cases} \Gamma_{adh}, & \Delta a < 0 \\ \Gamma_{sep}, & \Delta a > 0 \end{cases} \quad \& \quad \Gamma_{adh} < \Gamma_{sep} \quad (\text{Eq. 6.5})$$

where Δa is the change in the device radius.

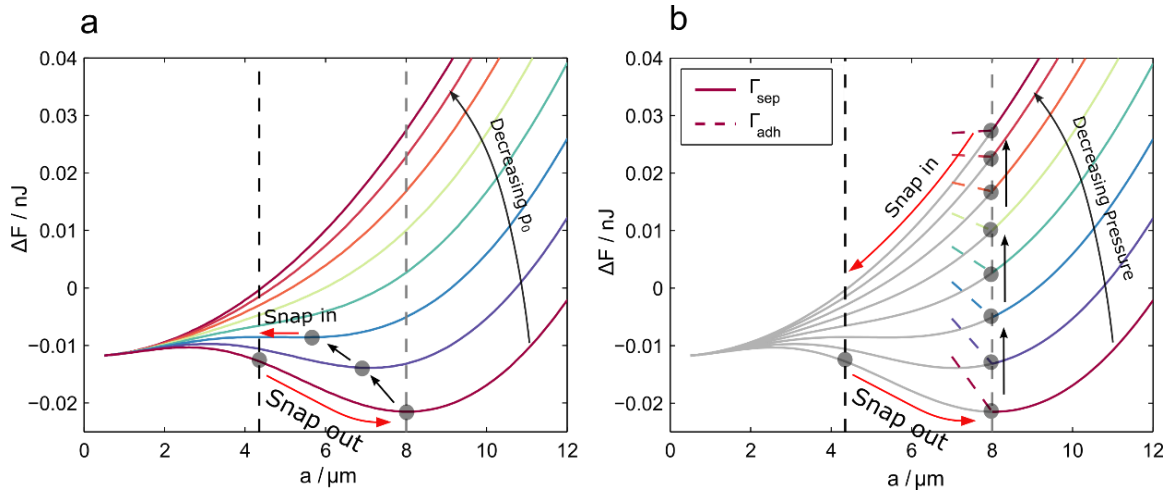


Figure 6.6 a) The free energy landscape for a device with no adhesion hysteresis. The device radius adjusts to minimize the free energy, and the energy minima are marked with grey circles. b) The energy landscape if the criteria in Eq. 6.5 are followed. The dashed and solid lines are generated using Eq. 6.2 with $\Gamma = \Gamma_{adh}$ and $\Gamma = \Gamma_{sep}$ respectively.

The effects of this on our model are most easily understood by plotting the free energy landscape given by Eq. 6.2. We first plot the free energy $F(a)$ as a function of radius a for the case of *no* adhesion hysteresis (Fig. 6.6a). The free energy minima gradually decrease in radius as the pressure p_0 decreases, until the energy minimum disappears. At this point the gradient of the curve means that the lowest free energy is achieved if the device undergoes a snap-in transition. This is not what we see in our experiments, where we find the radius remains pinned at the initial snap-out radius (Fig. 6.5a). If there is adhesion hysteresis however, the fact that $\Gamma_{adh} < \Gamma_{sep}$ means that reducing the radius a is a less effective means of reducing $F(a)$. This, combined with the asymmetry produced by the criteria in Eq. 6.5 means that a new free energy minimum is created (Fig. 6.6b). The dashed and solid lines are produced from Eq. 6.2 with $\Gamma = \Gamma_{adh}$ and $\Gamma = \Gamma_{sep}$ respectively. The radius a becomes stuck in this energy well where it remains pinned at the initial snap-out radius a_p , until a critical pressure (or critical deflection δ_c) where the device undergoes a snap-in transition. The critical pressure for snap-in occurs when δ has reduced enough for the gradient of $F(a)$ to become positive for $\Delta a < 0$, which allows the free energy to be minimized by the reduction in a , which can be described mathematically as

$$\frac{dF}{da} = 2\pi a_p \left[\Gamma_{adh} - \frac{5}{4} CKE_{2D} \left(\frac{\delta}{a_p} \right)^4 \right] > 0 \quad (\text{Eq. 6.6})$$

The point of the snap-in transition therefore occurs when a relationship between the critical deflection δ_c , a_p and Γ_{adh} , is satisfied,

$$\Gamma_{adh} = \frac{5}{4}CKE_{2D} \left(\frac{\delta_c}{a_p} \right)^4 \quad (\text{Eq. 6.7})$$

We perform a linear fit of our measurements of δ_c and a_p (lower dashed line in Fig. 6.5b) which yields an estimate of the work of adhesion for this sample to be $\Gamma_{adh} = 14 \pm 5$ mJ/m². Multiple measurements of Γ_{adh} with the same device show that this measurement is repeatable over many cycles (Fig 6.7a). We performed measurements on a total of 5 CVD grown samples (N2-6) and found the mean work of adhesion for all our samples to be 42 ± 20 mJ/m², with $\Gamma_{adh} < \Gamma_{sep}$ in every device. Γ_{adh} varied noticeably between samples with sample means falling in the range 14 - 63 mJ/m² (Fig. 6.7b). This large sample-to-sample variation suggests that factors such as the cleanliness of substrate or membrane may play significant roles in adhesion hysteresis.

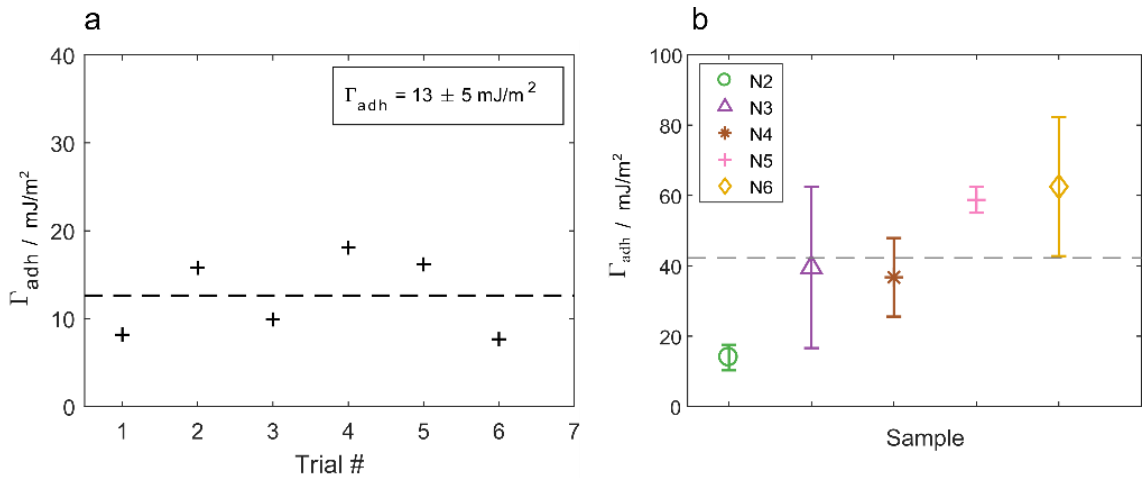


Figure 6.7 a) We checked the repeatability of our measurements of Γ_{adh} by repeating the experiment 6 times on a single device at a number of different charging pressures, which resulted in a mean and standard deviation of 13 mJ/m² and 5 mJ/m² respectively. **b)** Mean and standard deviations of the work of adhesion in each sample. The dashed line represents the mean of the 5 samples.

We directly compare the works of separation and adhesion for 3 of our samples (*N2-4*) in Fig. 6.5c. Our measurements of Γ_{adh} show that as little as one tenth of the energy required to separate the membrane from the substrate ($\Gamma_{sep} \sim 220 \text{ mJ/m}^2$) is recovered as the membrane at the edge of the bubble re-adheres to the substrate. We used Raman spectroscopy to measure the membrane strain distribution around our devices before and after snap-in (see appendix B4), and found that whilst some energy was dissipated in the form of residual strain transferred to the membrane, this can only account for <10% of the dissipation that produces a difference between Γ_{adh} and Γ_{sep} . This strain may also dissipate some energy through frictional sliding as the membrane changes its length on the surface of the substrate (Kitt et al., 2013).

Adhesion hysteresis is a commonly observed phenomenon (Chen, Helm, & Israelachvili, 1991) which has previously been observed in nano-indentation measurements of graphene (Suk et al., 2016), and the fraction of the energy dissipated in our system is comparable with the hysteresis observed in elastomers (Yalin Yu, Sanchez, & Lu, 2015). The behavior of our devices is also analogous to the related phenomenon of contact angle hysteresis seen in liquid bubbles (J. N. Israelachvili, 2011), and constant contact area pinning during unloading has been seen previously between two adhered solid spheres (Maugis & Barquins, 1978). Surface roughness and chemical heterogeneity on the surface can produce contact angle and adhesion hysteresis (Chen et al., 1991; de Gennes, 1985), and a further contribution in our system could be the finite time over which deflation occurs. This could mean that the membrane does not have time during

the measurement to re-conform fully to the surface or re-make the bonds which were made before the device delaminated (Kim, Choi, Ulman, & Fleischer, 1997; Tian et al., 2017). This would result in the system being in a transient non-equilibrium state during the measurement, which is a common cause of thermodynamic irreversibility and adhesion hysteresis (Chen et al., 1991; J. Israelachvili & Berman, 1995; Qian & Yu, 2013). Our method of finding Γ_{sep} also involves subjecting the membranes to high external pressures prior to measurement, which could improve their conformation to the substrate and thereby enhance Γ_{sep} relative to Γ_{adh} .

6.5 Conclusions

We have measured the work of separation of single and few layer MoS₂ fabricated by CVD and mechanical exfoliation, and found a value of $\Gamma_{sep} = 220 \pm 35$ J/m². We also measured the Young's modulus, and found that $E_{2D} = 160 \pm 40$ N/m for a single MoS₂ layer. Bulge testing provides a complimentary method to nanoindentation to determine E_{2D} , and our results are in the same range of values as reported in previous studies. We demonstrated snap-out and snap-in instabilities, which mechanically amplify small changes in pressure and could be used for pressure sensing. Finally we observed bubble edge pinning, analogous to contact angle hysteresis observed in liquids, and used Raman spectroscopy to provide evidence that the trapping of strain energy after the snap-in transition can account for some but not all of the hysteresis. We measured a Γ_{adh} which was significantly lower than Γ_{sep} , which may affect the performance of nanomechanical

switches made from atomically thin materials (X. Liu et al., 2014; Shi et al., 2012). The distinction between Γ_{adh} and Γ_{sep} we have observed here is an important consideration in the analysis of bubbles formed under atomically thin crystals (Algara-Siller et al., 2015; Dollekamp, Bampoulis, Poelsema, Zandvliet, & Kooij, 2016; Khestanova et al., 2016), and in the design of folded 3D structures made from 2D sheets (Cranford et al., 2009; Ebbesen & Hiura, 1995).

CHAPTER SEVEN: IN-SITU AFM IMAGING OF GRAPHENE NANOPORES

7.1 Introduction to nanopores

Nanopores are nanometer scale apertures which permit the passage of small molecules between two reservoirs. Nanopores are interesting because they have a diameter that is similar to the size of the molecules that pass through them. This means they can be used to separate molecules based on their size – essentially a nanoscale sieve. It is hoped that a membrane containing billions of such selective nanopores could be used as an industrial scale separation membrane, with the ability to separate based on molecular size with a sub-Ångstrom resolution. Nanoporous materials have been proposed which would be able to filter the CO₂ gas from industrial pollution (Ali et al., 2019) or separate salt ions from sea water (Cohen-Tanugi & Grossman, 2012). With enough imagination and research, nanopores may one day play a role in combating the major humanitarian issues of climate change and water scarcity. They are also examples of the smallest possible channels, and so can be used to study novel transport phenomena at a scale where macroscale formalisms break down.

Nature is the original inventor of the nanopore – your ability to read these words results from the opening and closing of billions of nanoscale ion channels which control the flow of charge across nerve cells, and allow action potentials to reverberate through the brain. In fact, biological ion channels are so fundamental to perception, movement

and metabolism that they are thought to have “...developed early in evolution, probably in the service of basic cellular tasks like energy production and osmotic stabilization of cells, and evolved to underlie the elaborate electrical system that provides rapid perception and control” (Hille, Armstrong, & MacKinnon, 1999).

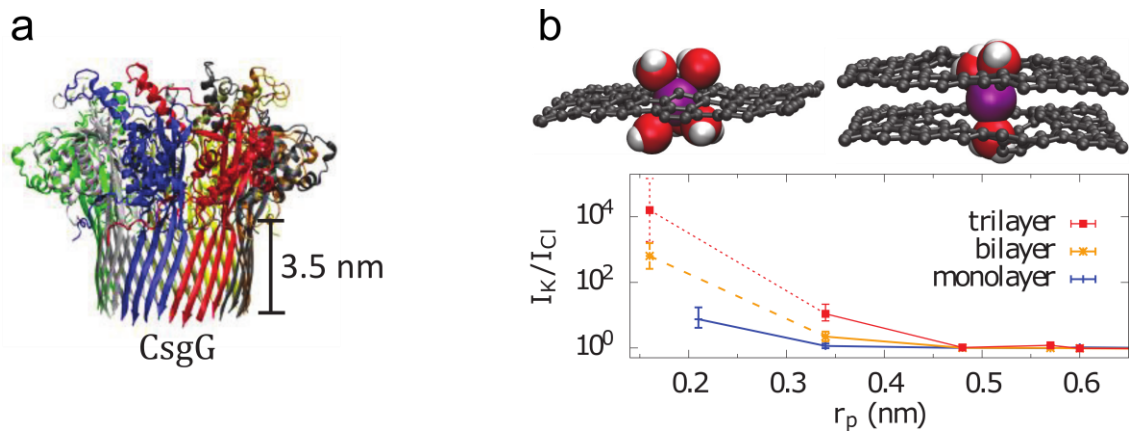


Figure 7.1 a) The membrane lipoprotein used by Oxford nanopore to sequence DNA. b) The steric exclusion of ion hydration radii means that large ion selectivity can be achieved in sub-nanometer graphene nanopores. In this case, K^+ cations have a flux across the pore that is several orders of magnitude higher the similarly sized Cl^- anions. Both images from (Sahu & Zwolak, 2019).

The nanoscale pores and membrane proteins designed by nature are so successful that engineers have sometimes transplanted them directly into their own technology, rather than make their own. The power of this approach is exemplified in the technology of Oxford Nanopore, who used the membrane lipoprotein CsgG to build a commercially available, USB plug-in desktop DNA sequencer that is capable of sequencing an entire human genome (Jain et al., 2018). They do this by measuring the conductance of the pore as DNA strands pass through it. As each base pair passes through, it modulates the

conductance of the pore by a unique magnitude and duration, allowing A,T,C and G's to be disambiguated in sequence using just a time series of the pore conductance.

Sometimes it is preferable to make synthetic nanopores from materials which lend themselves to mass production methods. The advantage of such *solid state* nanopores is that they are considerably more robust than their biological equivalents, which only evolved to function in water at a limited range of pressure, temperature and pH. Synthetic nanopores are able to withstand far more extreme environments, and could be used for chemical or gas separations in which a biological membrane protein would be unstable. To date, nanopores have been constructed from various polymers, silicon oxide, and silicon nitride (SiN_x), and various 2D crystals (Sahu & Zwolak, 2018). SiN_x is the most commonly used material due to its simple compatibility with CMOS wafer fabrication techniques.

We will study nanopores in atomically thin graphene for use as a nanoporous separation membrane. This is a promising technology on two fronts. Firstly, its ultimate thinness means the resistance that molecules face when translocating the pore is maximally small. This makes the membrane very efficient for high throughput applications like water desalination (Cohen-Tanugi & Grossman, 2012). Secondly, it is relatively straight forward to porate 2D materials with the smallest possible nanopores. Sub-nanometer pore diameters can be made by ejecting one or a handful of atoms from the 2D crystal by UVO, O_2 plasma, ion beam or electron beam irradiation. Nanopores of

< 10nm diameters have been made in bulk materials (e.g. SiN_x) using a focused ion beam (FIB) or TEM, however the process is slow and un-scalable. The advantage of using graphene is that millions of sub-nanometer pores can be created in parallel, with the aim of making high-selectivity, high-permeance membranes (Thiruraman et al., 2018). Pores which approach the Ångstrom scale of individual ions are of particular interest, as the steric exclusion of the hydration layers surrounding each ion allows for very high ion selectivity (Fig. 7.1b).

In particular, in this chapter we will study the transport of different cations across graphene nanopores. We find that nanopores of diameters as large as 50 nm show an unexpectedly high cation selectivity, with cations with the smallest hydration energy having the highest conductance. We also find that such pores can have other behaviors - such as being non-conductive, or being highly conductive but non-selective - and use liquid AFM to discover that nanoscale bubbles pinned to graphene nanopores is the source of the observed variation.

7.2 Conductance measurements of graphene nanopores

We will use an electric field to drive the ions through the pores by electrophoresis, and determine the relative permeability of each ion from measurements of its electrical conductance (Fig. 7.2a). The nanopore is immersed in an aqueous solution containing various different salts, and a voltage is applied across it using a voltage source

and two AgCl electrodes. Cations (K^+ , Na^+ , Li^+ , etc...) move with the electric field lines through the pore, and the anions (Cl^-) move the opposite direction. The net flow of charge is measured with a current pre-amp connected to a DAQ board. The current is measured as the voltage is swept over positive and negative voltages (typically $\pm 500mV$), from which we can infer the conductance for each cation species.

The graphene membrane is transferred onto a SiN_x chip containing a $1 - 5\mu m$ diameter through hole. The chip is then mounted on a PDMS flow cell that lets fluid access the back side of the chip while allowing AFM measurements to be taken on the top side. The chip is sealed with PDMS to ensure no current leakage through its sides. A droplet of salt solution can then be placed on top of the chip, and also injected to the back side. Electrodes are immersed in solution on both sides and used to drive and measure ion current.

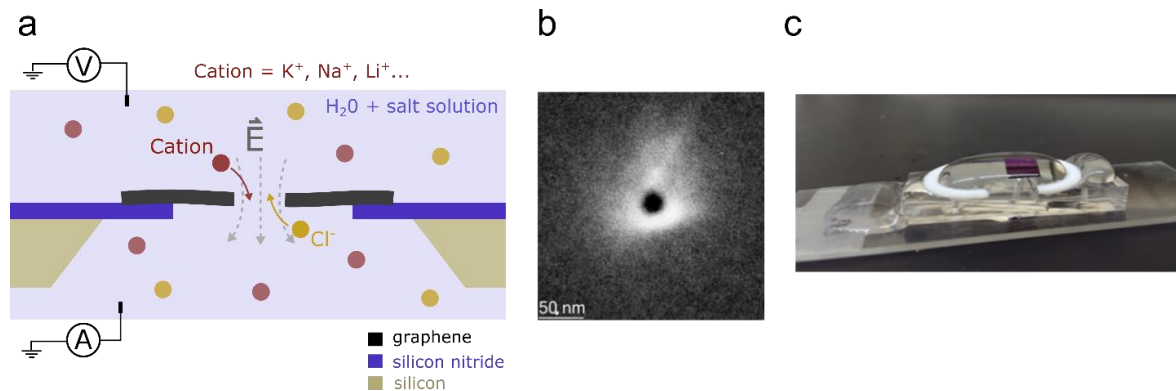


Figure 7.2 a) Cartoon schematic of the device geometry. The real suspended graphene region is 1 to 5 μm in diameter. b) Helium ion microscope (HIM) image of a nanopore. The region of white contrast is caused by hydrocarbon contamination deposited around the pore mouth during the HIM milling process. c) The PDMS flow cell and mounted Si/ SiN_x chip.

We introduce pores of controlled diameter into CVD graphene membranes using a helium ion microscope (HIM). The graphene is bombarded with He^+ ions at a high enough energy to perforate the crystal over a controlled area. Pores as small as 20 nm can be produced with this method. The details of SiN_x chip fabrication and HIM milling are discussed in detail in Cantley, 2017.

Before measurement, we first inject ethanol on either side of the graphene membrane, which has a low surface tension and therefore encourages the full wetting of the pore. We then flush the EtOH with DI water filtered (MilliQ) just prior to measurement, then inject the salt solution.

We find that different devices of similar pore diameters (50 – 75nm) can have significantly different IV characteristics. Even the same device re-wet multiple times can yield very different IV curves. Devices tend to be in one of 3 broadly defined states i) completely non-conductive, ii) low conductivity, ion selective and with non-linear IV curves, or iii) high conductivity with linear IV curves. An example of each of these states in a 0.1M KCl solution is shown in Fig. 7.3a. The IV curves for a device in *state ii* with various salt solutions is shown in Fig. 7.3b.

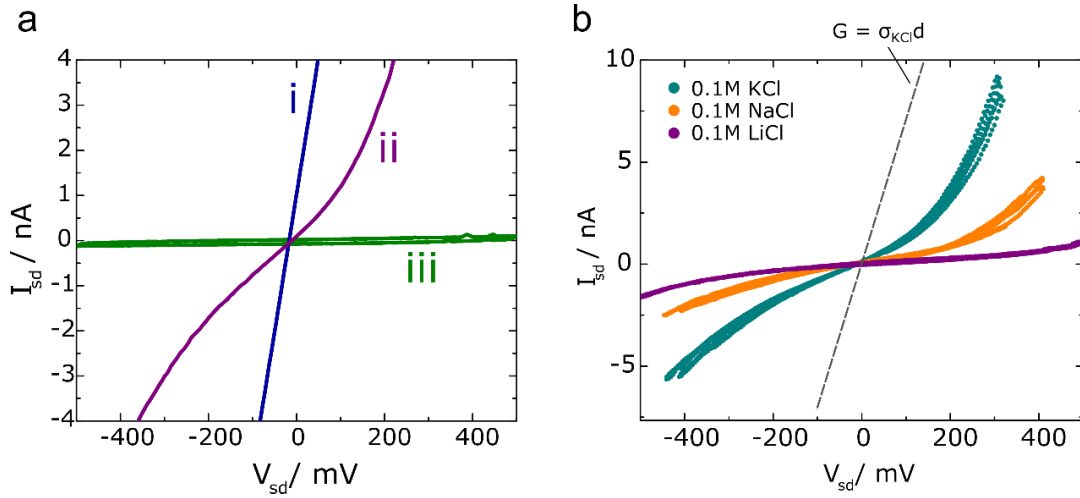


Figure 7.3 a) The IV characteristics for pores in three different states. Large linear conductance (i), low non-linear conductance (ii), and non-conductive (iii). b) The cation selectivity of a 50 nm pore device in *state ii*. The dashed line represents the predicted conductance curve for a pore of this diameter.

The low conductivity, non-linear behavior of *state ii* is of particular interest, because it shows a high selectivity between cation species. This behavior is unexpected in three important ways. Firstly, the diameter of the pore (50 nm) is enormous compared to the sizes of the various cations. The pore is therefore expected to be non-selective between ion species. Secondly, the non-linear IV curves suggest ‘activated’ or Arrhenius type transport where the ion are traversing an energetic barrier to pass through the pore. This can occur in very small pores (e.g. < 1nm), but 50 nm pores are expected to have linear IV curves. Thirdly, the expected conductance G for nanopores with a pore diameter d (assuming $d \gg$ the membrane thickness) is approximately

$$G = \sigma d \quad (\text{Eq. 7.1})$$

where σ is the bulk conductivity of the solution. The conductance of the *state ii* device in Fig. 7.3b is roughly 10x smaller than expected.

7.3 In-situ AFM imaging

Such results suggest that the pores in *state ii* are occluded in some way. In order to understand the cause of the occlusion we used liquid AFM to monitor the physical state of the nanopores while (or right after) IV measurements were taken.

AFM images were taken with an Asylum MFP-3D microscope operated in tapping mode. Platinum-iridium coated silicon AFM tips (ARROW-NCpt) were used for air imaging. For fluid imaging, Si₃N₄ tips (PNP-TR, spring constant $k_c = 0.32$ N/m) were driven at a free air amplitude of around 50 nm. After tip engagement, the set point amplitude was adjusted to be as high as possible, set just below the value at which the tip lost contact with the surface. This meant the tip would exert the smallest possible forces and avoid modifying the topology of the sample being measuring. Scanning speeds were approximately 3 $\mu\text{m/s}$, and post-processing of the images was carried out to remove low frequency noise.

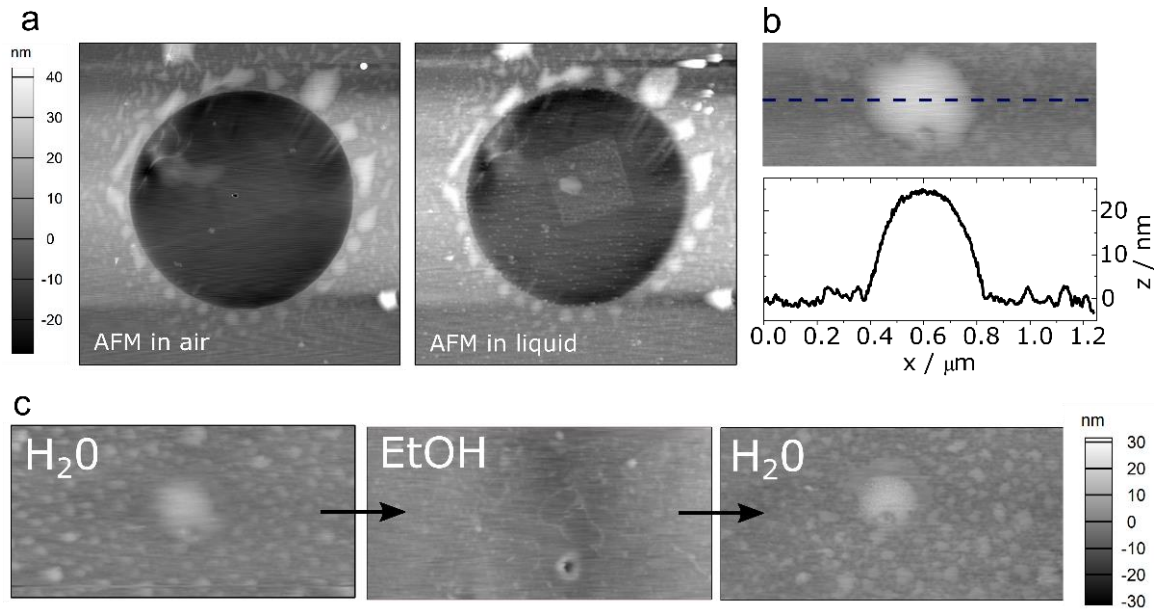


Figure 7.4 a) A device with a 50 nm pore, imaged with AFM first in air then in H₂O. The pore region is occluded when in liquid. The square region around the device is caused by hydrocarbons introduced during HIM imaging. b) A zoom-in and cross section of the bubble-like object occluding the pore. c) AFM images of the bubble in water and ethanol. The bubble disappears when water is replaced with EtOH, and re-appears when water is re-introduced. The images are imperfectly aligned due to sample drift.

We first imaged a device with a diameter of 50 nm with an AFM in air (Fig 7.4a). We then wet the device with ethanol, then water, then salt solutions containing KCl, NaCl or LiCl and took IV curves for each salt solution, with data plotted in Figure 7.3b (introduced earlier). Pure water was used to thoroughly flush out the device between each salt measurement to avoid cross contamination of cations. Immediately after the IV measurement we used liquid AFM to profile the surface of the membrane (Fig 7.4a). A distinctive bubble-like object can be clearly seen around the pore of the membrane. The object has an extremely low aspect ratio, with a diameter of ~400nm and a height of ~20 nm (Fig. 7.4b). We found that replacing the water with ethanol, the bubble disappears

(Fig. 7.4c), which then returned when the liquid was switched to water again. The device was not dried out during the exchange process.

We also probed the stiffness of the object occluding the pore by varying tip-sample forces during scanning. This was done by reducing the amplitude set point ratio (the ratio between the amplitude set point and the free air amplitude), which increases the forces on the sample from the tip. Figure 7.5 shows the result of imaging the pore in water with different set points ratios. The lower set point ratio of 30% caused the tip to deform the object over the pore (Fig. 7.5a) as compared with images using higher set point ratios of 36% (Fig. 7.5b). This means the object is soft and malleable, yet returned to its previous topology as soon as tip-sample forces were reduced (Fig. 7.5c).

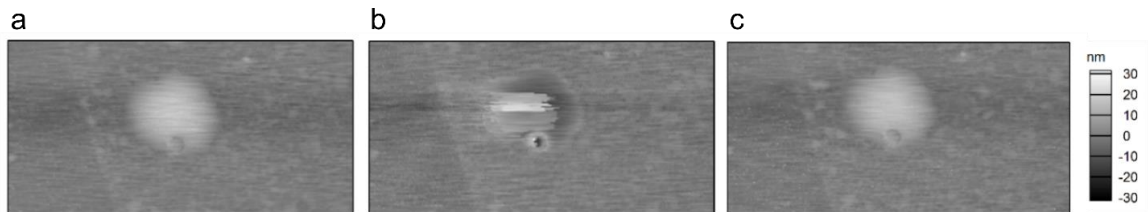


Figure 7.5 AFM images of the pore taken in water with different set point ratios of (a) 36%, (b) 30%, and back to 36% again (c). The lower set point ratio increases tip-sample forces which deform the bubble.

We found that some devices do not have bubbles occluding the pore, and when this is the case the conductance is linear, non-selective between cations, and very close to the magnitude predicted by Eq. 7.1. An example of such a device is shown in Fig. 7.6a and b. All six devices of the devices measured in liquid AFM with the same protocols described above showed presence of nanobubbles, and devices measured had a

systematically lower conductance than would be expected for their pore size (see appendix C1 for details).

7.4 Nanobubbles in nanopores

The aspect ratio of the bubbles, and their response to AFM tip-sample forces (An, Tan, & Ohl, 2016), are consistent with two types of nanoscale bubble that are commonly found in liquids. These bubbles are either composed of gas and called *nanobubbles*, or composed of oils which are called *nanodroplets* (Lohse & Zhang, 2015). Our AFM measurements cannot distinguish between the two cases, however the experimental conditions are conducive to the appearance of either type. Nanodroplets can be produced by PDMS (Berkelaar et al., 2014), a material which we use to construct our flow cell. While cured PDMS is insoluble to EtOH and water, any uncured silicone oils in the block could dissolve and condense on our graphene membranes. Alternatively, a gaseous nanobubble could be produced as a result of using EtOH to wet the devices before exchanging it with water. This wetting method is standard in the field (Jiandong Feng et al., 2016; O'Hern et al., 2014; Thiruraman et al., 2018), but is also unfortunately identical to the method nanobubble researchers use to nucleate a high density of gaseous nanobubbles (Lohse & Zhang, 2015). It would therefore be unsurprising for a graphene nanopore in these conditions to be frequently clogged by bubbles of either type.

The presence of nanobubbles and nanodroplets explains the various pore states

shown in Fig. 7.3a. *State i* pores are free of bubbles and therefore conduct as expected from Eq. 7.1 with no cation selectivity. *State iii* pores are those which are either covered in a macroscale bubble which has completely de-wet the pore area, or is blocked by some other form of contaminant. *State ii* pores are covered in nanobubbles whose dimensions are only a few times larger than that of the pores, which therefore allow some ions to cross it. These ions must traverse a non-aqueous bubble, which requires energy to shed their hydration shells. This results in a significant energy barrier to transport, which explains the low conductivity and non-linear activated behavior of the IV curves. The ion selectivity of the device results from the large differences in ion hydration energies of the different cations measured. The order of the cation conductances ($K^+ > Na^+ > Li^+$) follow the order of their relative hydration energies, with higher hydration energies reducing the conductance due to the higher energy barrier it creates.

In order to avoid any bubbles, droplets or other contamination from sticking to the nanopores, we performed a set of experiments in which we imaged graphene nanopores with liquid AFM in the cleanest possible conditions. Graphene nanopores and chips were fabricated as before, but now mounted on clean glass slides using SU8 epoxy as glue. SU8 is highly insoluble and clean, and so cannot dissolve contaminants into EtOH or water which could condense on our nanopores. The mounting was done in a cleanroom to avoid any other contamination or oils, and the chips were annealed in vacuum prior to transfer to remove any hydrocarbon residues. All liquids were degassed for ~ 1h before the experiment in a vacuum desiccator, which removes gases dissolved in water and

discourages the formation of gaseous nanobubbles.

The devices were wet with pure EtOH, which was then slowly replaced with a solution of EtOH:H₂O = 1:1, then finally wet with pure DI H₂O. The device was then imaged with liquid AFM, after the AFM cantilever and cantilever holder were thoroughly cleaned with EtOH and water. We first imaged a pristine graphene membrane with no nanopore in air (Fig. 7.6c) and water (Fig. 7.6d). The cleaner mounting technique considerably improved the membrane cleanliness, and there is a big reduction in the number of nanoscale bubbles surrounding and covering the device. We then rewet the same device using EtOH and water that had been passed once through a PDMS flow cell, but following the same sequence of wetting as described before. Figure 7.6e shows that this device became covered in PDMS nanodroplets, which suggests that these may have been a significant source of contamination in our earlier measurements. Finally, we image a device with a 150 nm HIM drilled nanopore, wetted with clean EtOH and H₂O. This device had no discernable bubble-like objects on the membrane, however the profile of the pore region suggests that the nanopore picked up contamination around the pore mouth. These results suggest that even when the membranes are free of nanobubbles or nanodroplets, the pore mouth can become rapidly covered in contaminants.

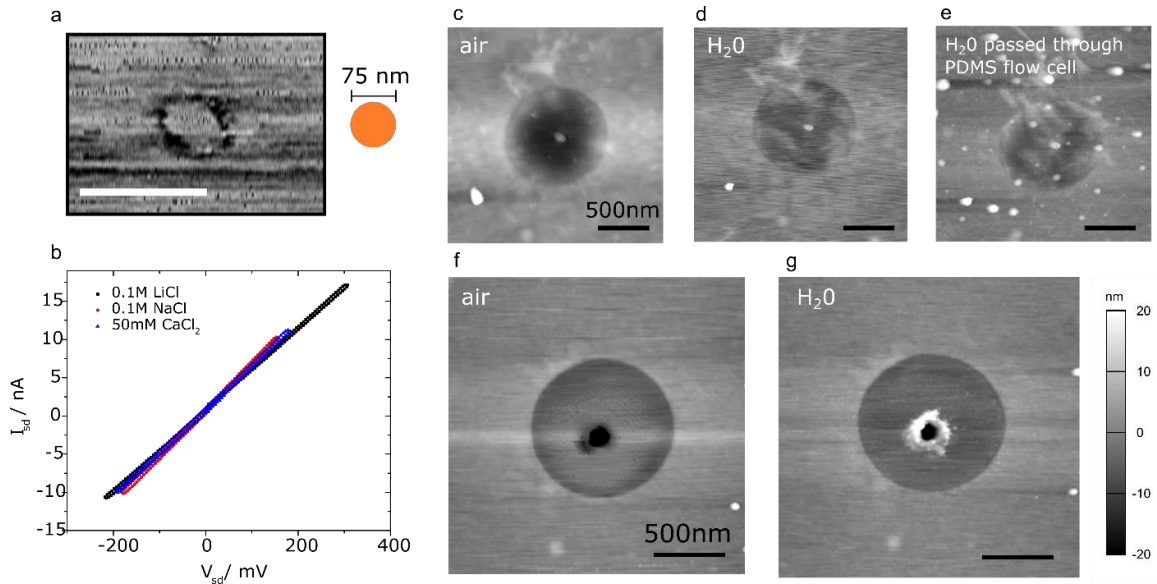


Figure 7.6 a) AFM phase channel image of a 75 nm diameter pore with no pore occlusion. The phase channel was used to get the best contrast for the pore edges. Scale bar is 200 nm. b) Conductance curves for the device shown in (a). Based on the conductance curves and Eq. 7.1 the predicted pore radius is 74 nm, in good agreement with the AFM images. c) AFM of a device in air and d) imaged in water. The device appears much cleaner using the new mounting procedure. e) Adding liquid that has passed through a PDMS flow cell makes the device significantly more dirty. f) Another device with a 150 nm pore is imaged in air then g) in water. The pore is free of bubbles, but immediately became covered in what appears to be some other kind of contaminant.

7.5 Discussion

The results described here present a problem for the study of graphene nanopores. Our findings show that nanopores are easily contaminated and that even if nanobubbles and nanodroplets are eliminated, other contamination appears to stick preferentially to the pore mouth. This means that measurements that are assumed to be of ion transport through of atomically thin nanoporous membranes, may instead be measurements of ions passing through a layer of contamination occluding the pore. Such contaminated pores

could easily be mistaken for < 1 nm pores from their conductance curves alone. Indeed, our results show that a 50 nm pore occluded with a bubble produces IV curves with a non-linearity and cation selectivity that are commensurate with behavior one would expect from < 1 nm pores (Jiandong Feng et al., 2016). It is therefore unwise to rely solely on electrical conductance curves to characterize graphene nanopores.

As long as the state of the pore can be monitored with an independent method in real time, the contaminated pores can easily be rejected and pristine pores can accurately be characterized. Much of the research in the literature however does not have this alternative means to probe the state of the pore, since membranes are usually contained within flow cells that prohibit such access. Recent work by Marion, 2019 suggests that the variation of the pressure at either reservoir could provide a method to accurately identify occlusions to pores.

To avoid mistaking contaminated false positives with truly nanometer scale pores, great care should be taken to prevent nanobubbles, nanodroplets, and other sources of contamination by thoroughly degassing liquids and avoiding silicone sealants. Care must also be taken statistically, to not only report data from devices with intriguing IV, since such selection will distort an accurate description of the true range of behaviors of the nanopore. These results also point to a particular weakness of the HIM milling method, which tends to accrue hydrophobic hydrocarbons around the pore mouth that may promote the accumulation of other contaminants.

It is important to point out that the contamination observed in our devices (e.g. Fig. 7.4a and Fig 7.6g) may not be indicative of the results seen in other labs, who have different experimental set-ups and wetting protocols. The results described here may therefore not be generalizable to all graphene nanopore experiments, although recent work suggests that our findings are reproducible in other labs (Marion, Macha, Davis, Chernev, & Radenovic, 2019). They do however provide an existence proof, showing that such contamination is likely and should be ruled out directly before assuming the pristine cleanliness of a graphene nanopore.

7.6 Conclusions

The results of this chapter show that various forms of contamination frequently stick to graphene nanopores, which can lead to distortions in the characterization of the pores. We found that 50 nm pores can be occluded by nanobubbles or nanodroplets, which give the pores a small, non-linear conductance and cation selectivity which is suggestive of the behavior of much smaller pores. Devices without bubbles have a conductance equal to the expected theoretical value. Efforts to remove contamination were partially successful, however we found that pores can still be contaminated even when using materials of clean room grade cleanliness. These results will help other researchers avoid misinterpreting occluded pores for ~ 1 nm diameter ones, and provide a method to monitor pores in-situ to confirm the physical state of pores during electrical measurements.

CHAPTER EIGHT: FUTURE WORK AND CONCLUSIONS

8.1 Nanofluidic switches using graphene electrowetting

During the ion transport studies described in the previous chapter, the graphene membranes were assumed to remain fully adhered to the substrate during electrical measurements. In-situ AFM measurements showed however that the voltage driving ions across the membrane occasionally resulted in the delamination of the membrane from its substrate (Fig 8.1). A similar mechanism was proposed in van den Beld, 2016 to explain non-linear conductances at larger voltages ($V_{sd} \geq 500\text{mV}$). Such a mechanism is therefore a confounding factor in studies intending to investigate nanopore behavior, and would also be a problem for any technological applications of nanoporous 2D materials. This effect could be harnessed too for new applications, with the controlled peeling of the membranes used to make nanoscale switches for controlling flow in nanofluidic circuits. Herein we present some initial data relating to this effect, which can serve as a basis for further study by others.

We used a similar geometry to that described in chapter 7, with the addition of a gold electrode connected to the graphene to allow gate voltages V_g to be applied (Fig 8.1b). The topside of the device remained dry during the experiments, which allowed AFM images to be taken straightforwardly in air rather than in liquid. We wet the back side of the device with water containing 0.1M KCl, and connected the liquid to the ground electrode. We then swept V_g and monitored the device with AFM.

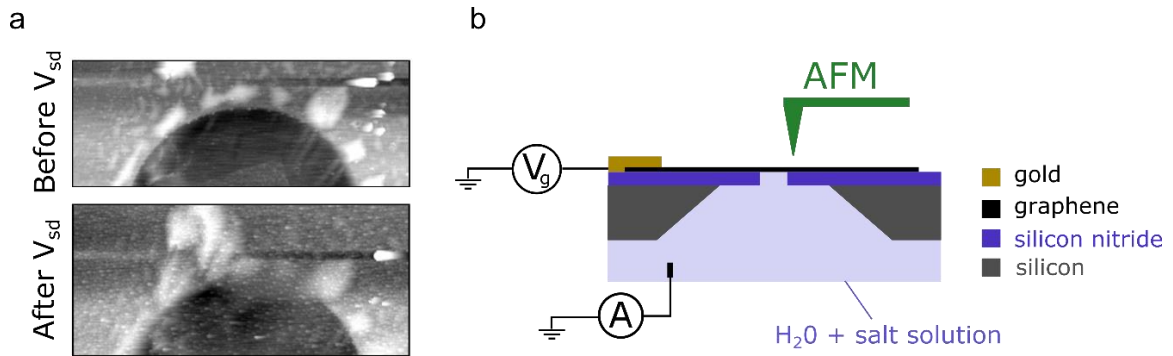


Figure 8.1 a) The application of V_{sd} in the geometry described in chapter 7 occasionally precipitated the delamination of the graphene membrane from the SiN_x substrate. b) The geometry used in this chapter involves applying a gate voltage to the graphene, and wetting only the back side of the membrane.

At $V_g = 5$, we observed the delamination of the membrane approximately symmetrically around suspended region of the device. Figure 8.2a & b shows in the height channel that the membrane is raised by ~ 5 nm in this region. The very large phase contrast visible in this region means that there are large differences in the tip-sample interaction forces in this region, which suggests that liquid has been drawn between the membrane and the substrate.

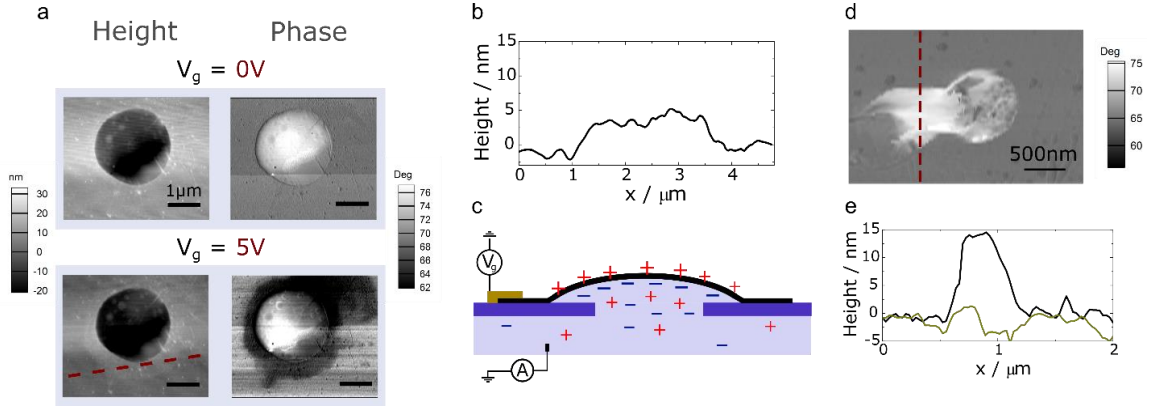


Figure 8.2 a) A gate voltage of 5V causes delamination of the graphene membrane, which can be seen in both the height and phase channels. b) The delaminated region is raised by approximately 5 nm. c) The graphene membrane and electric double layer have a capacitance that energetically drives the delamination process. d) Electrowetting can occur at small voltage magnitudes – in this case -0.3V. e) The delaminated region is raised by ~15 nm.

The mechanism for this can be simply explained as an electrowetting effect, by considering the capacitance of the graphene membrane with the ionic solution. When V_g is applied, charge builds up in the graphene layer which must be balanced by the accumulation of charge in the liquid double layer. This system stores charge with a capacitance C_m (Fig. 8.2c). The energy of the system F can be described in terms of this capacitive energy and the net adhesion energy γ of the membrane to the substrate,

$$dF = \gamma \cdot dA - \left(\frac{1}{2} C_m V_g^2\right) \cdot dA \quad (\text{Eq. 8.1})$$

where dA is change in the surface area of the graphene-liquid interface. We can see that increasing dA lowers the energy of the system when the condition

$$\frac{1}{2} C_m V_g^2 > \gamma \quad (\text{Eq. 8.2})$$

is satisfied, which suggests that there exists a threshold voltage for V_g before the membrane will spontaneously delaminate to minimize its energy (van den Beld, 2016). We performed further measurements using the electrically inert monolayer hBN as a dielectric layer between the substrate and the graphene to avoid any electrochemistry, and found that this threshold voltage can be as low as 0.3V (Fig. 8.2d & e). By using surface modifications to modify γ this threshold voltage may be even lower. Selective patterning of this surface modification could allow the direction and shape of the delaminating region to be controlled, which would allow it to be used to open and close connections controllably between other channels in nanofluidic circuits. Further work will need to improve the reproducibility of this effect to better understand the fundamental mechanisms at play, and which will allow future researchers to engineer the imagined devices.

8.2 Conclusions

This thesis has described methods to grow and transfer an atomically thin semiconductor, investigated how the band gap of this materials responds to mechanical strain and explored other mechanical properties of the material, and finally explored the use of graphene as a nanoporous separation membrane.

The initial experiments in chapter 4 concern the growth, transfer, and characterization of monolayer MoS₂ membranes. The novel growth method described here allows one to reliably grow large areas of high quality membranes, which can be

used to transfer to novel geometries. In our lab, MoS₂ produced by this method is being used to study the interlayer adhesion of van der Waals crystals, and used as an atomically thin coupled resonator or waveguide. My hope is that this ongoing work continues to lead to interesting and exciting new devices and discoveries.

In chapter 5 we measured the effect of biaxial strain on the band gap and Raman modes of MoS₂. The measured strain sensitivities will be a useful tool for other researchers who would like to quickly and easily determine the strains in their membranes, particularly after CVD growth which often induces intrinsic strains due to heating and cooling effects. We also showed that micron-sized areas of MoS₂ can be strained to very large strains, which would be unattainable for bulk materials. The corresponding band gap shift of ~25% exemplifies the extremely large band gap tunability available with this method. These results can be used to optimize MoS₂ for conventional applications, or be used to make pressure or strain sensors, and also provide a method for studying the diffusion of excitons and trions in large strain gradients. We then determined the Young's modulus and adhesion energy of MoS₂ in chapter 6, numbers which will be of importance in any nano-electromechanical applications of the material. We also found that our membranes had a considerable adhesion hysteresis. Understanding how these membranes peel on and off substrates may be useful for understanding hysteresis in nanoscale nano-electromechanical systems, and has practice use in the optimization of transfer processes.

Finally in chapter 7 we showed that graphene nanopores can become occluded by nanobubbles or nanodroplets, which substantially affect the conductance properties of the pores. The results of this work prove that conductance measurements alone are not a reliable way to determine device pore sizes, since large occluded pores and sub-nm pores are indistinguishable by this method. My hope is that the work of this chapter will provide impetus for future nanopore researchers to develop better techniques for confirming the cleanliness of the pore in real time. In this way, occluded pores can safely be discarded and the true properties of these fascinating systems can be fully explored.

APPENDIX A: ADDITIONAL DATA FOR CHAPTER 5

A1. Sliding and Repeatability

Under high strains our devices may be forced to slide over the substrate, an effect which has been observed in graphene (Kitt et al., 2013). This sliding would allow the membrane deflection δ to increase, and thus cause us to over-estimate the strain from our AFM measurements. To see if sliding has occurred, we plot the relationship between strain and the A peak position during the initial increase in internal pressures followed by the deflation of devices (Fig. A1). Device 1 shows little hysteresis, however Device 2 shows evidence of significant sliding. This can further be confirmed by the AFM images of the devices after deflating, with Device 2 showing wrinkling which was not previously present. To avoid any influence of this effect on our data presented in Fig. 5.2, we only used data taken from devices which showed none of these signs of sliding.

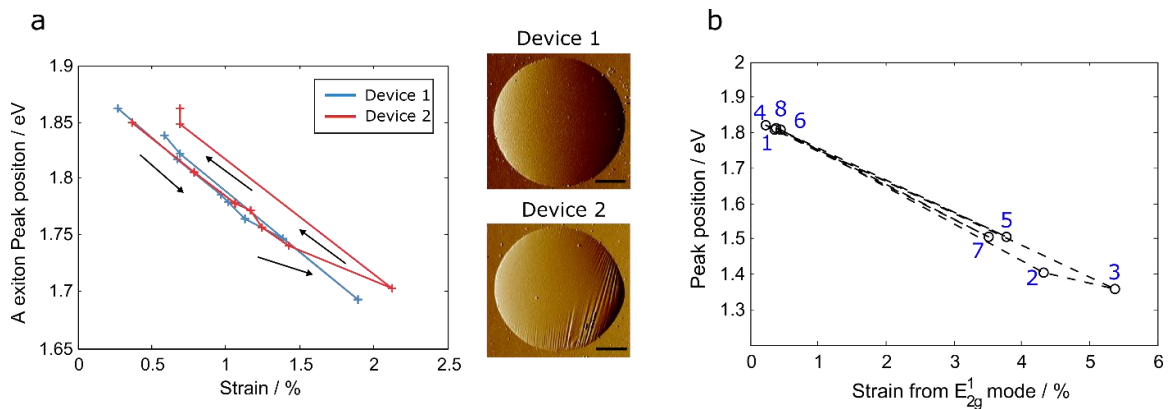


Figure A1 a) An example of the peak shift in two monolayer devices in which p_{int} was increased then decreased, with AFM images of both devices after pressure cycling (scale bars are 2 μm). Device 2 shows evidence of slipping. **b)** The repeatability of subjecting a device to high strain. Measurements were taken in the sequence indicated.

A2. Strain dependence of the A exciton intensity – a comparison with theoretical predictions.

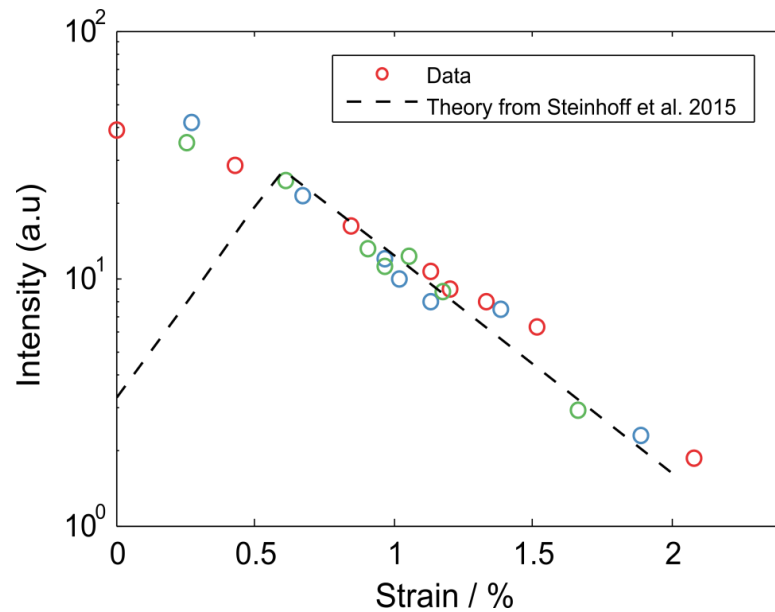


Figure A2 Comparison of the change in A peak exciton intensity with strain to a theoretical prediction. The intensity of our data has been scaled for comparison with the theory.

The exponential decrease in A peak intensity shown in Fig 2a inset of the main text compares well to the theory described in Steinhoff et al. at large strains (Fig. A2). At strains below 0.5 % however, they predicted that the PL intensity would increase with strain, caused by changes in conduction band minima at the Σ point of the conduction band. We did not observe such an enhancement over this range, however the difference may be due to different estimates of the doping level in the theory and the true doping level in our devices.

A3. Interference effects

The interference between light scattered of the MoS₂ membrane and the silicon at the bottom of the well may affect the relative intensities of the A_{1g} and E¹_{2g} modes (Fig. 5.5a). To rule this out as the cause of our observed changes to Raman mode intensities, we closely follow a model developed in other works (Carvalho et al., 2015; Song-lin Li, Miyazaki, Song, Kuramochi, & Nakaharai, 2012) originally used to determine the effect of the substrate thickness on the Raman mode intensities. In our case, instead of a layer of SiO₂, we have a vacuum cavity of distance d_2 which changes as the device bulges down under high pressures (Fig. A3a). Using the Fresnel equations, we can deduce the change in intensity of each MoS₂ Raman mode relative to the Si peak, as d_2 decreases from its unstrained value of 1.5 μm (equivalent to the depth of the well) with increasing strain. We deduce the value of d_2 by using the Hencky model described in the main text, which can be used to convert strain we determined from the E¹_{2g} peak position, to a membrane deflection δ . d_2 is then equal to the difference between δ and the well depth. We also account for the strain induced shift of each mode in these calculations, which makes the wavelength of the scattered light also dependent on strain.

The model is plotted against our data in Fig. A3b & c, and the intensity of the model curve is scaled in order to be in coincidence with our data at low strains. We find both the E¹_{2g} and A_{1g} peak intensities increase beyond what is expected from the interference model at high strains. We therefore conclude that the observed increase in

both Raman mode intensities at high strain was not due to the effect of interference, but was rather an intrinsic property of the material under strain. Similarly, the interference model does not account for why the ratio E_{2g}^1 / A_{1g} increases so dramatically. As the Raman modes are so similar in energy, interference effects should cause less than a 10% change in this ratio, and so we conclude that this is also strain induced effect.

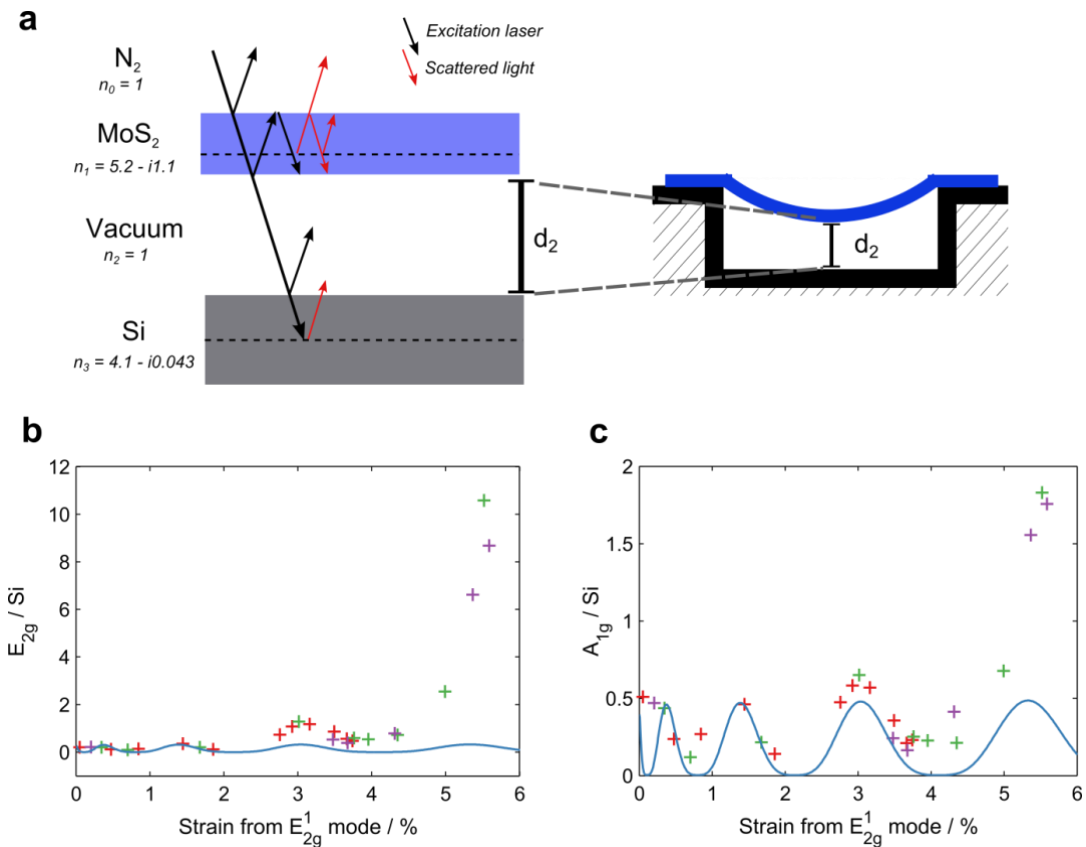


Figure A3 a) A ray diagram of incident and scattered light. The effective power of the excitation laser (black) is the sum of the incident beam with its reflected beams. The intensities of Raman scattered light (red) also depend on the sum of reflected rays, and rays scattered at different phases within the MoS₂ or Si. The effect of this interference for each frequency of light depends on the distance between membrane and substrate, d_2 , which changes as the devices are strained. **b) & c)** The intensities of the E_{2g}^1 and A_{1g} peaks relative to the Si peak. We compare our data (crosses) to the interference model (blue line).

A4. Additional Raman data

We plot the ratio of the integrated intensities of the two Raman modes (E_{2g}^1/A_{1g}) for different membrane thicknesses in Fig. A4. All three thicknesses have approximately the same E_{2g}^1/A_{1g} at zero strain, and each show some small increase in this ratio with strain.

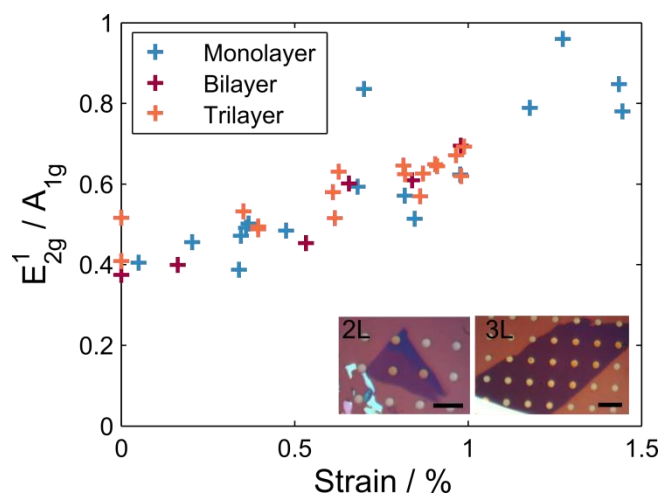


Figure A4 The ratio of integrated intensities of the E_{2g}^1 to A_{1g} Raman modes for different membrane thicknesses.

In a final experiment, we took line-scans of the Raman modes of a pressurized device, to see if the varying angle of the membrane relative to the laser produced the changes to the Raman mode intensities that we observe. As strain increases in our devices, the curvature of the membranes also increases, and as our laser spot has a finite size this change in curvature would change the angle between the incident light and the membrane. To rule this out as a cause of the change in Raman mode intensities, we plot the intensities of the Raman modes as a function of distance x across the device with $\Delta p =$

1599 kPa, corresponding to a biaxial strain at the center of the device of $\sim 5.6\%$ (Fig A5a). If changes in angle between the laser light and membrane were causing increases in Raman intensity, we would expect the largest change to occur at the edge of the membrane, where the angle change would be the most. However, Fig. A5c and Fig. A5d show that this is not the case. Intensities of both Raman modes and the ratio E_{2g}^1 / A_{1g} are both largest in the center of the device, where the biaxial strain is the most and the membrane is closest to being flat. We therefore rule out the changing membrane angle as the cause of these intensity changes.

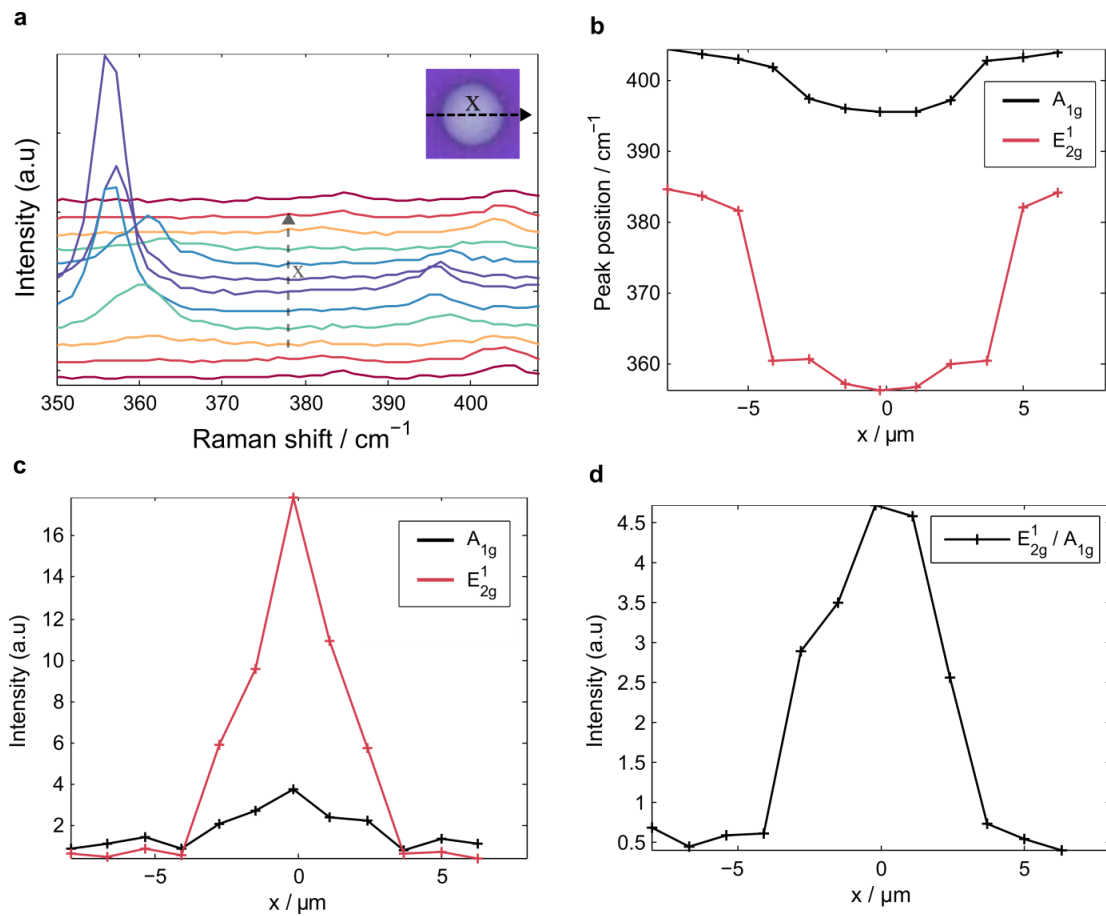


Figure A5 a) Line scan of Raman modes across a device. b) Peak positions and c) peak intensities of the Raman modes (normalized to the Si peak) across the device. d) The ratio E_{2g}^1 / A_{1g} of the two Raman mode intensities across the device.

APPENDIX B: ADDITIONAL DATA FOR CHAPTER 6

B1. The effect of membrane pre-tension

Even when there is no pressure difference across the membrane there is usually a residual pre-strain observed in suspended devices, due either to the transfer procedure or the membrane sticking to the sidewalls of the cavity (Bunch et al., 2008). We can estimate the pre-tension in our membranes by using photoluminescence spectroscopy. In an earlier paper (Lloyd et al., 2016) we showed that the band-gap in monolayer MoS₂ reduces when biaxial strain is applied, at a rate of -99 meV/%. We took a PL spectrum of a device with no pressure difference across the membrane, meaning any observed strain would correspond to the pre-strain. We can then convert this to a pre-tension using the formula (Campbell, 1956),

$$\sigma_0 = \frac{E_{2D}\epsilon_0}{1-\nu} \quad (\text{Eq. B1})$$

Our devices have a pre-strain of $\epsilon_0 < 0.002$ which corresponds to a pre-tension of $\sigma_0 < 0.2$ N/m, which is comparable to previously reported values for atomically thin membranes in this geometry (Bunch et al., 2008; L. Wang et al., 2012). Campbell, 1956 showed that when the non-dimensional parameter,

$$P = \frac{\Delta p a E_{2D}^{1/2}}{\sigma_0^{3/2}} \quad (\text{Eq. B2})$$

satisfies the condition $P > 100$, Hencky's formula in Eq. 6.1 in is correct to within 5%. Most of our data points were taken in a high enough pressure range to satisfy this condition. For instance for the data presented in Fig. 6.2a, $P = 100$ when $\Delta p = 350$ kPa. Since nearly all of our data was taken with $\Delta p > 350$ kPa we use Eq. 6.1 to calculate E_{2D} , and neglect the effect of the pre-tension.

B2. Work of separation

The full set of data used to produce means and standard deviations of each sample in Fig. 3 of the main text is shown in Fig. B1. Each data point represents the measured value of Γ_{sep} for an individual device of a given sample.

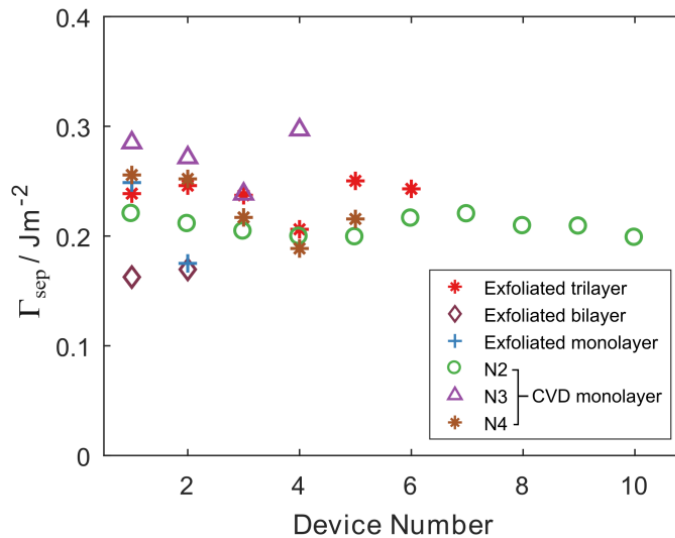


Figure B1 All Γ_{sep} data used to calculate means and standard deviations of each sample in Fig. 6.3.

B3. Calculating the work of adhesion – additional figures

The relationship described in Eq. 6.5 predicts that the value of δ_c is roughly proportional to a_p for the devices measured, assuming the work of adhesion remains roughly constant. This is corroborated by measurements in Fig. B2 which plots δ_c against a_p and shows a roughly linear trend. We can estimate the value of Γ_{adh} by fitting this relationship to the values of δ_c and a_p of devices just before the snap in transition occurs, and we plot this line of best fit in Fig. B2 which corresponds to $\Gamma_{adh} \sim 14 \text{ mJ/m}^2$.

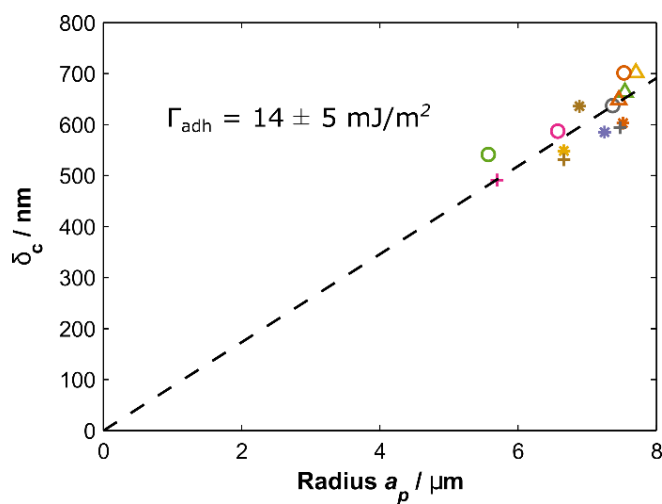


Figure B2 Data for devices measured on sample N2, showing the values of δ_c and a_p just before snap-in used to calculate Γ_{adh} . Each color/symbol represents a different device.

The complete data for comparing the work of adhesion of various samples is presented in Fig. B3a, with each data point representing a measurement of Γ_{adh} in a single device of a given sample. This data was used to produce Fig. 6.7b. A few of the devices measured did not snap in completely from radius a_p to a_0 , but rather initially snapped in

to an intermediate radius followed by a second snap in to a_0 (Fig. B3b). All the transitions between these states were unstable and occurred in less than one second.

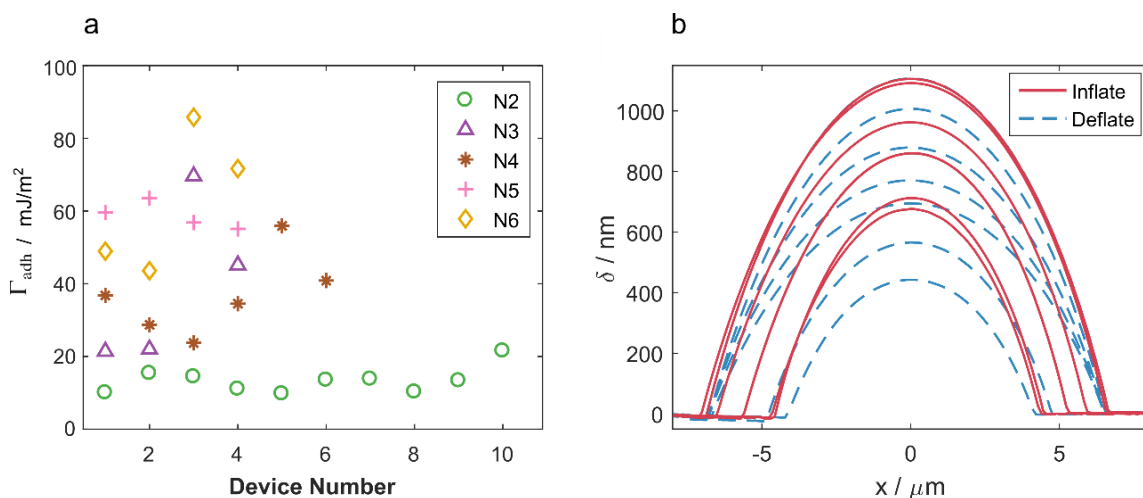


Figure B3 a) Work of adhesion for every device measured in each sample. b) A device which delaminates stably with increasing pressure, but shows adhesion hysteresis upon deflation. This device snapped in to an intermediate step before fully re-laminating to the substrate.

B4. Strain trapping around the edge of the membrane

To investigate a possible mechanism for the observed adhesion hysteresis we used Raman spectroscopy to measure the strain distribution around our devices. The peak positions of the Raman modes in monolayer MoS_2 are known to be sensitive to strain (Conley et al., 2013b; Lloyd et al., 2016), so by measuring how these peaks shift at different locations around the device we can build up an image of how strain is distributed. For these measurements we used the E^1_{2g} peak to estimate the strain, since it has a peak position which is strain sensitive and independent of doping effects.

Fig. B4a shows an AFM image of a device delaminated to $a_p \sim 7.5 \mu\text{m}$, which was then left to deflate and undergo the snap-in transition. A Raman map was then taken after snap-in (Fig B4b), with the strain calculated from the position of the E_{2g}^1 peak using the reported shift rate of $\sim 5 \text{ cm}^{-1} / \%$ (Conley et al., 2013b; Lloyd et al., 2016). A region of $\varepsilon \sim 0.5\%$ can be clearly seen around the circumference of where the delaminated bubble was before snap-in. This strain likely originates from the pressure induced radial strain at the edge of the bubble, which for these devices is $\sim 1.5\%$ (Fig. B5d). Using this upper bound of $\varepsilon \sim 1.5\%$ and the formula for the isotropic strain membrane energy density (Gould, 2013), $U = \frac{1}{2} E_{2D} \varepsilon^2$, we can estimate the energy stored in the strained regions to be $U \sim 20 \text{ mJ} / \text{m}^2$, which can account for some but not all the energy dissipation which produces a difference between Γ_{adh} and Γ_{sep} . The presence of strain in the membrane also implies some contribution of energy dissipation through friction as the membrane changes its length on the surface of the substrate (Kitt et al., 2013).

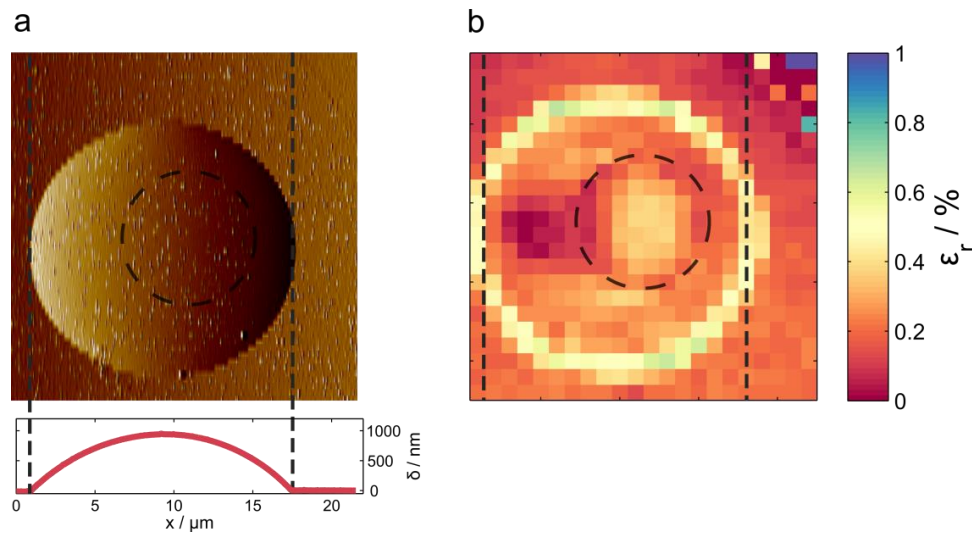


Figure B4 a) AFM image (amplitude channel) of a delaminated device before the snap-in transition. The position of the microcavity is marked by a dashed circle. Below is a cross

section of the device. b) Strain map of the same device after the snap-in transition when the device has fully deflated. Strain is calculated using the peak shift in the E_{2g}^1 Raman mode at each point. Each pixel is $1 \times 1 \mu\text{m}$ and corresponds to a single Raman scan.

In order to observe the process by which this strain becomes ‘trapped’ in the membrane around the device, we took Raman line scans over a cross section of a device as it deflated and plotted the E_{2g}^1 peak position as a function of distance (Fig. B5a and B5b). Before each Raman scan we found the corresponding geometry of the device by taking an AFM image (Fig. B5c). Across the delaminated bubble region (marked by dashed lines) the peak shift abruptly increases at the edge of the bubble, followed by a gradual increase towards the center of the device. In Fig. B5d we used Hencky’s solution to find the predicted strain profile across the device for its initial geometry (Fig. B5c red line) before deflation. In the model, the strain jumps from zero to purely radial tensile strain at the edge of the device, with the tangential component gradually increasing from zero to be equal to the radial component at the center. The E_{2g}^1 peak position depends on contributions of both the radial and tangential strain, so this model explains the profile seen in Fig. B5a.

Fig. B5b shows that a region of strain extends $\sim 1.5 \mu\text{m}$ outside the edge of the bubble in the initial Raman scan (red line). As the device deflates and the radius remains pinned, the peak shift across the delaminated region of the membrane reduces as it becomes less strained, however the region of strain outside the bubble remains roughly constant throughout deflation. These results show that the ring of strain in Fig. B4b is formed when the device initially delaminates, and that this strain does not relax as the

device deflates and eventually snaps in.

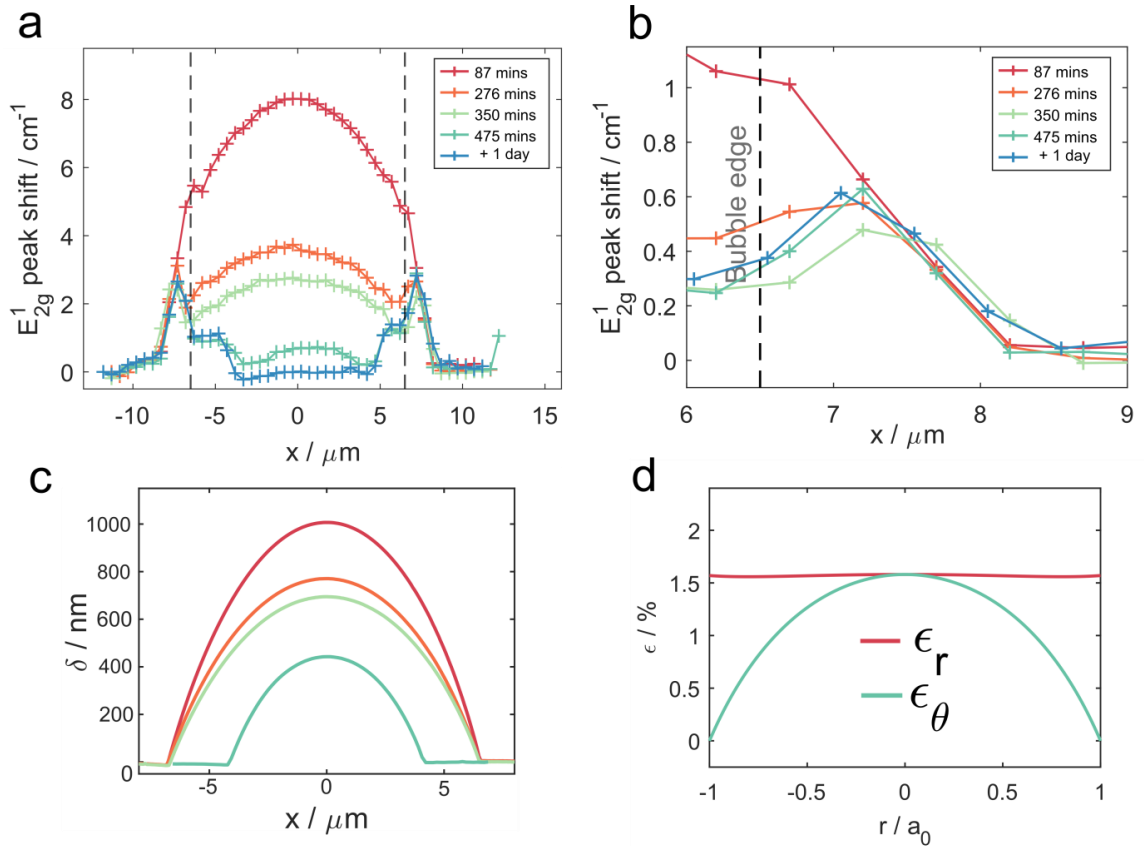


Figure B5 a) Raman line scans over a device over time as it deflates. Dashed vertical lines mark the edge of the delaminated bubble. b) A zoomed in version of a) focusing on the edge region of the device. c) AFM cross sections of the device at each time, using the same color scheme as in a). d) Radial (ϵ_r) and tangential (ϵ_θ) components of the strain as a function of radius for this device's initial geometry before deflating, calculated using Hencky's model with values for δ and a taken from the red curve in c).

B5. Contact angle of bubbles during deflation

Instead of analyzing the snap-out and snap-in data in terms of δ and a , an analogous method is to measure the contact angle θ_c between the membrane and the

substrate (see Fig. B6 inset) using an AFM. In Fig. B6 we plotted the contact angle against the radius of a device as it is inflated (black) and then left to deflate (red). As the device is inflated the contact angle increases until a critical value, at which point the device delaminates with the contact angle remaining constant. When the device is left to deflate the contact angle decreases at constant radius until another critical contact angle is reached, at which point the device undergoes the snap-in transition.

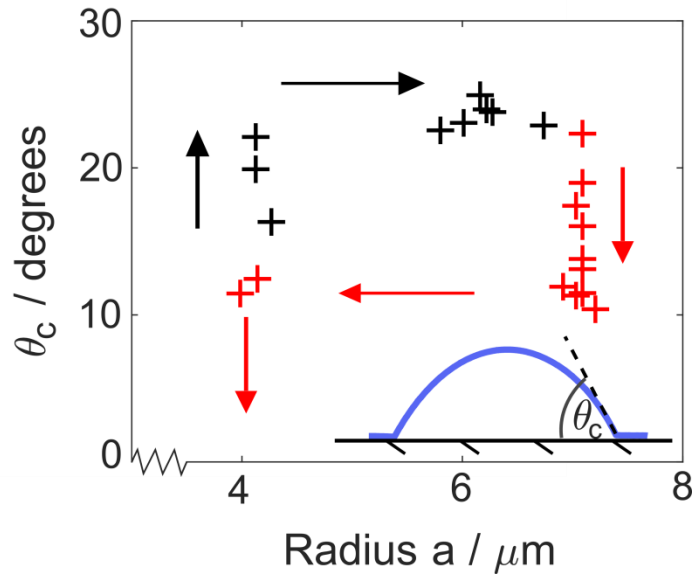


Figure B6 The contact angle of a device during inflation (black) and deflation (red).

B6. The effect of the slipping of the membrane on E_{2D} calculations

The strain at the edge of the bubble introduces extra slack into the membrane of bubble, which may affect our measurements of E_{2D} . We can estimate the effect this has on our measurements by integrating the strain over the strained region at the edge of the

bubble in Fig. B5b to find the total extra slack, ΔL , added to the bubble membrane. We can write the slack added to the membrane as,

$$\Delta L = \int_0^{x_1} \varepsilon(x) dx \quad (\text{Eq. B3})$$

The initial measurement in Fig. B5b (red line color and labeled ‘87 mins’) shows that the peak shift linearly decreases from $\sim 5.5 \text{ cm}^{-1}$ around the edge of the device to $\sim 0 \text{ cm}^{-1}$ at $1.5 \text{ }\mu\text{m}$ outside the device radius, so we take $x_l = 1.5 \text{ }\mu\text{m}$. To find $\varepsilon(x)$ we take $\varepsilon \sim 1.5 \%$ at the edge of the device (Fig. B5d) and use the linear strain profile seen in Fig. B5b, which leads to $\varepsilon(x) \sim (0.015/1.5) x \text{ }\mu\text{m}^{-1}$. This gives $\Delta L \sim 11 \text{ nm}$ over a device radius of $6.5 \text{ }\mu\text{m}$. This reduces the pre-strain by ~ 0.0017 which is about the same as the initial pre-strain. We therefore take this change to be negligible in to the pressure range we are studying due to the arguments made in section B1.

B7. Additional snap-in data

Figure B7a shows the complete data set for our snap-in measurements presented in Fig. 6.5b of the main text. This data was taken using an AFM in tapping mode. To confirm that the forces from the AFM tip were not affecting our results, we measured the snap-in of a device as it deflated by using solely optical measurements. We took sequential PL spectra at the center of the device as it deflated, where the membrane is under biaxial strain. In an earlier paper (Lloyd et al., 2016) we found that the PL peak

red-shifts under biaxial strain by -99 meV/%, so PL measurements allow us to measure the biaxial strain ε in the device. We can also measure the radius a of the device as it deflates using an optical microscope. Using these values for a and ε we can estimate the deflection of the device using the formula,

$$\varepsilon = \sigma(\nu) \left(\frac{\delta}{a}\right)^2 \quad (\text{Eq. B4})$$

where $\sigma(\nu)$ is a numerical constant which depends only on Poisson's ratio ν , and in this case $\sigma = 0.709$. We measured a deflating device using the non-contact optical method, after which we re-inflated the device to the same pressure and used the AFM to measure the geometry of the device as it deflated. We compare the results of these two methods in Fig. B7b, and find very similar results in the two cases. The device appears to snap-in at a slightly lower δ in the AFM measurements, however this is likely due to the long scan times (~ 3 min) required to take a PL spectrum meaning that we couldn't measure the device right at the moment before snap-in.

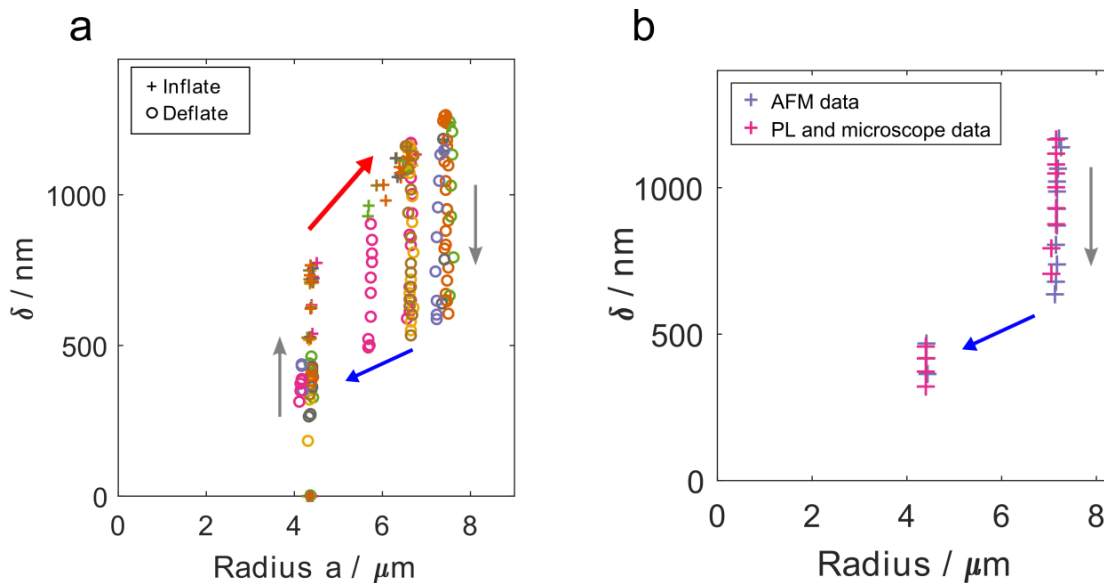


Figure B7 a) Complete data containing all data points of results presented in Fig. 6.5b in the main text. Each color represents a different device. b) Comparison of snap-in transitions measured optically or by AFM. For optical measurements a is determined using an optical microscope with a 100x objective, and δ is determined from the PL peak position and Eq. B4.

B8. Young's modulus

Figure B8 shows the complete data set used to calculate the Young's modulus for each device in Fig. 6.2b in the main text.

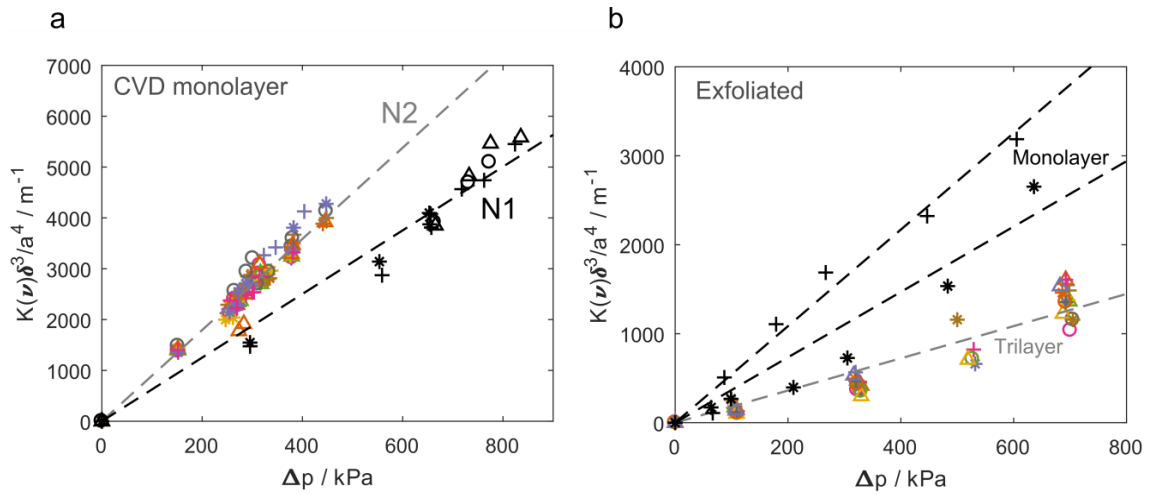


Figure B8 a) CVD monolayer devices from sample N1 and N2. b) Exfoliated monolayer and trilayers devices. Dashed lines are plotted for each of the sample means reported in Fig. 6.2c of the main text. Different color/symbols represent different devices.

APPENDIX C: ADDITIONAL DATA FOR CHAPTER 7

C1: The prevalence and formation of nanobubbles

To estimate the prevalence of nanobubbles in our experiments, we imaged six devices in water with AFM. We found the presence of nanobubbles in all six devices, four of which are shown in Fig. C1 as an example. Nanobubbles are distributed across the devices and are of various sizes. We found evidence of bubbles occluding the graphene nanopore in four of the six devices measured. The ethanol and water solutions were degassed in a vacuum desiccator for ~1h prior to measurement in three of these devices. In addition, we found that pores frequently had a conductance lower than is predicted analytically, given the imaged diameter of the pore. We interpret this as indirect evidence that the pore was obstructed due to bubble formation. We measured the pore diameter and conductance of aqueous salt solutions across 35 devices, and only two devices displayed a conductance magnitude consistent with what is predicted analytically for the imaged pore size. The other 33 devices all displayed lower than expected conductance values.

We hypothesize that the presence of hydrocarbon contamination around the pore mouth makes the pore region more hydrophobic, and therefore more prone to dewetting. This hydrocarbon contamination can be seen in Fig. C2 which shows a HIM image of a device after pore milling. The bright regions around the pore are caused by charging of

the electrically insulating hydrocarbons stuck to the graphene surface.

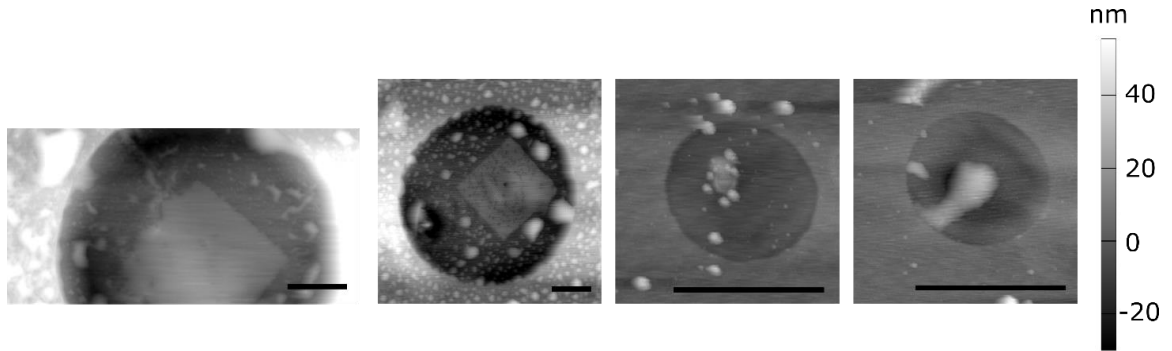


Fig. C1 Examples of other devices we imaged which are covered in nanobubbles. The devices were measured with AFM in water. Scale bars are 1 μ m.

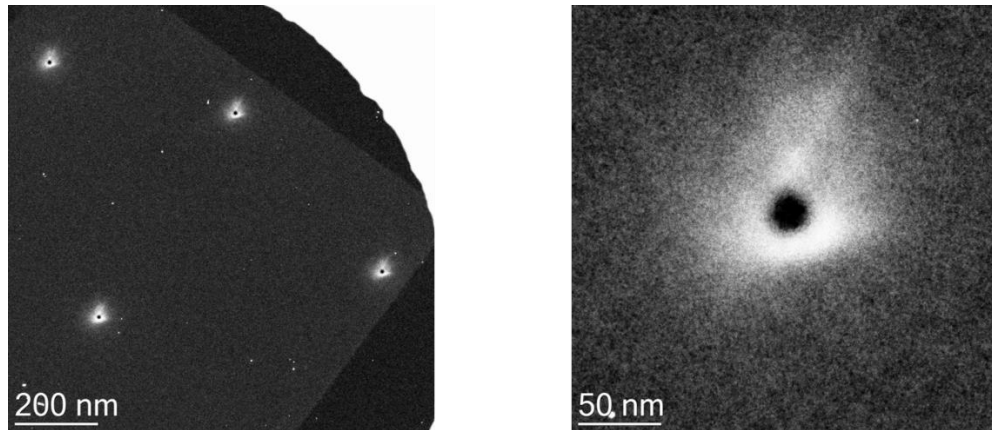


Fig. C2 Evidence of hydrocarbon contamination around the nanopore mouth after HIM milling. The white region indicates charging is occurring on the electrically insulating hydrocarbon layer.

BIBLIOGRAPHY

- Adams, A. R. (2011). Strained-layer quantum-well lasers. *IEEE Journal on Selected Topics in Quantum Electronics*, 17(5), 1364–1373.
<https://doi.org/10.1109/JSTQE.2011.2108995>
- Akinwande, D., Brennan, C. J., Bunch, J. S., Egberts, P., Felts, J. R., Gao, H., ... Zhu, Y. (2017). A review on mechanics and mechanical properties of 2D materials — Graphene and beyond. *Extreme Mechanics Letters*, 13, 42–72.
<https://doi.org/10.1016/j.eml.2017.01.008>
- Akinwande, D., Petrone, N., & Hone, J. (2014). Two-dimensional flexible nanoelectronics. *Nature Communications*, 5(5678).
<https://doi.org/10.1038/ncomms6678>
- Algara-Siller, G., Lehtinen, O., C.Wang, F., Nair, R. R., Kaiser, U., A.Wu, H., ... Grigorieva, I. V. (2015). Square ice in graphene nanocapillaries. *Nature*, 519, 443–447. <https://doi.org/10.1038/nature14295>
- Ali, A., Pothu, R., Siyal, S. H., Phulpoto, S., Sajjad, M., & Thebo, K. H. (2019). Graphene-based membranes for CO₂ separation. *Materials Science for Energy Technologies*, 2(1), 83–88. <https://doi.org/10.1016/j.mset.2018.11.002>
- An, H., Tan, B. H., & Ohl, C. D. (2016). Distinguishing Nanobubbles from Nanodroplets with AFM: The Influence of Vertical and Lateral Imaging Forces. *Langmuir*, 32(48), 12710–12715. <https://doi.org/10.1021/acs.langmuir.6b02519>
- Annett, J., & Graham, L. W. (2016). Self-assembly of graphene ribbons by spontaneous self-tearing and peeling from a substrate. *Nature*, 535(7611), 271–275.
<https://doi.org/10.1038/nature18304>
- Ashcroft, N. W., & Mermin, N. D. (2003). *Solid State Physics*. Brooks/Cole Cengage Learning.
- Bandaru, N., Kumar, R. S., Sneed, D., Tschauner, O., Baker, J., Antonio, D., ... Venkat, R. (2014). Effect of Pressure and Temperature on Structural Stability of MoS₂. *The Journal of Physical Chemistry C*, 118(6), 3230–3235.
<https://doi.org/10.1021/jp410167k>
- Beams, J. W. (1959). Mechanical Properties of Thin Films of Gold and Silver. *Proceedings of the International Conference on Structure and Properties of Thin Films*, 183–192.
- Berkelaar, R. P., Dietrich, E., Kip, G. A. M., Kooij, E. S., Zandvliet, H. J. W., & Lohse, D. (2014). Exposing nanobubble-like objects to a degassed environment. *Soft*

- Matter*, 10(27), 4947–4955. <https://doi.org/10.1039/c4sm00316k>
- Bertolazzi, S., Brivio, J., & Kis, A. (2011). Stretching and breaking of ultrathin MoS₂. *ACS Nano*, 5(12), 9703–9709. <https://doi.org/10.1021/nn203879f>
- Blakslée, O. L., Proctor, D. G., Seldin, E. J., Spence, G. B., & Weng, T. (1970). Elastic constants of compression-annealed pyrolytic graphite. *Journal of Applied Physics*, 41(8), 3373–3382. <https://doi.org/10.1063/1.1659428>
- Boddeti, N. G. (2014). *Adhesion Mechanics of Graphene*. University of Colorado Mechanical Engineering Graduate Theses & Dissertations.
- Boddeti, N. G., Koenig, S. P., Rong, L., Xiao, J., Bunch, J. S., & Dunn, M. L. (2016). Mechanics of Adhered, Pressurized Graphene Blisters. *Journal of Applied Mechanics*, 80(July 2013), 1–8. <https://doi.org/10.1115/1.4024255>
- Bunch, J. S., Van Der Zande, A. M., Verbridge, S. S., Frank, I. W., Tanenbaum, D. M., Parpia, J. M., ... McEuen, P. L. (2007). Electromechanical Resonators from Graphene Sheets. *Science*, 315, 490–493.
- Bunch, J. S., Verbridge, S. S., Alden, J. S., Van Der Zande, A. M., Parpia, J. M., Craighead, H. G., & McEuen, P. L. (2008). Impermeable atomic membranes from graphene sheets. *Nano Letters*, 8(8), 2458–2462. <https://doi.org/10.1021/nl801457b>
- Campbell, J. D. (1956). On the theory of Initially Tensioned Circular Membranes Subjected to Uniform Pressure. *Quarterly Journal of Mechanics and Applied Mathematics*, IX, 84–93. <https://doi.org/10.1093/qjmam/9.1.84>
- Cantley, L. (2017). *Biomimetic Nanopores from Atomically Thin Membranes*. Doctoral Dissertation Boston University. <https://open.bu.edu/handle/2144/23567>
- Cao, Z., Wang, P., Gao, W., Tao, L., Suk, J. W., Ruoff, R. S., ... Liechti, K. M. (2013). A blister test for interfacial adhesion of large-scale transferred graphene. *Carbon*, 69, 390–400. <https://doi.org/10.1016/j.carbon.2013.12.041>
- Carpick, R. W., & Salmeron, M. (1997). Scratching the Surface : Fundamental Investigations of Tribology with Atomic Force Microscopy. *Chemical Reviews*, 97, 1163–1194.
- Carvalho, B. R., Malard, L. M., Alves, J. M., Fantini, C., & Pimenta, M. A. (2015). Symmetry-dependent exciton-phonon coupling in 2D and bulk MoS₂ observed by resonance Raman scattering. *Physical Review Letters*, 114(13), 1–5. <https://doi.org/10.1103/PhysRevLett.114.136403>
- Carvalho, B. R., Malard, L. M., Alves, J. M., Fantini, C., & Pimenta, M. A. (2016).

- Erratum: Symmetry-Dependent Exciton-Phonon Coupling in 2D and Bulk MoS₂ Observed by Resonance Raman Scattering [Phys. Rev. Lett. **114**, 136403 (2015)]. *Physical Review Letters*, *116*(8), 089904. <https://doi.org/10.1103/PhysRevLett.116.089904>
- Castellanos-Gomez, A., Roldan, R., Cappelluti, E., Buscema, M., Guinea, F., Van Der Zant, H. S. J., & Steele, G. A. (2013). Local strain engineering in atomically thin MoS₂. *Nano Letters*, *13*(11), 5361–5366. <https://doi.org/10.1021/nl402875m>
- Chakraborty, B., Bera, A., Muthu, D. V. S., Bhowmick, S., Waghmare, U. V., & Sood, A. K. (2012). Symmetry-dependent phonon renormalization in monolayer MoS₂ transistor. *Physical Review B - Condensed Matter and Materials Physics*, *85*(16), 2–5. <https://doi.org/10.1103/PhysRevB.85.161403>
- Chen, Y. L., Helm, C. A., & Israelachvili, J. N. (1991). Molecular Mechanisms Associated with Adhesion and Contact Angle Hysteresis of Monolayer Surfaces. *The Journal of Physical Chemistry*, *95*, 10736–10747.
- Chhowalla, M., Shin, H. S., Eda, G., Li, L. J., Loh, K. P., & Zhang, H. (2013). The chemistry of two-dimensional layered transition metal dichalcogenide nanosheets. *Nature Chemistry*, *5*(4), 263–275. <https://doi.org/10.1038/nchem.1589>
- Cohen-Tanugi, D., & Grossman, J. C. (2012). Water desalination across nanoporous graphene. *Nano Letters*, *12*(7), 3602–3608. <https://doi.org/10.1021/nl3012853>
- Conley, H. J., Wang, B., Ziegler, J. I., Haglund, R. F., Pantelides, S. T., & Bolotin, K. I. (2013a). Bandgap engineering of strained monolayer and bilayer MoS₂. *Nano Letters*, *13*(8), 3626–3630. <https://doi.org/10.1021/nl4014748>
- Conley, H. J., Wang, B., Ziegler, J. I., Haglund, R. F., Pantelides, S. T., & Bolotin, K. I. (2013b). Bandgap engineering of strained monolayer and bilayer MoS₂. *Nano Letters*, *13*(8), 3626–3630. <https://doi.org/10.1021/nl4014748>
- Cooper, R. C., Lee, C., Marianetti, C. A., Wei, X., Hone, J., & Kysar, J. W. (2013). Nonlinear elastic behavior of two-dimensional molybdenum disulfide. *Physical Review B*, *87*(3), 035423. <https://doi.org/10.1103/PhysRevB.87.035423>
- Cranford, S., Sen, D., & Buehler, M. J. (2009). Meso-origami : Folding multilayer graphene sheets. *Applied Physics Letters*, *95*, 123121 1-4. <https://doi.org/10.1063/1.3223783>
- de Gennes, P. G. (1985). Wetting: statics and dynamics. *Reviews of Modern Physics*, *57*(3), 827–863.
- Deng, S., Gao, E., Xu, Z., & Berry, V. (2017). Adhesion Energy of MoS₂ Thin Films on

- Silicon-Based Substrates Determined via the Attributes of a Single MoS₂ Wrinkle. *ACS Applied Materials & Interfaces*, 9, 7812–7818. <https://doi.org/10.1021/acsami.6b16175>
- Dollekamp, E., Bampoulis, P., Poelsema, B., Zandvliet, H. J. W., & Kooij, E. S. (2016). Electrochemically Induced Nanobubbles between Graphene and Mica. *Langmuir*, 32, 6582–6590. <https://doi.org/10.1021/acs.langmuir.6b00777>
- Ebbesen, T. W., & Hiura, H. (1995). Graphene in 3-Dimensions: Towards Graphite Origami. *Advanced Materials*, 305(6), 582–586.
- Ellis, J. K., Lucero, M. J., & Scuseria, G. E. (2011). The indirect to direct band gap transition in multilayered MoS₂ as predicted by screened hybrid density functional theory. *Applied Physics Letters*, 99(26). <https://doi.org/10.1063/1.3672219>
- Feng, Ji, Qian, X., Huang, C., & Li, J. (2012). Strain-engineered artificial atom as a broad-spectrum solar energy funnel. *Nature Photonics*, 6(12), 866–872. <https://doi.org/10.1038/nphoton.2012.285>
- Feng, Jiandong, Liu, K., Graf, M., Dumcenco, D., Kis, A., Di Ventra, M., & Radenovic, A. (2016). Observation of ionic Coulomb blockade in nanopores. *Nature Materials*, 15(8), 850–855. <https://doi.org/10.1038/nmat4607>
- Fichter, W. (1997). Some Solutions for the Large Deflections of Uniformly Loaded Circular Membranes. *NASA Technical Paper*, 3658, 1–24.
- Gan, Y., & Zhao, H. (2014). Chirality effect of mechanical and electronic properties of monolayer MoS₂ with vacancies. *Physics Letters A*, 378(38–39), 2910–2914. <https://doi.org/10.1016/j.physleta.2014.08.008>
- Gould, P. L. (2013). *Introduction to Linear Elasticity* 3rd ed. SpringerVerlag: New York.
- Harats, M. G., Kirchhof, J. N., Qiao, M., Greben, K., & Bolotin, K. I. (2020). Dynamics and efficient conversion of excitons to trions in non-uniformly strained monolayer WS₂. *Nature Photonics*. <https://doi.org/10.1038/s41566-019-0581-5>
- He, K., Poole, C., Mak, K. F., & Shan, J. (2013). Experimental demonstration of continuous electronic structure tuning via strain in atomically thin MoS₂. *Nano Letters*, 13(6), 2931–2936. <https://doi.org/10.1021/nl4013166>
- Hill, H. M., Rigosi, A. F., Roquelet, C., Chernikov, A., Berkelbach, T. C., Reichman, D. R., ... Heinz, T. F. (2015). Observation of excitonic Rydberg states in monolayer MoS₂ and WS₂ by photoluminescence excitation spectroscopy. *Nano Letters*, 15(5), 2992–2997. <https://doi.org/10.1021/nl504868p>

- Hille, B., Armstrong, C. M., & MacKinnon, R. (1999). Ion channels: From idea to reality. *Nature Medicine*, 5(10), 1105–1109. <https://doi.org/10.1038/13415>
- Hong, J., Hu, Z., Probert, M., Li, K., Lv, D., Yang, X., ... Zhang, Z. (2015). Exploring atomic defects in molybdenum disulphide monolayers. *Nature Communications*, 6, 1–8. <https://doi.org/10.1038/ncomms7293>
- Israelachvili, J., & Berman, A. (1995). Irreversibility, Energy Dissipation, and Time Effects in Intermolecular and Surface Interactions. *Israel Journal of Chemistry*, 35, 85–91.
- Israelachvili, J. N. (2011). *Intermolecular and Surface Forces*. Academic Press.
- Jain, M., Koren, S., Miga, K. H., Quick, J., Rand, A. C., Sasani, T. A., ... Loose, M. (2018). Nanopore sequencing and assembly of a human genome with ultra-long reads. *Nature Biotechnology*, 36(4), 338–345. <https://doi.org/10.1038/nbt.4060>
- Jiang, J.-W., & Park, H. S. (2014). Negative Poisson's Ratio in Single-Layer Black Phosphorus. *Nature Communications*, 5, 1–7. <https://doi.org/10.1038/ncomms5727>
- Jiang, J. W. (2014). Phonon bandgap engineering of strained monolayer MoS₂. *Nanoscale*, 6(14), 8326–8333. <https://doi.org/10.1039/c4nr00279b>
- Khestanova, E., Fumagalli, L., Geim, A. K., & Grigorieva, I. V. (2016). Universal shape and pressure inside bubbles appearing in van der Waals heterostructures. *Nature Communications*, 7, 1–10. <https://doi.org/10.1038/ncomms12587>
- Kim, S., Choi, G. Y., Ulman, A., & Fleischer, C. (1997). Effect of Chemical Functionality on Adhesion Hysteresis. *Langmuir*, 13(4), 6850–6856.
- Kitt, A. L., Qi, Z., Remi, S., Park, H. S., Swan, A. K., & Goldberg, B. B. (2013). How Graphene Slides: Measurement and Theory of Strain-Dependent Frictional Forces between Graphene and SiO₂. *Nano Letters*, 13, 2605–2610.
- Kittel, C. (2004). *Introduction to Solid State Physics*. 8th edition. Hoboken, NJ: Wiley
- Koenig, S. P. (2013). *Graphene Membranes: Mechanics, Adhesion, and Gas Separations*. Doctoral Dissertation, University of Colorado at Boulder.
- Koenig, S. P., Boddeti, N. G., Dunn, M. L., & Bunch, J. S. (2011). Ultrastrong adhesion of graphene membranes. *Nature Nanotechnology*, 6(9), 543–546. <https://doi.org/10.1038/nnano.2011.123>
- Koenig, S. P., Wang, L., Pellegrino, J., & Bunch, J. S. (2012). Selective molecular sieving through porous graphene. *Nature Nanotechnology*, 7, 728–732. <https://doi.org/10.1038/nnano.2012.162>

- Koren, E., Lörtscher, E., Rawlings, C., Knoll, A. W., & Duerig, U. (2015). Adhesion and friction in mesoscopic graphite contacts. *Science*, *348*(6235), 679–683.
- Kou, L., Du, A., Chen, C., & Frauenheim, T. (2014). Strain engineering of selective chemical adsorption on monolayer MoS₂. *Nanoscale*, *6*, 5156–5161.
<https://doi.org/10.1039/c3nr06670c>
- Lee, C., Li, Q., Kalb, W., Liu, X., Berger, H., Carpick, R. W., & Hone, J. (2010). Frictional Characteristics of Atomically Thin Sheets. *Science*, *328*, 76–80.
<https://doi.org/10.1126/science.1184167>
- Lee, C., Yan, H., Brus, L. E., Heinz, T. F., Hone, J., & Ryu, S. (2010). Anomalous lattice vibrations of single- and few-layer MoS₂. *ACS Nano*, *4*(5), 2695–2700.
<https://doi.org/10.1021/nn1003937>
- Lee, H. S., Min, S. W., Chang, Y. G., Park, M. K., Nam, T., Kim, H., ... Im, S. (2012). MoS₂ nanosheet phototransistors with thickness-modulated optical Energy gap. *Nano Letters*, *12*(7), 3695–3700. <https://doi.org/10.1021/nl301485q>
- Li, H., Contryman, A. W., Qian, X., Ardakani, S. M., Gong, Y., Wang, X., ... Zheng, X. (2015). Optoelectronic crystal of artificial atoms in strain-textured molybdenum disulphide. *Nature Communications*, *6*(May), 7381.
<https://doi.org/10.1038/ncomms8381>
- Li, H., Zhang, Q., Yap, C. C. R., Tay, B. K., Edwin, T. H. T., Olivier, A., & Baillargeat, D. (2012). From bulk to monolayer MoS₂: Evolution of Raman scattering. *Advanced Functional Materials*, *22*(7), 1385–1390.
<https://doi.org/10.1002/adfm.201102111>
- Li, J., Shan, Z., Ma, E., & Editors, G. (2014). Elastic strain engineering for unprecedented materials properties. *MRS Bulletin* *39*(February), 108–114.
<https://doi.org/10.1557/mrs.2014.3>
- Li, Song-lin, Miyazaki, H., Song, H., Kuramochi, H., & Nakaharai, S. (2012). Quantitative Raman Spectrum and Reliable Thickness Identification for Atomic Layers on Insulating Substrates, *ACS Nano*, *6*(8), 7381–7388.
- Li, Suzhi, Li, Q., Carpick, R. W., Gumbsch, P., Liu, X. Z., Ding, X., ... Li, J. (2016). The evolving quality of frictional contact with graphene. *Nature*, *539*, 2–7.
<https://doi.org/10.1038/nature20135>
- Li, T. (2012). Ideal strength and phonon instability in single-layer MoS₂. *Physical Review B - Condensed Matter and Materials Physics*, *85*(23), 1–5.
<https://doi.org/10.1103/PhysRevB.85.235407>

- Li, X., Cai, W., An, J., Kim, S., Nah, J., Yang, D., ... Ruoff, R. S. (2009). Large-area synthesis of high-quality and uniform graphene films on copper foils. *Science*, 324(5932), 1312–1314. <https://doi.org/10.1126/science.1171245>
- Lien, D. H., Uddin, S. Z., Yeh, M., Amani, M., Kim, H., Ager, J. W., ... Javey, A. (2019). Electrical suppression of all nonradiative recombination pathways in monolayer semiconductors. *Science*, 364(6439), 468–471. <https://doi.org/10.1126/science.aaw8053>
- Liu, H.-L., Guo, H., Yang, T., Zhang, Z., Kumamoto, Y., Shen, C.-C., ... Kawata, S. (2015). Anomalous lattice vibrations of monolayer MoS₂ probed by ultraviolet Raman scattering. *Physical Chemistry, Chemical Physics*, 17(22), 14561–14568. <https://doi.org/10.1039/C5CP01347J>
- Liu, K., Yan, Q., Chen, M., Fan, W., Sun, Y., Suh, J., ... Wu, J. (2014). Elastic Properties of Chemical-Vapor-Deposited Monolayer MoS₂, WS₂, and Their Bilayer Heterostructures. *Nano Letters*, 14, 5097–5103.
- Liu, X. (2014). *Nanomechanical Systems from 2D Materials*. Doctoral dissertation, University of Colorado at Boulder. https://scholar.colorado.edu/concern/graduate_thesis_or_dissertations/kw52j832v
- Liu, X., Suk, J. W., Boddeti, N. G., Cantley, L., Wang, L., Gray, J. M., ... Bunch, J. S. (2014). Large Arrays and Properties of 3-Terminal Graphene Nanoelectromechanical Switches. *Advanced Materials*, 26, 1571–1576. <https://doi.org/10.1002/adma.201304949>
- Lloyd, D., Liu, X., Christopher, J. W., Cantley, L., Wadehra, A., Kim, B. L., ... Bunch, J. S. (2016). Band Gap Engineering with Ultralarge Biaxial Strains in Suspended Monolayer MoS₂. *Nano Letters*, 16, 5836–5841. <https://doi.org/10.1021/acs.nanolett.6b02615>
- Lohse, D., & Zhang, X. (2015). Surface nanobubbles and nanodroplets. *Reviews of Modern Physics*, 87(3), 981–1035. <https://doi.org/10.1103/RevModPhys.87.981>
- López-Polín, G., Gómez-Navarro, C., Parente, V., Katsnelson, M. I., Pérez-Murano, F., & Gómez-Herrero, J. (2015). Increasing the elastic modulus of graphene by controlled defect creation. *Nature Physics*, 11, 26–31. <https://doi.org/10.1038/NPHYS3183>
- Lugstein, A., Steinmair, M., Steiger, A., Kosina, H., & Bertagnolli, E. (2010). Anomalous Piezoresistance Effect in Ultrastained Silicon Nanowires. *Nano Letters*, 10(8), 3204–3208. <https://doi.org/10.1021/nl102179c>

- Mak, K. F., He, K., Lee, C., Lee, G. H., Hone, J., Heinz, T. F., & Shan, J. (2013). Tightly bound trions in monolayer MoS₂. *Nature Materials*, *12*(3), 207–211. <https://doi.org/10.1038/nmat3505>
- Mak, K. F., Lee, C., Hone, J., Shan, J., & Heinz, T. F. (2010). Atomically thin MoS₂: A new direct-gap semiconductor. *Physical Review Letters*, *105*(13), 2–5. <https://doi.org/10.1103/PhysRevLett.105.136805>
- Mak, K. F., & Shan, J. (2016). Photonics and optoelectronics of 2D semiconductor transition metal dichalcogenides. *Nature Photonics*, *10*(4), 216–226. <https://doi.org/10.1038/nphoton.2015.282>
- Manchanda, P., Sellmyer, D. J., & Skomski, R. (2015). Magnetism of Ta dichalcogenide monolayers tuned by strain and hydrogenation. *Applied Physics Letters*, *107*(3), 032402
- Manzeli, S., Allain, A., Ghadimi, A., & Kis, A. (2015a). Piezoresistivity and Strain-induced Band Gap Tuning in Atomically Thin MoS₂. *Nano Letters*, *15*(8), 5330–5335. <https://doi.org/10.1021/acs.nanolett.5b01689>
- Manzeli, S., Allain, A., Ghadimi, A., & Kis, A. (2015b). Piezoresistivity and Strain-induced Band Gap Tuning in Atomically Thin MoS₂. *Nano Letters*, *15*(8), 5330–5335. <https://doi.org/10.1021/acs.nanolett.5b01689>
- Manzeli, S., Ovchinnikov, D., Pasquier, D., Yazyev, O. V., & Kis, A. (2017). 2D transition metal dichalcogenides. *Nature Reviews Materials*, *2*. <https://doi.org/10.1038/natrevmats.2017.33>
- Marion, S., Macha, M., Davis, S. J., Chernev, A., & Radenovic, A. (2019). Nanobubbles at nanopores probed with pressure. *Arxiv*. Retrieved from <http://arxiv.org/abs/1911.05229>
- Maugis, D., & Barquins, M. (1978). Fracture mechanics and the adherence of viscoelastic bodies. *Journal of Physics D: Applied Physics*, *11*(14), 1989–2023.
- Nan, H., Wang, Z., Wang, W., Liang, Z., Lu, Y., Chen, Q., ... Ni, Z. (2014). Strong photoluminescence enhancement of MoS₂ through defect engineering and oxygen bonding. *ACS Nano*, *8*(6), 5738–5745. <https://doi.org/10.1021/nn500532f>
- Nayak, A. P., Bhattacharyya, S., Zhu, J., Liu, J., Wu, X., Pandey, T., ... Lin, J.-F. (2014). Pressure-induced semiconducting to metallic transition in multilayered molybdenum disulfide. *Nature Communications*, *5*(3731), 1–9. <https://doi.org/10.1038/ncomms4731>

- Nayak, A. P., Pandey, T., Voiry, D., Liu, J., Moran, S. T., Sharma, A., ... Akinwande, D. (2015). Pressure-dependent optical and vibrational properties of monolayer molybdenum disulfide. *Nano Letters*, *15*(1), 346–353. <https://doi.org/10.1021/nl5036397>
- Nourbakhsh, A., Zubair, A., Sajjad, R. N., Amir, T. K. G., Chen, W., Fang, S., ... Palacios, T. (2016). MoS₂ Field-Effect Transistor with Sub-10 nm Channel Length. *Nano Letters*, *16*(12), 7798–7806. <https://doi.org/10.1021/acs.nanolett.6b03999>
- Nowak, E., Combes, G., Stitt, E. H., & Patek, A. W. (2013). A comparison of contact angle measurement techniques applied to highly porous catalyst supports. *Powder Technology*, *233*(January), 52–64. <https://doi.org/10.1016/j.powtec.2012.08.032>
- O'Hern, S. C., Boutilier, M. S. H., Idrobo, J.-C., Song, Y., Kong, J., Laoui, T., ... Karnik, R. (2014). Selective Ionic Transport through Tunable Subnanometer Pores in Single-Layer Graphene Membranes. *Nano Letters*, *14*, 1234–1241.
- Peelaers, H., & Van De Walle, C. G. (2012). Effects of strain on band structure and effective masses in MoS₂. *Physical Review B - Condensed Matter and Materials Physics*, *86*(24), 1–5. <https://doi.org/10.1103/PhysRevB.86.241401>
- Peng, Q., Ji, W., & De, S. (2012). Mechanical properties of the hexagonal boron nitride monolayer: Ab initio study. *Computational Materials Science*, *56*, 11–17. <https://doi.org/10.1016/j.commatsci.2011.12.029>
- Plechinger, G., Castellanos-Gomez, A., Buscema, M., van der Zant, H. S. J., Steele, G. a, Kuc, A., ... Korn, T. (2015). Control of biaxial strain in single-layer molybdenite using local thermal expansion of the substrate. *2D Materials*, *2*(1), 015006. <https://doi.org/10.1088/2053-1583/2/1/015006>
- Qian, L., & Yu, B. (2013). Adhesion Hysteresis. In *Adhesion Hysteresis. Encyclopedia of Tribology* (pp. 29–32). <https://doi.org/10.1007/978-0-387-92897-5>
- Radisavljevic, B., Radenovic, A., Brivio, J., Giacometti, V., & Kis, A. (2011a). Single-layer MoS₂ transistors, *6*(March). <https://doi.org/10.1038/nnano.2010.279>
- Radisavljevic, B., Radenovic, A., Brivio, J., Giacometti, V., & Kis, A. (2011b). Single-layer MoS₂ transistors. *Nature Nanotechnology*, *6*(3), 147–150. <https://doi.org/10.1038/nnano.2010.279>
- Rice, C., Young, R. J., Zan, R., Bangert, U., Wolverson, D., Georgiou, T., ... Novoselov, K. S. (2013). Raman-scattering measurements and first-principles calculations of strain-induced phonon shifts in monolayer MoS₂. *Physical Review B - Condensed Matter and Materials Physics*, *87*(8), 1–5. <https://doi.org/10.1103/PhysRevB.87.081307>

- Rigosi, A. F. (2016). *Investigation of Two-Dimensional Transition Metal Dichalcogenides by Optical and Scanning Tunneling Spectroscopy*. Doctoral dissertation, Columbia University.
<https://academiccommons.columbia.edu/doi/10.7916/D8WH2PXD>
- Roldan, R., Castellanos-gomez, A., & Cappelluti, E. (2015). Strain engineering in semiconducting two-dimensional crystals. *Journal of Physics: Condensed Matter*, 27. <https://doi.org/10.1088/0953-8984/27/31/313201>
- Roser, M. (2020). Moore's Law: Transistors per processor.
- Roy, K., Padmanabhan, M., Goswami, S., Sai, T. P., Ramalingam, G., Raghavan, S., & Ghosh, A. (2013). Graphene-MoS 2 hybrid structures for multifunctional photoresponsive memory devices. *Nature Nanotechnology*, 8(11), 826–830.
<https://doi.org/10.1038/nnano.2013.206>
- Sahu, S., & Zwolak, M. (2018). Colloquium: Ionic phenomena in porous 2D materials and their applications. Retrieved from <http://arxiv.org/abs/1809.05098>
- Sahu, S., & Zwolak, M. (2019). Colloquium: Ionic phenomena in nanoscale pores through 2D materials. *Reviews of Modern Physics*, 91(2), 21004.
<https://doi.org/10.1103/RevModPhys.91.021004>
- Scalise, E., Houssa, M., Pourtois, G., Afanas'ev, V., & Stesmans, A. (2012). Strain-induced semiconductor to metal transition in the two-dimensional honeycomb structure of MoS₂. *Nano Research*, 5(1), 43–48. <https://doi.org/10.1007/s12274-011-0183-0>
- Scheuschner, N., Ochedowski, O., Kaulitz, A. M., Gillen, R., Schleberger, M., & Maultzsch, J. (2014). Photoluminescence of freestanding single- and few-layer MoS₂. *Physical Review B - Condensed Matter and Materials Physics*, 89(12), 2–7.
<https://doi.org/10.1103/PhysRevB.89.125406>
- Shi, Z., Lu, H., Zhang, L., Yang, R., Wang, Y., Liu, D., ... Zhang, G. (2012). Studies of Graphene-Based Nanoelectromechanical Switches. *Nano Research*, 5(2), 82–87.
<https://doi.org/10.1007/s12274-011-0187-9>
- Shull, K. R. (2002). Contact mechanics and the adhesion of soft solids. *Materials Science and Engineering*, 36, 1–45.
- Signorello, G., Karg, S., Björk, M. T., Gotsmann, B., & Riel, H. (2013). Tuning the light emission from GaAs nanowires over 290 meV with uniaxial strain. *Nano Letters*, 13(3), 917–924. <https://doi.org/10.1021/nl303694c>
- Simon, S. H. (2016). *The Oxford Solid State Basics*. Oxford: Oxford University Press.

- Smith, A. D., Niklaus, F., Paussa, A., Schröder, S., Fischer, A. C., Sterner, M., ... Lemme, M. C. (2016). Piezoresistive Properties of Suspended Graphene Membranes under Uniaxial and Biaxial Strain in Nanoelectromechanical Pressure Sensors. *ACS Nano*, *10*, 9879–9886. <https://doi.org/10.1021/acsnano.6b02533>
- Steinhoff, A., Kim, J. H., Jahnke, F., Rösner, M., Kim, D. S., Lee, C., ... Gies, C. (2015). Efficient Excitonic Photoluminescence in Direct and Indirect Band Gap Monolayer MoS₂. *Nano Letters*, *15*(10), 6841–6847. <https://doi.org/10.1021/acs.nanolett.5b02719>
- Suh, J., Park, T. E., Lin, D. Y., Fu, D., Park, J., Jung, H. J., ... Wu, J. (2014). Doping against the native propensity of MoS₂: Degenerate hole doping by cation substitution. *Nano Letters*, *14*(12), 6976–6982. <https://doi.org/10.1021/nl503251h>
- Suk, J. W., Kitt, A., Magnuson, C. W., Hao, Y., Ahmed, S., An, J., ... Ruoff, R. S. (2011). Transfer of CVD-grown monolayer graphene onto arbitrary substrates. *ACS Nano*, *5*(9), 6916–6924. <https://doi.org/10.1021/nn201207c>
- Suk, J. W., Na, S. R., Stromberg, R. J., Stauffer, D., Lee, J., Ruoff, R. S., & Liechti, K. M. (2016). Probing the adhesion interactions of graphene on silicon oxide by nanoindentation. *Carbon*, *103*, 63–72. <https://doi.org/10.1016/j.carbon.2016.02.079>
- Sun, P. Z., Yang, Q., Kuang, W. J., Stebunov, Y. V., Xiong, W. Q., Yu, J., ... Geim, A. K. (2020). Limits on gas impermeability of graphene. *ArXiv:1912.09220*.
- Sun, Y., Thompson, S. E., & Nishida, T. (2007). Physics of strain effects in semiconductors and metal-oxide-semiconductor field-effect transistors. *Journal of Applied Physics*, *101*(10). <https://doi.org/10.1063/1.2730561>
- Thiruraman, J. P., Fujisawa, K., Danda, G., Das, P. M., Zhang, T., Bolotsky, A., ... Drndić, M. (2018). Angstrom-Size Defect Creation and Ionic Transport through Pores in Single-Layer MoS₂. *Nano Letters*, *18*(3), 1651–1659. <https://doi.org/10.1021/acs.nanolett.7b04526>
- Tian, K., Gosvami, N. N., Goldsby, D. L., Liu, Y., Szlufarska, I., & Carpick, R. W. (2017). Load and Time Dependence of Interfacial Chemical Bond-Induced Friction at the Nanoscale. *Physical Review Letters*, *118*, 076103, 1–6. <https://doi.org/10.1103/PhysRevLett.118.076103>
- Tsai, M. L., Su, S. H., Chang, J. K., Tsai, D. S., Chen, C. H., Wu, C. I., ... He, J. H. (2014). Monolayer MoS₂ heterojunction solar cells. *ACS Nano*, *8*(8), 8317–8322. <https://doi.org/10.1021/nn502776h>
- van den Beld, W. (2016). *Graphene and permalloy integration in functional fluidic and solid-state devices*. Doctoral dissertation, University of Twente.

<https://doi.org/10.3990/1.9789036541893>

- van der Zande, A. M., Huang, P. Y., Chenet, D. a, Berkelbach, T. C., You, Y., Lee, G.-H., ... Hone, J. C. (2013). Grains and grain boundaries in highly crystalline monolayer molybdenum disulphide. *Nature Materials*, 12(6), 554–561. <https://doi.org/10.1038/nmat3633>
- Verreck, D., Arutchelvan, G., Heyns, M. M., & Radu, I. P. (2019). Device and circuit level gate configuration optimization for 2d material field-effect transistors. *International Conference on Simulation of Semiconductor Processes and Devices, SISPAD, 2019*, 1–4. <https://doi.org/10.1109/SISPAD.2019.8870506>
- Wan, K.-T., & Mai, Y.-W. (1995). Fracture Mechanics of a New Blister Test with Stable Crack Growth. *Acta Metallurgica et Materialia*, 43(11), 4109–4115.
- Wang, L., Travis, J. J., Cavanagh, A. S., Liu, X., Koenig, S. P., Huang, P. Y., ... Bunch, J. S. (2012). Ultrathin Oxide Films by Atomic Layer Deposition on Graphene. *Nano Letters*, 12, 3706–3710.
- Wang, P., Liechti, K. M., & Huang, R. (2016). Snap Transitions of Pressurized Graphene Blisters. *Journal of Applied Mechanics*, 83(7), 1–14. <https://doi.org/10.1115/1.4033305>
- Wang, Y., Cong, C., Qiu, C., & Yu, T. (2013). Raman spectroscopy study of lattice vibration and crystallographic orientation of monolayer MoS₂ under uniaxial strain. *Small*, 9(17), 2857–2861. <https://doi.org/10.1002/smll.201202876>
- Wang, Y., Cong, C., Yang, W., Shang, J., Peimyoo, N., Chen, Y., ... Yu, T. (2015). Strain-induced direct–indirect bandgap transition and phonon modulation in monolayer WS₂. *Nano Research*, 8(8), 2562–2572. <https://doi.org/10.1007/s12274-015-0762-6>
- Wu, S., Huang, C., Aivazian, G., Ross, J. S., Cobden, D. H., & Xu, X. (2013). Vapor Solid Growth of High Optical Quality MoS₂ Monolayers with Near-Unity Valley Polarization. *ACS Nano*, 7(3), 2768–2772. <https://doi.org/10.1021/nn4002038>
- Wu, W., Wang, L., Li, Y., Zhang, F., Lin, L., Niu, S., ... Wang, Z. L. (2014). Piezoelectricity of single-atomic-layer MoS₂ for energy conversion and piezotronics. *Nature*, 514(7523), 470–474. <https://doi.org/10.1038/nature13792>
- Yeung Yu Hui, Xiaofei Liu, Wenjing Jie, Ngai Yui Chan, Jianhua Hao, Yu-Te Hsu, Lain-Jong Li, Wanlin Guo, S. P. L. (2013). Exceptional Tunability of Band Energy in a Compressively Strained Trilayer MoS₂ Sheet. *ACS Nano*, (8), 7126–7131.

- Yu, S., Xiong, H. D., Eshun, K., Yuan, H., & Li, Q. (2015). Phase transition, effective mass and carrier mobility of MoS₂ monolayer under tensile strain. *Applied Surface Science*, 325, 27–32. <https://doi.org/10.1016/j.apsusc.2014.11.079>
- Yu, Yalin, Sanchez, D., & Lu, N. (2015). Work of adhesion / separation between soft elastomers of different mixing ratios. *Journal of Materials Research*, 30(18), 2702–2712. <https://doi.org/10.1557/jmr.2015.242>
- Yu, Yiling, Yu, Y., Cai, Y., Li, W., Gurarslan, A., Peelaers, H., ... Cao, L. (2015). Exciton-dominated Dielectric Function of Atomically Thin MoS₂ Films. *Scientific Reports*, 5, 16996, 1–7. <https://doi.org/10.1038/srep16996>
- Zabel, J., Nair, R. R., Ott, A., Georgiou, T., Geim, A. K., Novoselov, K. S., & Casiraghi, C. (2012). Raman spectroscopy of graphene and bilayer under biaxial strain: Bubbles and balloons. *Nano Letters*, 12(2), 617–621. <https://doi.org/10.1021/nl203359n>
- Zandiatashbar, A., Lee, G., An, S. J., Lee, S., Mathew, N., Terrones, M., ... Koratkar, N. (2014). Effect of defects on the intrinsic strength and stiffness of graphene. *Nature Communications*, 5, 1–9. <https://doi.org/10.1038/ncomms4186>
- Zhang, Y., Yao, Y., Sendeku, M. G., Yin, L., Zhan, X., Wang, F., ... He, J. (2019). Recent Progress in CVD Growth of 2D Transition Metal Dichalcogenides and Related Heterostructures. *Advanced Materials*, 31(41), 1–30. <https://doi.org/10.1002/adma.201901694>
- Zhu, H., Wang, Y., Xiao, J., Liu, M., Xiong, S., Wong, Z. J., ... Ye, Y. (2014). Observation of piezoelectricity in free-standing monolayer MoS₂. *Nature Nanotechnology*, 10(2), 151–155. <https://doi.org/10.1038/nnano.2014.309>
- Zhu, T., & Li, J. (2010). Progress in Materials Science Ultra-strength materials. *Progress in Materials Science*, 55(7), 710–757. <https://doi.org/10.1016/j.pmatsci.2010.04.001>
- Zong, Z., Chen, C., Dokmeci, M. R., & Wan, K. (2010). Direct measurement of graphene adhesion on silicon surface by intercalation of nanoparticles. *Journal of Applied Physics*, 107, 026104. <https://doi.org/10.1063/1.3294960>

CURRICULUM VITAE**David Lloyd**

dlloyd1@bu.edu • 25 Westbourne Terrace, Brookline, MA 02446 • 617-415-6450

Nationality: UK • Year of Birth: 1991

Education

Boston University Boston, MA
 PhD in Mechanical Engineering May 2020
 Deans Fellow and BU Nano Fellowship recipient

University of Oxford Oxford, UK
 MPhys 2013
 Relevant coursework: MPhys project in condensed matter physics with Prof. A Turberfield

Experience

Boston University Boston, MA
PhD researcher Aug. 2014 Year – present

- Developed novel CVD growth recipe to grow high quality 2D MoS₂ crystals with a large breaking strength and a low permeability to gases.
- Demonstrated that biaxial strain can be used to significantly modulate the band gap of monolayer MoS₂ by as much as 25%, using photoluminescence spectroscopy and AFM measurements.
- Determined the interfacial adhesion and adhesion hysteresis in 2D MoS₂ by using a pressurized blister test, also examining the mechanical instabilities of these systems.
- Built a microfluidic platform to study the transmembrane transport properties of 2D crystals, using cleanroom fabrication techniques extensively.
- Investigated the properties of nanopores in single layer graphene, MoS₂ and hBN membranes and their potential application in nanofiltration and desalination. Measured the ionic transconductance properties of nanopores via electrical measurements and simultaneous in situ liquid AFM.
- Presented research at APS March Meeting and Society of Engineering Science conferences.
- Finalist at the BUnano Symposium entrepreneurship competition for translational research.

University of Oxford Oxford, UK
MPhys project Feb. 2013 – April 2013

- Designed self-assembling DNA nanostructures, with DNA nucleotide sequence encoding the order of assembly. Exposure to both wet-lab and computational analysis techniques.

Leadership and Activities

Boston University Graduate teaching assistant

Boston, MA
Sep. 2015 – May 2015

- Responsible for running weekly discussion sessions, grading exams, overseeing practical labs and design projects, and occasionally giving lectures.

Research Mentor

Sep. 2015 – present

- Mentored 10+ masters, undergraduate and high school students in conducting research in the lab, responsible for designing suitable projects and teaching mentees the necessary new skills.

Publications

David Lloyd, Xinghui Liu, Jason W Christopher, Lauren Cantley, Anubhav Wadehra, Brian L Kim, Bennett B Goldberg, Anna K Swan, J Scott Bunch (2016) Band Gap Engineering with Ultralarge Biaxial Strains in Suspended Monolayer MoS₂, *Nano Letters* 16, 9, 5836-5841

David Lloyd, Xinghui Liu, Narasimha Boddeti, Lauren Cantley, Rong Long, Martin L Dunn, J Scott Bunch (2017) Adhesion, Stiffness, and Instability in Atomically Thin MoS₂ Bubbles, *Nano Letters* 17, 9, 5329-5334

Zhong Lin, Yu Lei, Shruti Subramanian, Natalie Briggs, Yuanxi Wang, Chun-Li Lo, Eilam Yalon, **David Lloyd**, Sanfeng Wu, Kristie Koski, Richard Clark, Saptarshi Das, Robert M Wallace, Thomas Kuech, Joseph Scott Bunch, Xiaoqin Li, Zhihong Chen, Eric Pop, Vincent H Crespi, Joshua A Robinson, Mauricio Terrones (2018) Research Update: Recent progress on 2D materials beyond graphene: From ripples, defects, intercalation, and valley dynamics to straintronics and power dissipation, *APL Materials*, 6, 8, 080701

Robin J Dolleman, **David Lloyd**, Martin Lee, J Scott Bunch, Herre SJ van der Zant, Peter G Steeneken (2018) Transient thermal characterization of suspended monolayer MoS₂ *Physical Review Materials*, 2, 11, 114008

Jason W Christopher, Mounika Vutukuru, **David Lloyd**, J Scott Bunch, Bennett B Goldberg, David J Bishop, Anna K Swan (2019) Monolayer MoS₂ Strained to 1.3% With a Microelectromechanical System, *Journal of Microelectromechanical Systems*, 28, 2, 254-263

Lauren Cantley, Jacob L Swett, **David Lloyd**, David A Cullen, Ke Zhou, Peter V Bedworth, Scott Heise, Adam J Rondinone, Zhiping Xu, Steve Sinton, J Scott Bunch (2019) Voltage gated inter-cation selective ion channels from graphene nanopores, *Nanoscale*, 11, 20, 9856-9861

Skills & Interests

Technical: Good working knowledge of MATLAB, experience with C and Shell programming

Language: Basic French

Laboratory: Standard cleanroom techniques (photolithography, deposition and etching), Raman and photoluminescence spectroscopy, AFM, SEM, E-beam lithography

Interests: Cycle touring, running, piano improvisation, reading, hiking, sailing